EXPERIMENTAL INVESTIGATION AND THEORETICAL ANALYSIS OF THE STRUCTURAL RELAXATION IN AMORPHOUS $Fe_{40}Ni_{40}B_{20}$

BY

Munsami Valanathan

Submitted in fulfilment of the
requirements for the degree of
Doctor of Philosophy
in the
School of Pure and Applied Physics,
University of Natal,
Durban
December 1998

Acknowledgments

The presentation of this thesis would not have been possible without contribution and sacrifice from many colleagues and members of my family.

Firstly, I must thank my supervisor, Prof T B Doyle. Having drawn copiously on his ideas and factual knowledge, I take this opportunity to thank him for these and many other invaluable sacrifices and hidden inputs.

Among others who have helped, I must commend the Physics Workshop (particularly Mr W de Beer) for their prompt attention to all aspects of designing and commissioning of the experimental apparatus.

Thanks to my colleagues Leigh Jarvis and Vish Naidoo for their concern and assistance and to Mr and Mrs Terry Govender for their interest and encouragement.

I also owe my gratitude to my parents and parent-in-laws for their support and encouragement, without which this study would not have been possible.

Finally, but not in the least, I would especially like to thank my wife Sugendri for her forbearance, love and support throughout the course of my research.

In memory of my dear departed friend, Rajendran Govender

Abstract

Amorphous metallic alloys are produced by a variety of techniques some of which involve rapid solidification of the alloying constituents. In these methods the solidification occurs so rapidly that the atoms are frozen-in and partially retain their liquid configuration. There are clear structural and other indications from their various properties that amorphous metallic alloys possess short range order but lack long range order. In general, amorphous alloys are not in a thermodynamic equilibrium state and, therefore, relax structurally whenever atoms attain an appreciable mobility. Associated with structural relaxation, many physical properties change; some significantly and others only slightly.

Relaxation experiments in amorphous metallic alloys often display approximate $\ln(t)$ kinetics which can be understood in terms of various models. In the present work the model by Primak (1955), for which the kinetic behaviour of a system depends on processes that are distributed over a range of activation energies, is used as a basis for further development. The Primak model allows, in principle, for the identification of the order of the relaxation reaction and for the determination of an initial activation energy spectrum $p_o(\epsilon_o)$, where ϵ_o is a characteristic activation energy. Although the model provides for a qualitative explanation of the $\ln(t)$ law, it has no predictive power as to the quantitative changes accompanying the various relaxing properties. Furthermore, an estimation of $p_o(\epsilon_o)$, inferred from various isothermal annealing procedures, reveals the approximate shape but does not fix its location on the activation energy axis. These shortfalls are attributed to complications in the frequency factor ν, inherent to the Primak model. Also, the Primak model does not include consideration of the entropy involved in a 'configurational jump' of any particular atom during the relaxation process. Inclusion of the configurational entropy through the frequency factor ν, in the present treatment, leads to a 'relaxation equation'.

Structural relaxation measurements of density (in practice length - from which

density can be approximately inferred) and electrical resistivity, in an $Fe_{40}Ni_{40}B_{20}$ alloy, have been obtained and fitted to this relaxation equation. The fitting parameters are found, within experimental error, to be the same for both length and resistivity relaxation. The initial activation energy spectrum $p_o(\epsilon_o)$, as inferred from the fits, over the energy range 1.4 to 2.0 eV, reveals roughly three regimes, namely below 1.5 eV, from 1.5 to 1.8 eV, and above 1.8 eV, respectively, over which the initial activation energy spectrum $p_o(\epsilon_o)$ assumes different approximately constant values. Previous treatments have, however, implicitly assumed that $p_o(\epsilon_o)$ is constant throughout a temperature range over which $\ln(t)$ kinetics is observed. The behaviour observed in this work is associated with the intrinsic relaxation mechanism involving consecutive diffusion of the metallic and metalloid atoms, respectively. A configurational entropy change inferred from this work is found to be negative as a consequence of contraction of the spread-out free volume resulting from thermal fluctuations.

Within the framework of the 'present model', other related behaviour of amorphous metallic alloys, including the glass transition, crystallization and diffusion, are discussed. Where direct comparison between theory and experiment is possible for the various observed phenomena, the agreement is good and shows an overall consistency in our approach. Finally, the analysis considered here gives an expression which can be easily used to make quantitative predictions about the experimental relaxation behaviour. An immediate understanding of some of the main features of experimental data on relaxation can, therefore, be obtained through application of the present model.

Contents

1 Introduction **1**

1.1 Historical Review 1

1.2 Glass Formation Criteria 5

1.2.1 Kinetic Criterion 7

1.2.2 Free Volume Criterion 13

1.3 Amorphous Alloy Fabrication 15

1.4 Physical Properties and Applications 21

1.5 Structural Features 24

1.6 Structural Models 28

1.6.1 Introduction 28

1.6.2 Microcrystallite Model 29

1.6.3 Amorphous Cluster Model 30

1.6.4 Dense Random Packing Model 31

1.7 Structural Defects 33

1.7.1 Introduction 33

1.7.2 Point Defects 35

1.7.3 Line Defects 36

1.8 Relaxation Phenomena 37

1.9 Scope of Thesis 40

2 Theory **41**

2.1 Introduction 41

2.2 Relaxation Models 42

2.2.1 A Spectrum of Relaxation Times 42

2.2.2 Percolation Model 44

2.2.3 Short Range Ordering 46

2.2.4 Kinetics of Processes Distributed in Activation Energy 52

2.3 A Review of Relaxation Phenomena 59

2.4 Development of a 'Relaxation Equation' 75

2.5 Structural Relaxation Mechanisms 84

3 Experimental **91**

3.1 Introduction 91

3.2 As-Prepared Specimen Characteristics 93

3.3 Description of Apparatus 94

3.4 Specimen Temperature Regulation 102

3.5 Length Measurement 106

3.6 Resistance Measurement 106

3.7 Data Capture and Control 109

3.8 Modus Operandi 114

4 Results and Discussion **115**

4.1 Introduction 115

4.2 Experimental Results 115

4.3 The Initial Activation Energy Spectrum $p_o(\epsilon_o)$ 120

4.3.1 The Behaviour of $p_o(\epsilon_o)$ 120

4.3.2 Relaxation Processes that Determine $p_o(\epsilon_o)$ 125
4.4 Use of the 'Relaxation Equation' 138
4.5 Some Implications of the 'Relaxation Equation' 144
4.5.1 Scaling Behaviour 144
4.5.2 Entropy 145
4.5.3 Free Volume Annihilation 149

5 Other Related Effects **151**
5.1 The Glass Transition Temperature 151
5.2 Diffusion 153
5.3 Crystallization 155

6 Conclusion **160**

7 References **164**

8 Appendix **176**

List of Figures

1.1 A graph of volume versus temperature during rapid quenching. The arrow illustrates the volume change accompanying structural relaxation of the glass if held at temperature T_1. 8

1.2 A graph of Heat Capacity C_p versus Temperature, depicting the glass transition. 9

1.3 Time-Temperature-Transformation curves (solid lines) and the corresponding Continuous-Cooling-Transformation curves (dashed lines) for Ni, $Au_{78}Ge_{14}Si_8$, $Pd_{82}Si_{18}$ and $Pd_{78}Cu_6Si_{16}$ (Davies, 1983). 12

1.4 Viscosities ($\log\eta$) of a variety of organic glasses as a function of reduced reciprocal temperature $\frac{T_g}{T}$. The curves have been normalized such that the glass transition temperature is defined when $\eta = 10^{13}$ poise (Wong and Angell, 1976). 16

1.5 Melt spinning technique for fabrication of ribbon specimens. 20

1.6 Structural origin of the radial distribution function (Ziman, 1979). 26

1.7 Typical plots of $I(k)$, $RDF(r)$ and $G(r)$ (Cahn, 1980). 27

2.1 Relaxation time spectrum $H(\log\tau_r)$ for a metal glass at various temperatures (Chen, 1981b). 45

2.2 Distribution in hydrostatic stress P_s (Srolovitz *et al*, 1981). 50

2.3 Distribution in shear stress τ_s (Srolovitz *et al*, 1981). 51

2.4 The characteristic annealing function θ_n vs ϵ. 54

2.5 A schematic representation of the initial activation energy spectrum $p_o(\epsilon)$ being swept out as the characteristic annealing function θ_n advances in activation energy. 56

2.6 Temperature dependence of $< P_s^2 >$ and $< \tau_s^2 >$ calculated for a model amorphous iron. T_g is the glass temperature, T_f the fictive temperature and T_g' the upper glass transition temperature (Egami and Srolovitz, 1982). 60

2.7 V_f versus $\log(c't)$ for three initial values of V_{fo} (Van den Beukel and Radelaar, 1983). 63

2.8 $\Delta V_f = V_{fo} - V_f$ versus $\log(c't)$ for three initial values of V_{fo} (Van den Beukel and Radelaar, 1983). 64

2.9 Evolution of heat during continuous heating of an as-quenched glass and of glasses pre-annealed at 400 and 450 K during the times indicated (Van den Beukel and Radelaar, 1983). 67

2.10 Histogram of the relaxation time spectrum for FeNiPB (Cost and Stanley, 1984). 69

2.11 Changes in T_c and the corresponding enthalpy evolution of the $Fe_{40}Ni_{40}P_{14}B_6$ glass (Chen, 1983). 72

2.12 Changes in length during short-time annealing of amorphous $Fe_{40}Ni_{40}B_{20}$. The annealing temperatures are (a) 323 K, (b) 573 K, (c) 598 K, (d) 623 K and (e) 673 K (Kursmovic *et al*, 1980). 76

2.13 Potential energy plot for a two level system. 78

2.14 $\ln(\nu)$ vs Temperature for $Fe_{40}Ni_{40}P_{14}B_6$ ($\nu(\tau)$ taken from Chen (1981a), Berry and Pritchet (1976) and Balanzat (1980)). 85

2.15 Schematic representation of a place exchange mechanism. 86

2.16 Schematic representation of interstitial diffusion. 87
2.17 Schematic representation of migration of vacancies (free volume). 88

3.1 Energy Dispersive X-ray Analysis of $Fe_{40}Ni_{40}B_{20}$. 95
3.2 Schematic of apparatus for simultaneous measurement of length and resistivity during sub-T_g annealing. 97
3.3 Photograph of apparatus for simultaneous measurement of length and resistivity during sub-T_g annealing. 98
3.4 Scheme of the solenoid magnet with a water cooling jacket. 99
3.5 LVDT response as a function of displacement. 107
3.6 Schematic of the four terminal AC bridge employed for resistivity measurement. 108
3.7 Scheme of the data capture and control peripherals. 110
3.8 Photograph of the supporting electronics. 111
3.9 Control pulse schedule for a sub-anneal. 113

4.1 Fractional change in length vs annealing time, for the various isothermal annealing temperatures indicated. 116
4.2 Fractional change in resistivity vs annealing time, for the various isothermal annealing temperatures indicated. 117
4.3 Fractional change in length vs $\ln(t)$, for the various isothermal annealing temperatures indicated. 118
4.4 Fractional change in resistivity vs $\ln(t)$, for the various isothermal annealing temperatures indicated. 119
4.5 $\tau p_o(\epsilon_o)$, inferred from length measurements, vs temperature T. 122
4.6 $\tau p_o(\epsilon_o)$, inferred from resistivity measurements, vs temperature T. 123
4.7 Heat flow curve for $Fe_{40}Ni_{40}B_{20}$ (Scott, 1981). 124

4.8 Relation of surface bend strain at fracture E_f, of amorphous $Fe_{40}Ni_{40}P_{14}B_6$, to the annealing temperature (Kimura and Ast, 1980). 127
4.9 Decay of the total enthalpy in Region I and decay of the local microstructure strain in Stage I, for $Fe_{40}Ni_{40}P_{14}B_6$ (Kimura and Ast, 1980). 128
4.10 Plots of the annealing times, required to reach various fracture strains in $Fe_{40}Ni_{40}P_{14}B_6$, as a function of $1/T$ (Kimura and Ast, 1980). 130
4.11 A profile of $p_o(\epsilon_o)$ vs ϵ (Ascasibar and Hernando, 1985). 132
4.12 Reorientation of pairs of metal atoms in the neighbourhood of a free volume. Big empty circle = iron atoms, big shaded circle = nickel atoms, small circles = metalloid atoms (Kronmuller and Moser, 1983). 134
4.13 MAE relaxation spectra of several FeNiB alloys (Kronmuller and Moser, 1981). 135
4.14 Movement of metalloid atoms in a Bernal Polyhedra (Bernal, 1960). . . . 137
4.15 $-(\Delta P/P_o(\ln(t) = 0))/\tau$ vs T, inferred from length measurements. 139
4.16 $-(\Delta P/P_o(\ln(t) = 0))/\tau$ vs T, inferred from resistivity measurements. . . 140
4.17 Fit for length measurements. 142
4.18 Fit for resistivity measurements. 143
4.19 $\Delta L/(L_o \ln(t))$ vs T. 146
4.20 $\Delta R/(R_o \ln(t))$ vs T. 147

5.1 Normalised Arrhenius graph of measured diffusion coefficients in metal-metalloid amorphous alloys (Cantor and Cahn, 1983). 156
5.2 A hypothetical diagram of the free energy for various phases versus B concentration (Koster and Weiss, 1975). 158

Chapter 1

Introduction

1.1 Historical Review

Historically, the first range of amorphous metallic alloys, based on vapour deposition, was fabricated by Kramer (1934). This was followed by the electro deposition of nickel-phosphorus amorphous alloys by Brenner *et al* (1950). The alloys produced by both the methods mentioned above showed only one diffuse X-ray peak, as expected of an amorphous alloy. Such alloys were used extensively for many years as hard wearing and corrosion resistant coatings. It was not until 1960 that the first production of amorphous alloys, by direct quenching from the melt, was realized by Pol Duwez and his colleagues Klement and Willens, at the California Institute of Technology. An account of this discovery is given by Duwez (1967), where by means of 'splat' cooling against a cold copper substrate, which provides for a high cooling rate, an alloy of gold and silicon with nominal composition $Au_{81}Si_{19}$ was produced. This material was established to be non-crystalline; i.e. lacking both translational spatial periodicity and short range compositional homogeneity. Although this Au-Si alloy was produced in small quantity, and also found to be unstable at room temperature, the achievement added an important

new dimension to both metal and glass science.

Quenching is generally defined as a process of rapid cooling. The main purpose of quenching is to cool an alloy at a high enough rate so that phases that are stable at higher temperatures are retained and remain as metastable phases at lower temperatures. Subsequent heat treatments (annealing) can then be used to control their relative concentration, and also their microstructure, to achieve the optimum physical properties of the final product. In the quenching of alloys, the aim is to rapidly cross the phase boundaries so as to prevent or reduce equilibrium reactions from occurring. In quenching from the liquid state, the critical phase boundaries are the liquidus and solidus boundaries. The primary motivation for the use of high cooling rates, by Duwez and his colleagues (Duwez, 1967), was to prevent the separation of a binary alloy system into separate phases. Subsequent studies have also emphasized the limitations placed by the nature of chemical bonding on cooling rates. For instance, glass formation occurs easily in some classes of non-metallic materials such as silicates and organic polymers, whereas metals which have non-directional bonds, such that atomic rearrangements occur more rapidly, do not readily form glasses. Relatively high cooling rates ($> 10^5$ K/s) must, therefore, be used to form metallic (metal/metalloid) glasses.

Giesen and Wagner (1972) reviewed the structure and properties of amorphous metallic phases produced mainly by quenching from the melt. Jones (1973) provided a compilation of developments in splat cooling and metastable phases that includes an analysis of the methods available for quenching from the melt, the structural features obtained in both metastable crystalline and amorphous phases, the response of the as-quenched structures to annealing (relaxation), and the properties and applications of splat cooled alloys. The structure of alloy glasses, derived experimentally and theoretically, was discussed by Cargill (1975), and the formation and stability of the amorphous structure was reviewed by Takayama (1976). A more complete review reflecting the sta-

tus of our general understanding of the structure, transformation kinetics, mechanical properties, electrical properties and corrosion resistance have been given by Chen (1980). Other less extensive reviews include those by Cahn (1980) and Chaudhari *et al* (1980).

Extensive reviews have also been written covering, specifically, the magnetic properties of amorphous metallic materials (see, for example, Egami *et al* (1975) and Gyorgy *et al* (1976)). Due to the lack of long range ordering it was earlier believed that ferromagnetism could not exist in amorphous solids (Luborsky, 1983). Gubanov (1960), however, theoretically predicted that certain amorphous solids can be ferromagnetic. The electronic band structure of crystalline solids does not change significantly on transition to the liquid state, implying that the band structure is dependent on short-range rather than long-range order. The retention of ferromagnetism in amorphous ferromagnetic solids should then be expected. This was experimentally verified by Mader and Nowick (1965) on vacuum deposited Co-Au alloys and thereafter by Tsuei and Duwez (1966) on splat cooled $Pd_{68}Co_{12}Si_{20}$ and $Pd_{75}Fe_5Si_{20}$ alloys. The first alloy with a substantial ferro-magnetization, further confirming Gubanov's prediction, was $Fe_{83}P_{10}C_7$ reported by Duwez and Lin (1967). This alloy appeared to have 'soft' ferromagnetic properties with a saturation magnetization of the order of 0.7 T and a relatively low coercive field of the order of 240 A/m. However, the early amorphous alloys of Co-P, prepared by vapour deposition methods, had coercivities as high as 800-1600 A/m. These high coercivities arise from compositional inhomogeneities, as demonstrated by Chi and Cargill (1976) using small angle X-ray scattering analysis. The early splat melted alloys of Fe-P-C although compositionally more homogeneous still, however, reflect coercivities many orders of magnitude higher than the commercially available Fe-Ni alloys. This is attributed to the large strain introduced by rapid quenching using the splat technique. Amorphous alloys of Fe-Ni-P-B prepared as ribbons using a melt spinning technique (see Section 1.3) exhibits coercivities of the order of 8 A/m. Luborsky *et al* (1975) demonstrated that a

reduction of the coercivity in these alloys down to less than 0.8 A/m can be obtained by suitable annealing and showed that the changes in coercivity were well correlated with the relief of internal strains.

With the development of uniform long ribbon specimens (Pond and Maddin, 1969), using 'Rapid Quench Planar Casting' (RQPC, see Section 1.3), other interesting properties such as the high tensile strength and the excellent corrosion resistance in certain alloys has drawn further attention to these materials. Amorphous magnetic alloys are relatively resistant to plastic deformation and hence do not lose their high permeability on handling. The electrical resistivity of metallic glasses are relatively high, and together with the inherently low internal stress fields which allow for the easy movement of domain walls (Bloch walls), make them most suitable for low loss transformer core applications and fast pulse compressors. It is established that these materials have power losses, in transformer applications at 50-60 Hz, that is much lower than those of the best commercial crystalline Fe-Si alloys. Large scale production of rapidly solidified ribbon strips (Pond and Maddin, 1969) resulted in amorphous metals moving from being a laboratory curiosity to an important large scale commercial exploitation. Subsequently, extensive developments of the production technology have resulted. Other interesting properties and their commercial exploitation are outlined in Section 1.4.

Amorphous alloys obtained at quenching rates greater than 10^5 K/s possess a large frozen-in disorder and are, therefore, not in an internal equilibrium ground state. As a result, these alloys relax structurally by thermally activated atomic rearrangements. The term 'structural relaxation' is generally used to indicate this process and must be clearly distinguished from crystallization. Associated with structural relaxation, many physical properties change; some significantly and others only slightly. Although the change in density associated with structural relaxation is small (Chen, 1978), approximately 0.5%, an appreciable change has been observed in many other properties, for example, Young's

modulus (Chen, 1978) by approximately 7%, enthalpy (Chen and Coleman, 1976) by 200-300 cal/mole, Curie temperature (Chen *et al*, 1976) by as much as 40 K, and electrical resistivity (Balanzat, 1980) by approximately 2%. Super-ambient temperature annealing also reduces the internal friction (Berry and Pritchet, 1973), rates of stress relief (Williams and Egami, 1976) and magnetization processes (Luborsky, 1976). Consequently, an understanding of the stability and structural relaxation process has drawn great interest for the realization of potential applications. A number of papers on this subject have appeared (see, for example, Chen (1980) for a general review).

In the present investigation we have carried out studies on resistivity and density relaxation to elucidate the structural relaxation kinetics. We present first a general framework of the physics of amorphous alloys inclusive of the formation criteria, glass production techniques, structural features and relaxation dynamics. This is followed by a review of structural relaxation models and of the experimental data. A new model for structural relaxation kinetics, within the framework of Primak's theory (Primak, 1955), for processes distributed in activation energies, is proposed and its implications in respect of the relaxation behaviour in amorphous metal/metalloid alloys is considered.

1.2 Glass Formation Criteria

There is some confusion in the literature concerning the use of the terms 'amorphous' and 'glassy'. Although we tend to use them interchangeably, a material is defined as 'amorphous' if it does not possess long range order characteristic of a crystal structure, and 'glassy' if an amorphous solid exhibits a glass transition. Glass transition is the phenomenon in which a solid amorphous phase exhibits a gradual change in derivative thermodynamic properties (Elliot, 1984). The glass transition is discussed in greater detail in Section 1.2.1. Note that glassy solids are a special subset of amorphous materials,

i.e. all glasses are amorphous but not all amorphous solids are necessarily glasses.

The configurational organization of atoms in a glass, and hence many of its physical properties, depend on the formation and subsequent thermal ageing history of the glass. When certain liquid metal alloys are cooled sufficiently rapidly, the resulting solid is atomically disordered, i.e. glass-like rather than crystalline. As the alloy is quenched rapidly from $T > T_m$, where T_m is the melting temperature, a temperature is reached where, due to the reduced atomic mobility, a non-equilibrium metastable configurational distribution of the constituent atoms is frozen in. This temperature is loosely defined as the glass transition temperature T_g, which shows a marked dependence on the cooling rate (Cohen and Grest, 1979).

Rapid quenching of the melt requires that it be cooled at a sufficiently high rate to avoid a significant degree of crystallization, so that the 'disordered' atomic configuration of the liquid state is partially frozen-in. This is practically realizable because of the existence of an energy barrier to the formation of crystal nuclei (nucleants). The growth rate for crystals once nucleated in metallic melts are rapid and, where the rate of heat removal to the surroundings is small, rapid atomic rearrangements occur. If, however, the liquid is cooled rapidly by heat removal to a sink, the influence of nucleants is increasingly delayed as the cooling rate increases, and the undercooling is also enhanced. The degree of undercooling that occurs depend on several factors, including:

1. the initial viscosity of the liquid,

2. the rate at which the viscosity increases with decreasing temperature,

3. the temperature dependence of the free energy difference between the undercooled liquid and the crystal phase, and

4. the imposed cooling rates.

Owing to these complexities, several criteria for glass formation have been proposed. These include the kinetic (Uhlmann, 1972) and the free volume (Cohen and Turnbull, 1959) criteria which are discussed below.

1.2.1 Kinetic Criterion

Depending on the cooling rate, when a liquid alloy is solidified, one of two events may occur. These events are illustrated in the volume-temperature diagram shown schematically in Figure 1.1. The liquid may solidify

1. discontinuously to a crystalline solid (at T_m) or
2. continuously, with a gradual reduction in slope dV/dT near $T = T_g$, to an amorphous solid.

It is found that the higher the rate of cooling, the larger is the regime for which the liquid may be supercooled, and hence the lower is the glass transition temperature, for example, in silica-based glasses the change in T_g for different cooling rates may be as much as 100-200 K for T_g in the range 600-900 K (Elliot, 1984).

Certain extensive thermodynamic variables (volume V, entropy S and enthalpy H) are continuous through the glass transition but exhibits a change of slope there. This implies that at T_g there should be a discontinuity in derivative variables, such as the coefficient of thermal expansion $\gamma_T = \left(\frac{d\ln(V)}{dT}\right)_p$, bulk compressibility $\kappa_T = -\left(\frac{d\ln(V)}{dp}\right)_T$ and heat capacity $C_p = \left(\frac{dH}{dT}\right)_p$. This is indeed observed, and the behaviour of the heat capacity is shown in Figure 1.2.

The definition of the order of a transition, in the so-called Ehrenfest scheme, is the order of the lowest derivative of the Gibbs Free Energy which shows a discontinuity at a transition point. Thus the liquid-crystal transition is of first order, whereas a glass transition is a manifestation of a second-order phase transition. This rather simple model

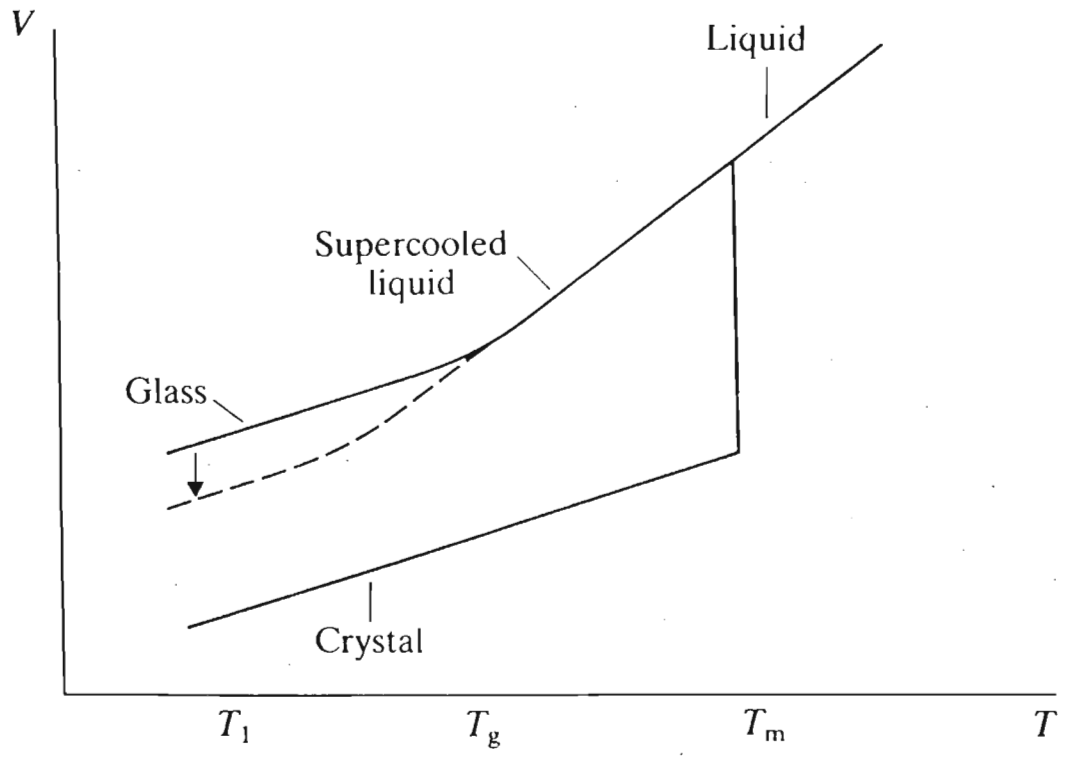

Figure 1.1: A graph of Volume versus Temperature during rapid quenching. The vertical arrow illustrates the volume change accompanying structural relaxation of the glass if held at temperature T_l

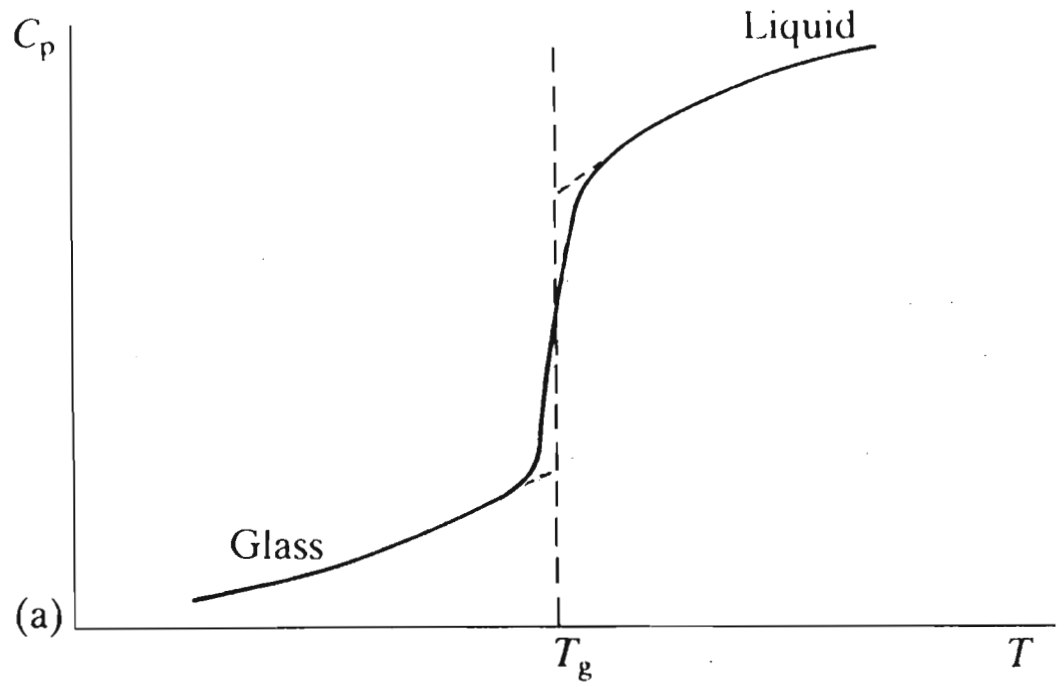

Figure 1.2: A graph of Heat Capacity C_p versus Temperature depicting the glass transition.

of the glass transition, however, fails in several respects. We have already noted that the glass transition temperature T_g is a function of the thermal ageing history and of the cooling rate, to which the melt is subjected. One would not expect changes of this nature in the transition temperature due to simple kinetic factors in a thermodynamic phase transition. Prigogine and Defay (1954) showed that the ratio

$$R = \frac{\Delta\kappa_T \Delta C_p}{TV(\Delta\gamma_T)^2}$$

is equal to unity if a single ordering parameter determines the position of equilibrium in a relaxing system. If more than one ordering parameter is responsible, then $R > 1$. The latter case is found for most glasses and, therefore, one parameter models, although capable of explaining some of the phenomenology, is an oversimplification.

A related kinetic approach was considered by Uhlmann (1972) for a number of non-metallic glasses, where account was taken of the degree of crystal growth. This approach was adopted by Davies *et al* (1974) for some selected metallic glass formers and subsequently extended and generalized for metallic systems (Davies and Lewis (1975), Davies (1975)). Following the treatment of transformation kinetics, the fraction of a transformed phase x in time t, for x small, is given by the so-called Johnson-Mehl-Avrami expression (Davies, 1983):

$$x \sim \pi I_v U_c^3 t^4/3, \tag{1.1}$$

where I_v is the homogeneous nucleation frequency and U_c is the crystal growth velocity. U_c is usually expressed (Davies, 1983) by

$$U_c = \frac{kTf}{3\pi a_o^2 \eta}\left[1 - \exp\left(\frac{-\Delta T_r \Delta H_f}{kT}\right)\right], \tag{1.2}$$

where f is the fraction of sites at the crystal surfaces where atomic attachment can occur, a_o is the mean atomic diameter, η is the viscosity, ΔH_f is the free enthalpy change, ΔT_r is the reduced undercooling temperature $(T_l - T)/T_l$, T_l is the liquidus temperature and

k is Boltzman's constant. The expression used for I_v is based on the free enthalpy of crystallization, which is given (Davies, 1983) by

$$I_v = \frac{kT\bar{N}_v}{3\pi a_o^3 \eta} \exp\left[\frac{-1.07}{\Delta T_r^2 T_r^3}\right], \tag{1.3}$$

where $\bar{N}_v$ is the average volume concentration of atoms and T_r is the reduced temperature T/T_l. The pre-exponential constants in Equations 1.2 and 1.3 are derived on the assumption that the atomic diffusivity is identical across the liquid-nucleus and the liquid-crystal interfaces and are related to the viscosity η by the Stokes-Einstein relationship. On substitution for I_v and U_c, from Equations 1.2 and 1.3 into Equation 1.1, the time t to achieve a small fraction of crystal x is given by

$$t \sim \frac{9.3\eta a_o^2 x}{kTf^3\bar{N}_v}\left[\exp(1.07/\Delta T_r^2 T_r^3)/(1-\exp(-\Delta H_f \Delta T_r/kT))^3\right]^{\frac{1}{4}}. \tag{1.4}$$

A time-temperature-transformation (T-T-T) curve can now be computed from Equation 1.4, where the time t is expressed as a function of T_r for the time required to transform a detectable fraction of crystal, which is arbitrarily set to $x = 10^{-6}$. Computed T-T-T curves for Ni and three additional alloys, $Pd_{82}Si_{18}$, $Pd_{78}Cu_6Si_{16}$ and $Au_{78}Ge_{14}Si_8$, are shown in Figure 1.3. The interpolated viscosities η are based on the Vogel-Taumann-Fulcher expression considered in the next section (Equation 1.11). The form of the T-T-T curves and the magnitude of the time t_n at the nose is largely a reflection of the competition between the increasing driving force for nucleation and the decreasing atomic mobility with decreasing T_r. Correction of these isothermal transformation curves for continuous cooling conditions (Grange and Keifer, 1941) yield the continuous-cooling-transformation (C-C-T) curves also shown in Figure 1.3. The predicted cooling rates dT/dt are given by the cooling curves that just avoid interception with the nose of a T-T-T curve, i.e. $dT/dt \sim (T_l - T_n)/t_n$ where T_n is the temperature at the nose. The values of dT/dt for Ni, AuGeSi, PdSi and PdSiCu alloys are approximately 10^{10}, 10^6, 3000 and

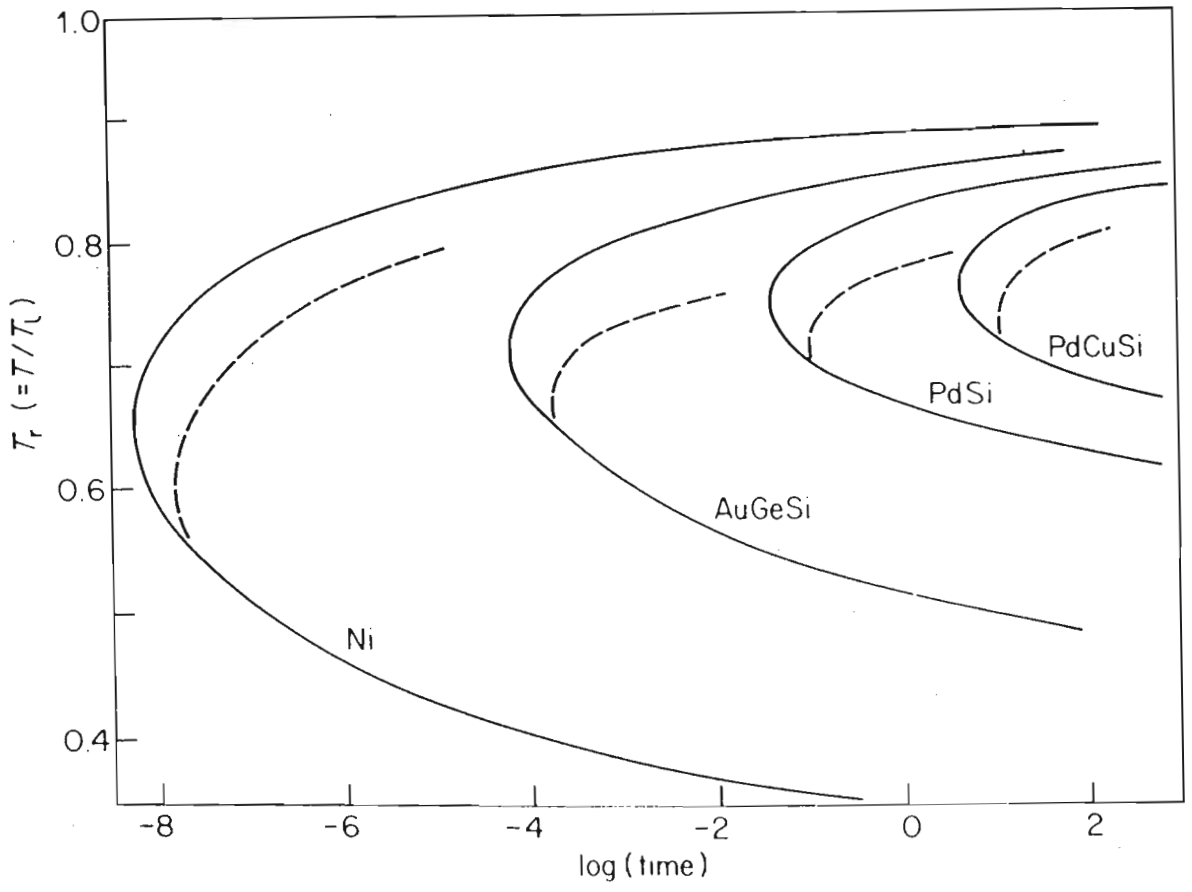

Figure 1.3: Time-Temperature-Transformation curves (solid lines) and the corresponding Continuous-Cooling-Transformation curves (dashed lines) for Ni, $Au_{78}Ge_{14}Si_8$, $Pd_{82}Si_{18}$ and $Pd_{78}Cu_6Si_{16}$ (Davies, 1983)

35 K/s, respectively (Davies, 1983). These estimates, for the binary and ternary alloys, are in reasonable agreement with experimental observations.

1.2.2 Free Volume Criterion

Batschinski (1913) suggested that the product of the shear viscosity η and the total thermal expansion $(V - V_o)$ of a liquid, where V is the volume of the material at any temperature T and V_o its volume at a reference temperature T_o, is a constant, i.e.

$$\eta(V - V_o) = \text{Constant}. \tag{1.5}$$

Subsequently, Doolittle (1951) showed that the shear viscosities of simple hydrocarbons are better expressed by a nonlinear expression of the form

$$\eta = A\exp\left(\frac{BV_o}{V - V_o}\right), \tag{1.6}$$

where A and B are empirical constants and the latter is of the order of unity, and V_o is the volume at $T = 0$ K.

Equations 1.5 and 1.6 result in a rather vaguely defined, but useful, concept of 'free volume', $V_f = V - V_o$. The difference between the properties of liquids and solids are partly attributed to the large free volume of liquids. V_f at any given temperature is often expressed as a function f_T of the total volume at absolute zero temperature, namely

$$f_T = (V - V_o)/V_o. \tag{1.7}$$

Substituting for f_T into Equation 1.6 leads to

$$\eta = A\exp(B/f_T), \tag{1.8}$$

which is known as the Doolittle equation (Doolittle, 1951). Theoretical basis for the free volume V_f was provided by Beuche (1959) and Cohen and Turnbull (1970). Beuche

(1959) assumed that atomic vibrations in a liquid occasionally open up voids large enough to permit an atomic jump. The creation of a void requires the cooperative movement or vibration of a number of atoms. At high densities and low temperature the formation of the required voids becomes increasingly difficult and the undercooled liquid exhibits a glass transition. Cohen and Turnbull (1970), on the other hand, started with the assumption that atomic transport in a hard sphere fluid becomes possible only when a void of volume greater than a critical value is formed. The critical void is postulated to arise from a redistribution of the free volume without changes in energy at constant volume. For $T \ll T_g$ the density fluctuation capable of redistributing the free volume is minimal. On increasing the temperature, however, a rapid increase in free volume results and is redistributed over the entire sample. Cohen and Turnbull (1959) relate the self diffusion constant D to the probability $p(V)$ of finding a free volume between V and $V + dV$ by the following equation

$$D = gU \int_{V_C}^{\infty} a(V)p(V)dV, \tag{1.9}$$

where g is a geometric factor with magnitude $\frac{1}{6}$, U is the kinetic velocity given by $(3kT/m)^{\frac{1}{2}}$, k is Boltzman's constant and m is the mass of an atom. The probability $p(V_c)$ of finding a free volume exceeding a critical volume V_c is obtained by maximizing the number of ways of distributing the free volume. Such a procedure results in the expression

$$D = \frac{1}{6}a^* U \exp\left(-\gamma \frac{V_c}{V_f}\right), \tag{1.10}$$

where a^* is approximately equal to the molecular diameter and γ is an overlap factor that corrects for the overlap of adjacent voids and lies in the range $\frac{1}{2} < \gamma < 1$. Equation 1.10 is shown to be valid in the high density regime where $V_c \gg V_f/\gamma$ (Cohen and Turnbull, 1970).

The above model was originally developed for fluids which are assumed to be composed of hard spheres which oscillate in cages corresponding to their atomic sites (Cohen

and Turnbull, 1959). The total volume is then divided into that part occupied by the spheres V_{occ} and that in which the spheres are free to move. The latter volume, permitting diffusive motion, is termed the 'free volume'. In essence, it is assumed that atomic transport can only occur when the free volume is greater than a certain critical value. As the temperature of the liquid is lowered, V_f is expected to decrease. Redistribution of the free volume ceases when the glass is formed. Thus, the glass transition occurs when V_f falls below some critical threshold (Fox and Flory, 1954).

Assuming that the thermal expansion is linear in temperature and inserting into Equation 1.6, results in the so called Vogel-Tammann-Fulcher expression (Wong and Angell, 1976)

$$\eta = A\exp[a/(T - T_o)], \tag{1.11}$$

where a is a constant and T_o represents a critical temperature at which a singularity occurs. This relationship has been successful in accounting for the relaxation behaviour of many glasses. Shown in Figure 1.4 are the viscosities of a variety of organic glasses as a function of the reduced reciprocal temperature T_g/T (from Wong and Angell, 1976).

Although the free volume model is appealing and simple, it has some shortcomings. These are related in part to the use of the hard sphere model and the assumption of non-directional bonds. The model, however, is applied to certain glass systems which are strongly covalent and almost certainly possess directed bonds.

1.3 Amorphous Alloy Fabrication

Since amorphous alloy fabrication techniques do not fall within the scope of this thesis, only a brief overview will be presented. The preparation and stability of amorphous alloys depends on various kinetic barriers for the growth of crystal nuclei, if nuclei are present, or on nucleation barriers which hinder the formation of crystalline phases. Co-

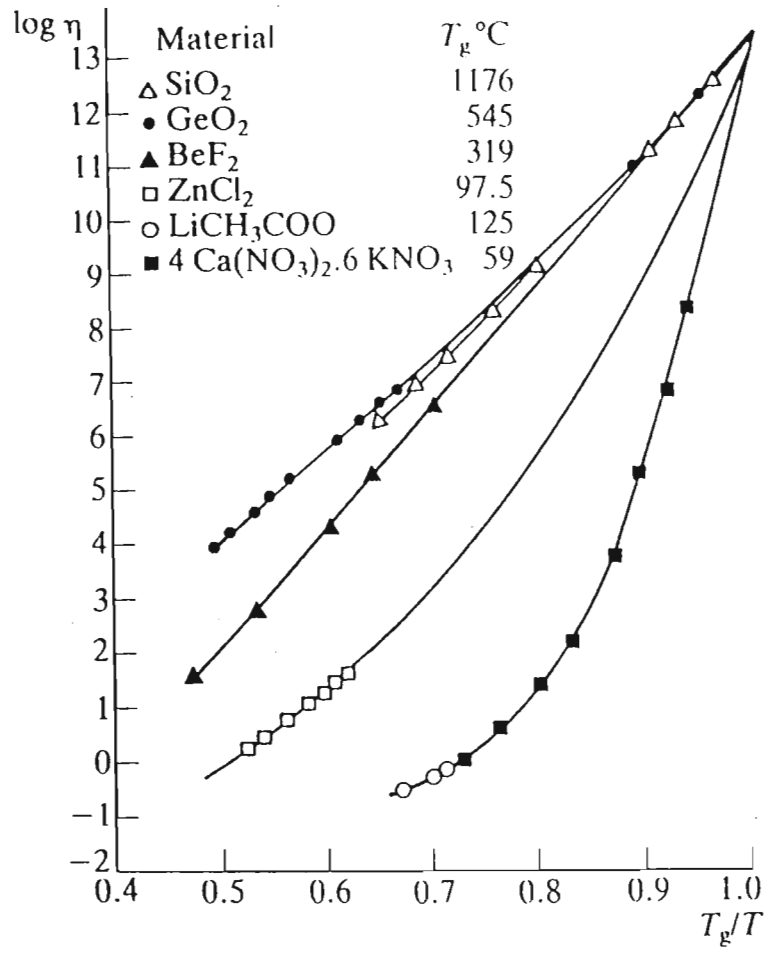

Figure 1.4: Viscosities ($log\eta$) of a variety of organic glasses as a function of reduced reciprocal temperature $\frac{T_g}{T}$. The curves have been normalized such that the glass-transition temperature is defined to be $\eta = 10^{13}$ poise (Wong and Angell, 1976)

hen and Turnbull (1964) have discussed the origins of these barriers and their dependence on the parameters of the material. Alloys produced by rapid quenching from the melt are primarily controlled by the specimen thickness and the nature of the interfacial contact between cooling substrate and sample (Jones, 1973). Calculations by Ruhl (1967) have shown that the average quench rate varies inversely with the square of specimen thickness for ideal cooling or as the inverse of thickness for Newtonian (interface-controlled) cooling. Aside from the high quench rates, the ability to undercool the melt to such an extent that subsequent recalescence does not cause morphological destabilization of the as-quenched sample is an important factor.

High quench rates can be achieved by promoting rapid heat removal from the bulk. The simplest means by which this may be achieved is by maximizing the contact area between the melt and cooling medium by rapidly increasing the liquid alloys surface area. This may be effected either by altering the shape of the melt during processing (for example, splat quenching and melt spinning) or by physically segmenting the melt by various means (for example, atomization). The morphology and characteristics of some rapidly quenched amorphous and crystalline alloys have been shown to depend significantly on the sample preparation method used (see, for example, Wood *et al* (1974) and Chi *et al* (1978)).

There are several techniques commonly used to prepare amorphous alloys. A common rule of thumb is that the faster the rate of deposition or cooling, the further the amorphous solid lies from 'equilibrium'. The common techniques categorized below allow for a variety of different alloys to be prepared.

1. **Vapour deposition** - This involves elements evaporated under vacuum and condensation of their vapours onto a cooled substrate (usually $T \sim 4$ K). The criteria for formation of an amorphous phase by vapour deposition can be described in terms of whether an added atom is prevented from diffusing more than an atomic

distance before it is fixed in position by the arrival of additional atoms. This requires the binding energy of the atoms in the substrate to exceed the kinetic energy of the condensing atoms (Wehner and Anderson, 1970).

2. **Sputtering** - Atoms are removed from the precursor target under bombardment with energetic inert gas atoms and then condensed on a cold substrate. The criteria for formation of an amorphous film by sputter deposition is the same as described for vacuum deposition. The advantage of sputtering is that the deposit composition will be essentially the same as the source material. Sputtering is carried out under partial pressure of an inert gas. This method has been used extensively to prepare rare earth transition metal films.

3. **Chemical or electrode deposition** - In this method ions in aqueous solution are deposited onto a cold substrate by chemical reactions. This method has been used for many years to prepare binary, ternary and more complex amorphous alloys such as NiP, CoP, NiCoP and NiCoFeP. The composition of the product depends strongly on the deposition condition and bath composition during sample formation. Typical bath compositions and deposition parameters may be obtained from reference sources such as Brenner (1963) or Simpson and Brambley (1971).

4. **Splat quenching** - A liquid alloy droplet is squeezed between a rapidly moving piston and a fixed anvil. Two rapidly moving pistons can also be used. The splat-cooled specimen is typically 20-80 μm thick. Such rapid quenching devices are suitable for basic research. The most significant variables in splat cooling are the splat thickness, splat substrate interfacial heat transfer coefficient and the instantaneous splat temperature (Ruhl, 1967). The splat cooling devices seem to give somewhat slower cooling rates than the melt spinning technique described next.

5. **Melt spinning** - In this method a liquid jet of molten alloy is directed onto a rapidly spinning copper, stainless steel or iron wheel, as shown in Figure 1.5, which conducts heat rapidly and continuously away from the melt and produces a thin continuous solidified ribbon. The molten alloy is ejected, at 'relatively' high pressure, through a circular orifice positioned approximately 1 cm away from the cooling substrate. The ribbon is spun off the rotor at speeds exceeding about 1 km per minute. This superficially simple method is in fact quite complicated in respect of the physical mechanism involved. An accurate description of the process is made difficult by the simultaneous occurrence of heat and mass transfer. To this end, empirical relations have been established between process parameters, ribbon width and thickness (see, for example, Lieberman (1980), and Luborsky and Lieberman (1981)). Parameters, including the surface smoothness of the wheel, wheel rotation speed, wheel temperature, temperature of the melt, melt jet diameter, velocity and angle of incidence of the melt, and the nature and pressure of the gas in which the operation takes place must be fixed and kept within certain limits. Care must also be exercised to keep the wheel surface clean of slag and other impurities by operating under an inert gas or in vacuum. This process is suitable for the production of metallic glasses, usually a metal-metalloid alloy system. Melt spun ribbons have typical thicknesses of 20-60 μm.

6. **Rapid quench planar casting (RQPC)** - The basic principle of obtaining metallic glasses by rapid quenching is similar to that of melt spinning. This method differs from the melt spinning technique in that the molten alloy is ejected through a slit situated close to the rotating copper or stainless steel wheel. The melt is not ejected under pressure in this method. After an initial pressure pulse to get the melt flowing, the melt is subsequently entrained out of the slit by the wheel motion. The advantage of this system is that the slit width can be laterally ex-

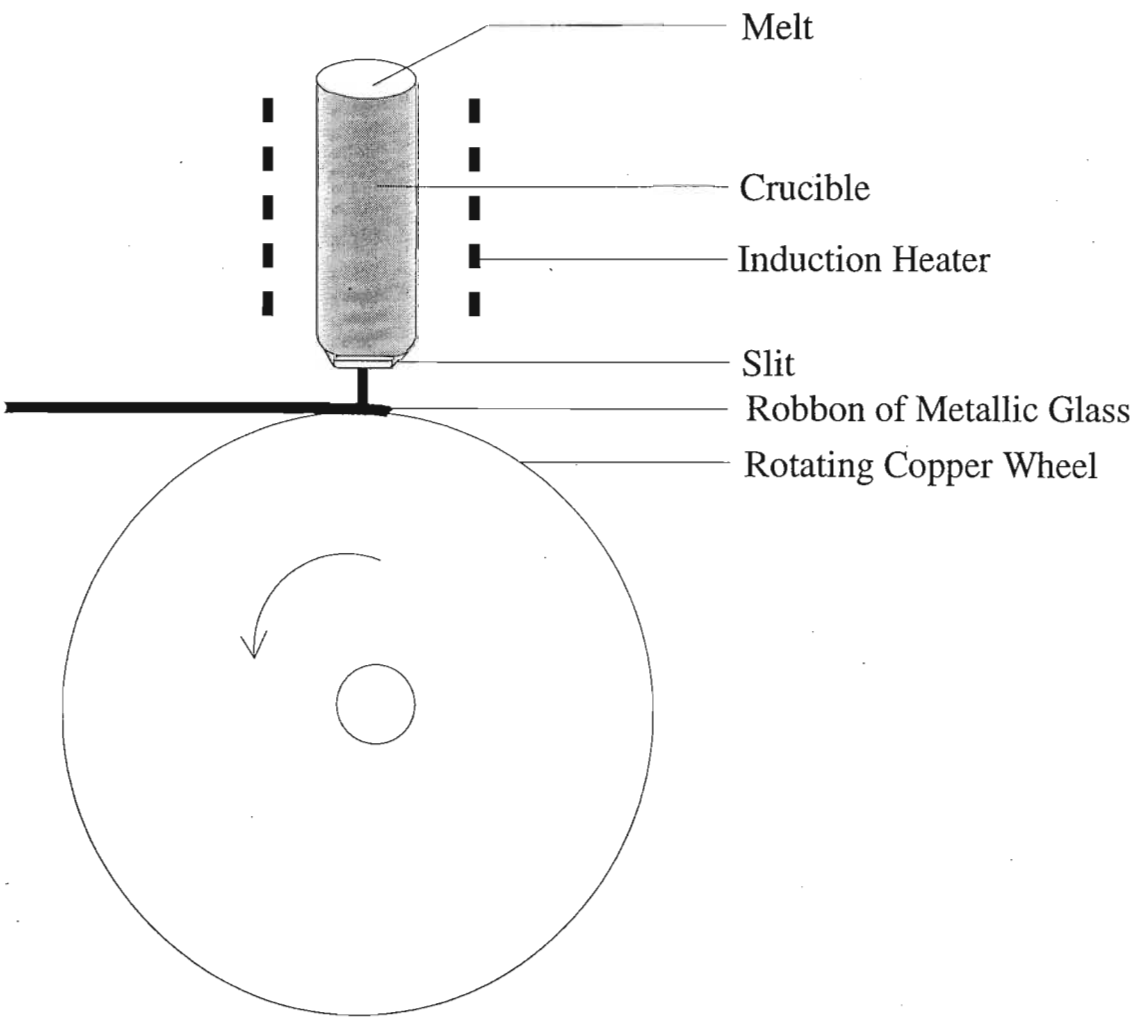

Figure 1.5: Melt Spinning technique for fabrication of ribbon specimens.

tended, thereby allowing the production of wide tapes. Care must, however, be exercised to maintain a fixed nozzle-wheel gap since this significantly affects the ribbon dimension, smoothness and quench rate. The melt-wheel interfacial contact has been studied by Huang and Fiedler (1981). Empirical characterization of the planar flow process has also been performed (see, for example, Takayama and Di (1969)). The cooling rates achieved are usually of the order of 10^6 K/s.

The fabrication techniques described above all have limitations as to quench rate and specimen geometry. For example, although very high quench rates can be achieved with processes such as deposition, the percentage yield is relatively low. This limits such processes to the fabrication of alloys of special composition which cannot be formed by other processing techniques. The atomic short range order and the quenched-in free volume are dependent on the preparation technique used, and on the experimental variables during the fabrication process. Differences in the as-quenched state of amorphous alloys is noted even for otherwise identical samples made by the same method, for example, by melt quenching (Chi *et al* (1978) and Luborsky (1980)). Variability in wheel temperature can, for example, result in a macroscopically inhomogeneous material. This implies that secondary effects associated with the sample preparation details can have a significant effect on the structure and properties of rapidly quenched samples.

1.4 Physical Properties and Applications

Generally, there are three technologically important classes of amorphous alloys, the transition metal-metalloid (TM-M) alloys, the transition metal-transition metal (TM-TM) alloys and the rare earth transition metal (RE-TM) alloys. The TM-M alloys are generally composed of 80 atomic % Fe, Co or Ni, with the remaining 20 % being metalloids B, C, Si, P or Al, and are typically prepared by rapid quenching from the

melt (using the RQPC method). The presence of the metalloid is necessary to lower the melting point, by producing alloys with lower eutectic points, making it possible to quench the alloy rapidly enough through the glass transition temperature T_g. For a eutectic alloy the melting point is depressed and is a minimum at the so called 'eutectic' composition. Glass formation is generally favoured for compositions at which there is a deep eutectic. Compositions near the eutectic favour glass formation since the melting point is depressed and so the liquid is less supercooled at T_g, thereby reducing the possibility of crystallization. Once fabricated the metalloid content also stabilizes the amorphous phase and alters the mechanical, electrical and magnetic properties by, inter-alia, donating electrons to the d-band.

In ferromagnetic amorphous alloys the isotropic character of the material results in low coercivities and anisotropy energies and, therefore, in low hysteresis losses and high permeabilities. These soft magnetic properties are of technological importance. Moreover, since they have been thoroughly investigated, experimental data on TM-M alloys are more complete and informative. It is for this reason that a TM-M $Fe_{40}Ni_{40}B_{20}$ alloy has been chosen for investigation in this thesis. TM-TM and RE-TM alloys will, therefore, not be discussed further.

Due to their atomic disorder and low internal stress fields, amorphous metallic glasses display unusual combinations of electrical, mechanical, magnetic and chemical properties. Although glassy alloys are clearly metallic in character, on the basis of both electrical resistivity and lustre, their properties, in general, are substantially different and in certain respects superior to their crystalline counterparts with the same composition. The most striking aspects of metallic glasses are their high mechanical strength and hardness (Davis, 1978), corrosion resistance (Masumoto *et al*, 1978) and, for certain compositions, their excellent magnetic properties (Graham and Egami, 1978). These attractive properties have stimulated further development of new production processes

and the design and development of improved alloys. It is the intention of the remainder of this section to highlight some of the singular important properties of amorphous metallic alloys and their applications.

Metallic glasses do not exhibit the work-hardening behaviour as found in normal metals; their yielding and fracture can occur almost simultaneously (Kimura and Masumoto, 1983). They also have a high Young's modulus of $E_Y \simeq 100$ GPa, a property which persists almost up to the crystallization temperature. These features make them useful for reinforcements in concrete, plastics, rubber cord material for automobile tyres and flywheels in energy storage devices.

Due to their hardness and corrosion resistant properties they have found use in razor blades and surgical scalpels (Masumoto *et al*, 1978). When Fe-based alloys contain ~9 atomic % Cr, the corrosion resistance is comparable with that of conventional crystalline stainless steel but, when alloys contain phosphorous the resistance to corrosion by a wide range of hostile media becomes substantially better than stainless steel. Such alloys may find applications in the chemical and food industry. Some metallic glasses also have thermal expansion coefficients which are nearly equal to zero, allowing them to be used in precision instruments.

The electrical resistivity ρ of metallic glasses is relatively high and structure sensitive. Typically $\rho \simeq 200$ $\mu\Omega$cm at room temperature (Rao, 1983) compared with $\rho \simeq 2$ $\mu\Omega$cm for copper. Its temperature coefficient can be positive, negative, or approximately zero, depending upon the composition chosen. Below a certain temperature, some alloys have a relatively high temperature coefficient of resistivity and can be used as low temperature thermometers with a sensitivity of about 60 $\mu\Omega$/K.

They have also been used in recorder heads and record disk pick-up cartridges. Some of the projected applications of metallic glasses are magnets for fusion reactors and magnetically levitated trains, and in a variety of magnetic devices such as motors,

generators and sub-transformers for electrical power distribution (Werner, 1981).

It has also been shown that certain metallic glasses can act as good catalysts, gas absorbers and ion-adhesion material (Yokoyama *et al*, 1981). They also possess good wear resistance and low friction coefficients which have created interest in the development of bearings (Davis, 1978). A combination of properties has also created interest in the development of corrosion-resistant reaction vessels having amorphous interior surfaces (Asamo and Hashimoto, 1979).

Interest in amorphous alloys has been sustained to a large degree by the clear benefits seen in the use of these materials in a number of application areas. Potential applications for this interesting class of alloys are far from being fully explored and thus, only a brief summary has been presented here.

1.5 Structural Features

Structural analysis relies on experimental diffraction techniques. Several diffraction techniques, using X-rays, neutrons and electrons, have been extensively used.

Generally, the quantity measured is the scattering interference function or the structure factor $I(k)$, where k is the modulus of the scattering vector. $\mid k \mid$ is related to the angle of the scattered beam 2θ by

$$\mid k \mid = \frac{4\pi}{\lambda}\sin\theta,$$

where λ is the wavelength of the incident beam. $I(k)$ essentially gives the momentum distribution of elastically scattered particles.

The structural arrangement of the atoms in an amorphous solid is given in terms of a radial distribution function $RDF(r)$, which represents the average number of atoms in a spherical shell of radius r, from some chosen atom as origin, and thickness dr. This average is $4\pi r^2 p(r)dr$, where $p(r)$ is the atomic density distribution. The radial

distribution function is then defined by

$$RDF(r) = 4\pi r^2 p(r).$$

Experimentally, the $RDF(r)$ is obtained from the interference function $I(k)$ and is given by

$$RDF(r) = 4\pi r^2 p_o + \frac{2r}{\pi}\int_0^\infty k[I(k) - 1]\sin(\mathrm{kr})dk,$$

where p_o represents the average density of the amorphous sample.

Figure 1.6 (after Ziman, 1979) shows the structural origin of certain features in $RDF(r)$, which can be interpreted physically. The $RDF(r)$ is zero for a distance extending over the core diameter of the atom and then rises to a peak at some typical distance r_o. This distance defines the radius of the first nearest neighbour shell of atoms. The area under the peak

$$z = \int RDF(r)4\pi r^2 dr$$

represents the coordination number of the amorphous structure. Similarly, the next peak defines a second coordination shell of next-nearest neighbours, and so on. Since the number of atoms in each shell becomes uncertain as the peaks broaden, merge with one another and become lost in the continuum background, the coordination becomes less precisely defined at higher orders. This feature of the RDF depicts the typical trend of a structure having short range order but lacking long range order.

The atomic distribution function is sometimes presented in a slightly different form, namely; the partial radial distribution function,

$$G(r) = 4\pi r[p(r) - p_0].$$

$G(r)$ is defined so as to tend to zero at large correlation distances, and thus project any deviation from random coordination. Some typical $I(k)$, $RDF(r)$ and $G(r)$ functions are shown in Figure 1.7 (Cahn, 1980). It is now well established that the majority of amorphous metal-metalloid alloy systems have the following two characteristic features:

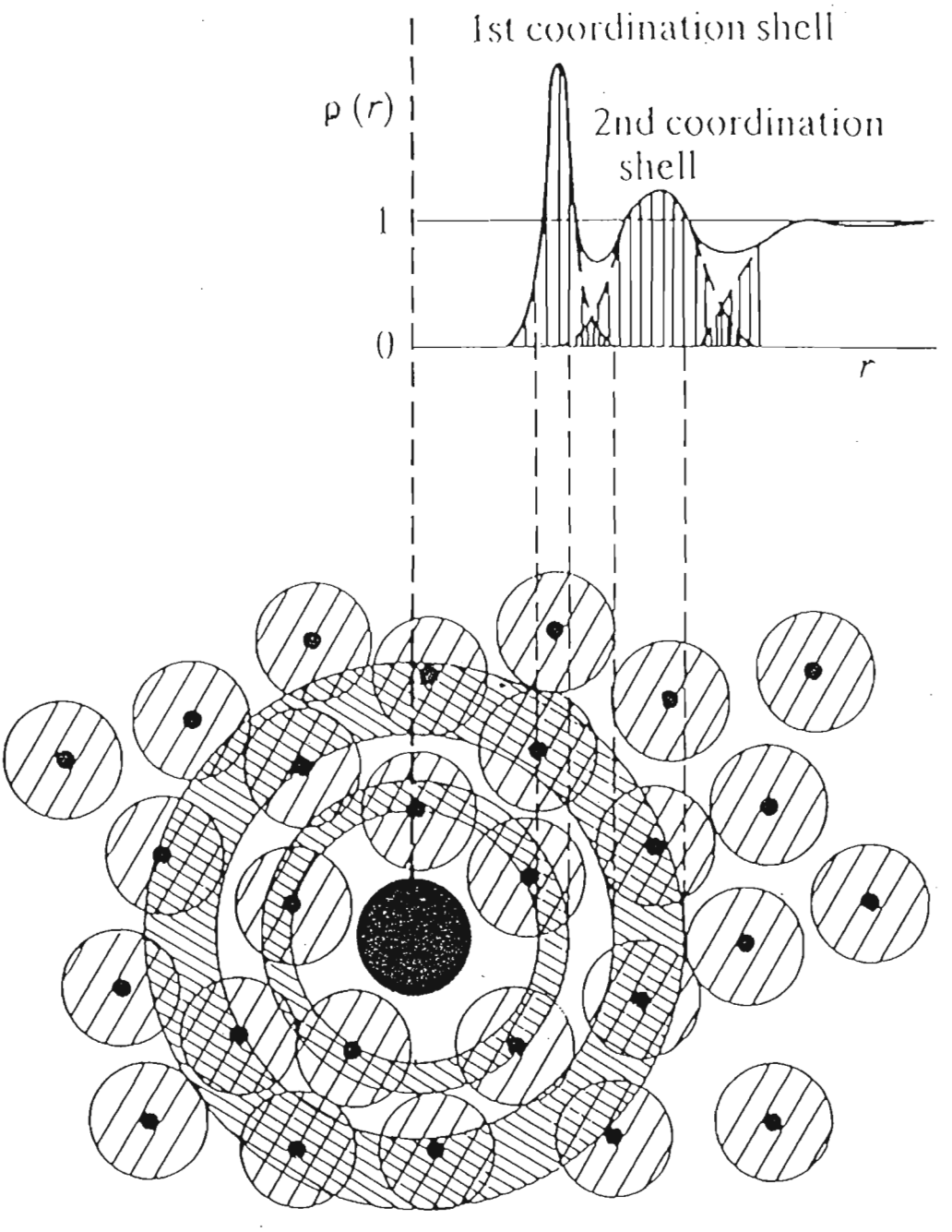

Figure 1.6: Structural origin of the Radial Distribution Function (Ziman, 1979).

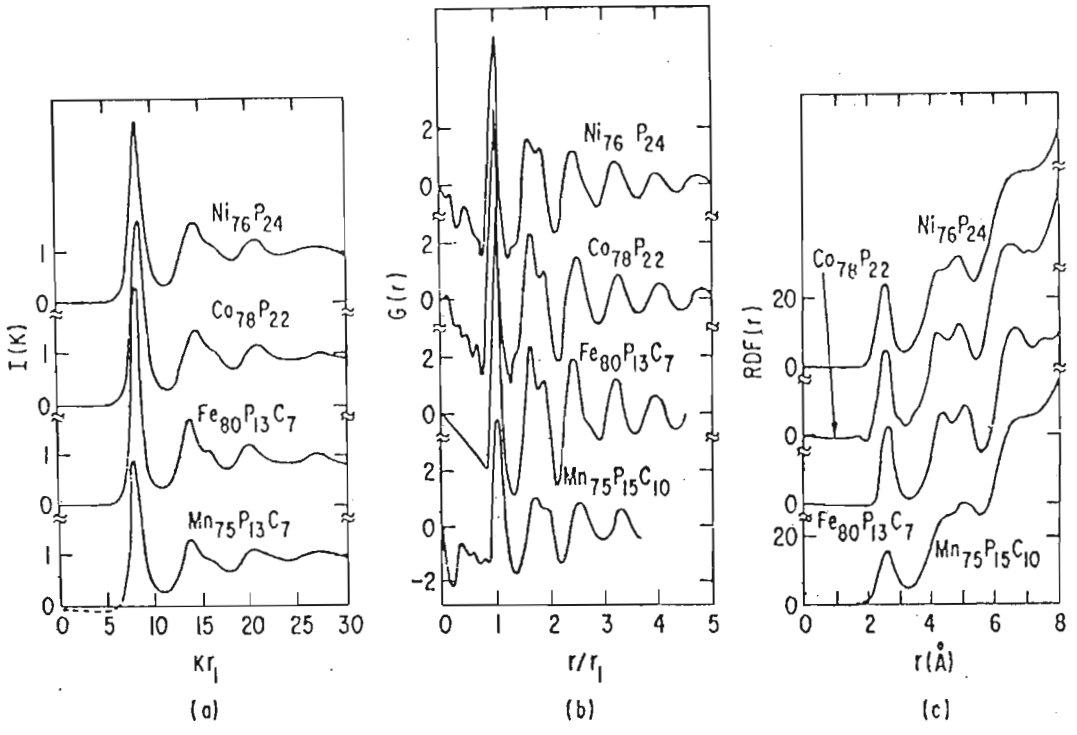

Figure 1.7: Typical plots of $I(K)$, $RDF(r)$ and $G(r)$.

1. a second peak is observed in the interference function $I(k)$,

2. the second peak of the partial radial distribution function $G(r)$ is split, and the first sub-peak is more intense than the second.

Although diffraction experiments help elucidate the microscopic structure of amorphous solids, this information is limited almost entirely to the first two coordination shells. For the case of RDFs derived from experiments on monatomic systems, the problem is that peaks other than the first and second cannot be uniquely associated with a particular interatomic correlation, but are made up of a variety of contributions from the higher lying shells. There are further complications for multi component materials for which a diffraction experiment does not identify the origin of any peak in the RDF in terms of specific atomic pair correlations. Diffraction experiments, therefore, do not yield a three dimensional picture of the atomic configuration and need to be complemented by model structures developed on the basis of topological restrictions. These models are presented in the next section.

1.6 Structural Models

1.6.1 Introduction

Structural models proposed for metallic glasses involve both the 'discontinuous' and 'continuous' random types. In each case, the proposed model falls short of defining all aspects of an amorphous solid. The 'discontinuous' models include the microcrystallite and amorphous cluster models. The microcrystallite model include major drawbacks in that the configuration in the inter-crystalline boundaries are not described (Dixmier *et al*, 1965). Amorphous cluster models, as discussed by Frank (1952) and Hoare and Pal (1975), appear to show lower potential energies than crystalline arrangements. Again,

the problem of the configuration in the boundary region remains unresolved.

In contrast to the microcrystallite and amorphous structure models the continuous random models are homogeneous. The dense random packing of hard spheres (DRPHS), proposed independently by Bernal (1960) and Scott (1962), as a model for monatomic liquids have been applied to amorphous metals. This model can be considered as close packing of a continuous random network structure. Developments of the dense random packing model now use a 'soft sphere' approach, where many of the spheres are allowed to overlap slightly.

1.6.2 Microcrystallite Model

In this model it is assumed that the metallic glass structure can be represented by an agglomeration of randomly orientated microcrystals with

1. strains induced by mismatches of the lattices at the grain boundaries,
2. the presence of a disordered interfacial region, and
3. defects such as dislocations, stacking faults or disclinations within the microcrystallites.

Dixmier *et al* (1965) suggest that amorphous Ni-P alloys can be represented by a model in which the Ni atoms lie in close-packed hexagonal planes, arranged irregularly in domains of less than 2 nm in dimension. These authors find qualitative agreement between the derived X-ray intensity curve and experiment. Upon reexamination of this and several other microcrystallite models, by calculation of the effect on the structure factor of Ni, crystallite size, stacking fault density, uniform dilation and lattice symmetry, Cargill (1970) concludes that simple random-stacking models are inadequate in reproducing all experimental results.

It has been noted that the small difference in density between amorphous and crystalline materials cannot account for the strain associated with grain boundaries. Also, the elastic strain necessary to cause a broadening of the structure factor peaks cannot be correlated with the heat of crystallization. The problems associated with the microcrystallite model are, therefore, considered to be related to the interfacial nature between crystallites. An upper limit for a microcrystallite is 1.5-2 nm and in a cube of this size, about two thirds of the atoms lie within one atom diameter of the microcrystallite surface. The radial distribution function beyond the first nearest neighbour is, therefore, meaningless and moreover, the fit between experiment and model is poor; the microcrystallites produce excessively large oscillations in the RDF for large r. The value of the strain obtained from the breadth of the distribution of nearest neighbour distances amount to 5 % and consequently, the energy associated with the interfaces cannot be large. This model excludes structural relaxation effects since, broken or extensively distorted bonds impose energy restrictions. High energies associated with an interface between crystallites will lead to instabilities with respect to crystal growth. Therefore, energetic considerations of the metallic-glass structure suggests that such a model is incomplete.

1.6.3 Amorphous Cluster Model

An amorphous, or non-crystallographic, cluster model describes an arrangement of atoms having a symmetry element but lacking long-range translational periodicity. The symmetry can be produced using various close-packing arrangements, for example, tetrahedral close packing or trigonal prismatic packing. Certain groupings of atoms possess advantageous energetic or space-filling properties, and it may be reasonable to assume that these groups dominate in a given structure. Hoare and Pal (1972) demonstrate several non-crystallographic clusters which are shown to be more stable than crystalline clusters

with the same number of atoms. In particular, the icosahedron structure, which consists of twelve atoms packed around a central thirteenth atom, is inherently stable and it is believed that this structure may represent an absolute minimum energy configuration for thirteen atoms. Sadoc *et al* (1973), using an algorithm which tends to force a high degree of icosahedrality, found that the resulting interference function shows the characteristic splitting in the second peak.

Tetrahedral close packing, however, is not space filling, and it is found that larger close packed clusters possess considerable strain and, in fact, require a soft potential to preserve their symmetry. If the elastic strain increases to a sufficiently high degree then nucleation of a crystal structure becomes energetically more favourable. To maintain the amorphous cluster arrangements the clusters must be small enough to prevent crystal nucleation. Barker (1977) showed that by combining tetrahedral and octahedral structures, the limitation on cluster size is no longer valid. Finney and Wallace (1981) have shown that while tetrahedrality increases on relaxation, there is no evidence for icosahedral clusters in either the original or relaxed models. While not discounting the possibility of some form of tetrahedral close packing to describe the arrangement of metallic atoms in an amorphous binary alloy, there are arguments in favour of extending the concept to produce trigonal prismatic coordination for metalloid atoms. So far, however, the evidence for trigonal prismatic packing around metalloid atoms is purely circumstantial, and there is as yet little evidence that metallic glasses exist with such structures.

1.6.4 Dense Random Packing Model

Examination of physical properties of physically constructed laboratory models was conducted independently by Bernal (1960) and by Scott (1960). The method involved pouring thousands of spheres into a suitable container, which were then 'kneaded' to facilitate maximum sphere densification. The spheres were then fixed in position, by

pouring molten wax, and the coordinate of each sphere was then noted. Both procedures by Bernal and by Scott were in excellent agreement. Finney (1970) then extended this idea, which was originally intended to be applicable to liquids, to metallic glass systems and calculated the radial distribution function.

The connection between structural models for simple liquids and experimental data for amorphous solids became more evident when Cargill (1970) compared his RDF data for amorphous $Ni_{76}P_{24}$ with the predictions of Finney's model. Treating the hard sphere radius as a variable fitting parameter, correlation between the experimental and theoretical results were found to be good, specifically in relation to the position of the peaks in the RDF. There are, however, two problems with these fits. Firstly, the relative intensities of the two components of the split second peak are in significant disagreement. This problem was resolved by refinement of the model using soft potentials (Barker *et al*, 1975). Secondly, the identification of a two component real alloy with a single component model is problematic. Although, in the X-ray measurements on $Ni_{76}P_{24}$, the nickel will dominate the scattering, the phosphorous scattering contribution of 8% is significant. Also, with metal-metalloid alloys, it would be difficult for the dense random packed model to reproduce the complex behaviour of the metal-metalloid interaction unless, this property depends on the relative size of atoms and the strength of the interaction alone.

It is appropriate in light of the strong correlation between the experimentally and theoretically derived distribution functions, to highlight the salient features of the dense random packed model, which are as follows

1. In alloys consisting of two elements A and B, the probabilities of AA, BB and AB contacts are independent of the chemical nature of A and B.

2. The spatial arrangement of atoms is random and subject to space filling constraints only.

3. There is no preference for a particular local symmetry or coordination number. The average local geometry is a function of the radius ratio and concentration of each species.

4. The structure is essentially homogeneous and subject only to statistical fluctuations.

The random close-packed hard-sphere model, therefore, does contain the essential consequences of volume exclusion in a non-crystalline structure, and hence can be perceived as a reference structure, which is of importance in the definition of defect structures considered in the next section.

1.7 Structural Defects

1.7.1 Introduction

Comprehensive reviews of structural defects in amorphous materials and their influence on physical properties has been given by Mott (1980) and Robertson (1982). In crystalline materials, the periodic lattice provides a reference structure for the definition of point, line and planar defects. In amorphous materials, however, the identification of defects is less obvious due to the difficulty in defining a defect-free reference state. An unambiguous definition of such an 'ideal' amorphous structure is the (metastable) equilibrium ground-state of the amorphous system at absolute zero temperature. This state must have zero entropy and thus be fully ordered. Although this state is not accessible, Kauzmann (1948) has shown that an extrapolation of the equilibrium properties below T_g gives a vanishing amorphous-crystalline entropy difference at a non-zero temperature. He postulated, under the notion that configurational order can only be achieved by crystalline periodicity, that the amorphous phase would 'spinodally' transform into

a crystalline phase at this temperature. The non-crystallographic and cluster models, however, still possess a high degree of configurational order although amorphous on a larger scale.

The only remaining approach for the model study of defects, therefore, is to make use of the amorphous structures as they are available. In this respect, two routes have been identified, namely

1. an existing model can be analyzed in the hope of identifying defects that have been trapped in it or

2. defects can be introduced in an existing model and their characteristic features can be studied with respect to function, stability and motion.

For example, the first option has been taken by Egami *et al* (1980) who analyze the internal stresses in amorphous clusters and find regions where either hydrostatic pressure, hydrostatic tension or shear stresses dominate. The identification of these regions as defects is problematic since it is not clear which of these stressed regions would be absent in the ideal reference structure. The reference state problem is avoided when route 2 is taken. Defects can be introduced in amorphous model systems either by deformation or by introducing point or line defects directly by appropriate removals and/or displacement of atoms.

Due to the conceptual difficulty in defining an 'ideal' reference state, much of our conception of point and line defects in amorphous solids, vital to our understanding of atomic processes, stems from computer simulation experiments using simple pair potentials. Although the results of these modeling studies are not definite enough to draw broad conclusions about defect stability and mechanism, it is still of interest to discuss them with reference to dynamic relaxation studies, such as those reported in this thesis.

1.7.2 Point Defects

In a crystalline solid a point defect can be readily identified because it represents a deviation from a perfectly periodic lattice. A vacancy maintains its local identity as a missing atom and can only disappear by executing a jump into a vacant position. Consequently, if this process is repeated often enough, the vacancy reaches a sink (for example, a free surface, an edge dislocation, grain boundary etc.) and is annihilated.

Although the definition of a defect-free glass does not exist, a point defect in an amorphous system is recognized as a significant deviation in the local atomic density. The identification of a vacancy with an empty atomic site, in the absence of symmetry, makes it difficult to predict whether the vacancy will remain as a localized unit under structural relaxation. Two methods of tracking the vacant volume, using computer simulation, have been used (Bennet *et al*, 1979). In the first approach an atomic model was sectioned into slices and the time evolution of the vacant volume was studied. In the second approach the volume space between model atoms was monitored. The latter approach allows one to follow the 'annealing out' of a vacancy and vacancy clusters with time. The break-up of a vacancy apparently distributes the extra volume more uniformly within the system. Molecular dynamic calculations carried out at different temperatures show that the 'annealing out' time is a function of temperature. The most effective way of volume removal is, however, by elastic collapse of the vacancy (Spaepen, 1981). At constant pressure the extra volume can also be removed by a process of annihilation. These vacancy annihilation processes are of interest for a macroscopic interpretation of structural relaxation, where the excess volume plays a role in diffusive and shear rearrangements.

1.7.3 Line Defects

Line defects involve only a small deviation in the local density and are, therefore, more difficult to study. The strength of a line defect is conventionally measured by taking a Burgers circuit (Chaudhari *et al*, 1983) around the line defect and measuring its closure deficit. This is obviously not easily achievable in the amorphous state. A common conclusion therefore, is that a line defect in a metallic glass is not a sensible notion. There are, however, various features of line defects that can be measured intrinsically without reference to a defect free system. Identification of a line defect in an amorphous network, associated with Finney's model, has been attempted (Volterra, 1944). The resulting structure is then altered to evolve under either static or dynamic relaxation. This simulation of line defects has established that under certain conditions of static relaxation or low temperature molecular dynamics, simulated stress fields characteristic of dislocations can be present. However, two questions arise, namely,

1. is such a defect stable with respect to structural relaxation and

2. how can such a line defect be detected and characterized in the absence of a periodic lattice if it is stable?

Chaudhari *et al* (1983) have undertaken computer simulation investigations of defects in amorphous dense-random-packed structures. The line defects were visualized using a 'reference net' as an ideal 3D lattice (a cubic lattice for an edge dislocation, or a lattice with cylindrical symmetry for a screw dislocation). They found that unlike atomic point defects, vacancies or self-interstitials, both screw and edge dislocations were stable against structural relaxation.

1.8 Relaxation Phenomena

Following a quench from $T > T_m$ to $T \ll T_g$ the resulting solidified glass is expected to have a structure which may be characterized by the glass transition temperature T_g or, more precisely, by the so-called 'fictive temperature' T_f, which is defined to be the temperature at which the solidified glass is in equilibrium with the supercooled liquid (Jones, 1956). In accordance with this definition T_f would, in general, be an increasing function of quench rate and can, in principle, be reduced from its initial value $T_f \sim T_g$ to some minimum value by suitable sub-T_g ageing. During this latter process the glass undergoes structural relaxation to some 'ideal' optimum relaxed state before the onset of crystallization. The specific volume of a metallic glass is about 1% larger than the corresponding crystalline state. This difference in specific volume, the so-called free volume, plays an important role in determining the physical properties and the degree of structural relaxation of the glass. Thus, structural relaxation is a direct consequence of the rapid solidification process used to produce the amorphous alloy, and has been found to have considerable influence on the measured value of many physical properties. The measured physical property-time-temperature behaviour of amorphous alloys is a complex function of the thermo-mechanical history. The relaxation process can be categorized into three broad classes, namely $\ln(t)$ kinetics, reversibility and crossover which are defined as follows:

$\ln(t)$ - When the changes in a measured property varies linearly with the logarithm of annealing time t, $\ln(t)$ kinetics is said to be obeyed.

Reversibility - Any property change which depends only on the annealing temperature and not on the previous thermal history is said to be reversible.

Crossover - A measured property changes gradually due to annealing at some temperature T_1, for short term annealing. If after some time the temperature is increased to T_2 ($T_2 > T_1$), the recorded property drops below the curve expected for annealing at T_2

and only after some time falls back onto the normal curve. This effect is referred to as crossover.

Structural relaxation within the amorphous phase involves a succession of steps between metastable states that are formed during rapid quenching. Many of the properties, in particular, viscosity, mechanical ductility, magnetic anisotropy, hardness, etc., alter significantly as a result of this relaxation. Consequently, there has been much emphasis on structural relaxation processes and on the stability of metallic glasses, and many reviews on the subject has been published (for example, Chen (1980), Masumoto and Suzuki (1982)). Presented in Table 1.1 is a summary of the characteristic behaviour and the property changes used in their experimental elucidation. These references represent only a summary of the experimental work associated with the various relaxation phenomena.

Complications to the above classifications often arise. Scott *et al* (1981) pointed out that $\ln(t)$ kinetics does not hold over a whole temperature regime when observing stress relaxation in a bend test. The breakdown occurs in the early stages of relaxation, which are experimentally detectable at short annealing times and low annealing temperatures, and in the late stages, which are conveniently studied at higher annealing temperatures.

Breakdown in $\ln(t)$ kinetics is also seen in the usual time-temperature (t-T) regime if the specimen is pre-annealed, i.e. annealed before performing the bend test (Scott *et al*, 1981). Chen (1981a) reported that by choosing a suitable t-T regime, irreversible changes in Curie temperature are superimposed on a reversible change.

There have also been various phenomenological models proposed to explain the processes of relaxation. Any model for relaxation in metallic glasses should account for $\ln(t)$ kinetics under certain conditions and conversely its failure in others; it must also incorporate reversibility and crossover effects and should relate to the structural features of the alloy. A discussion of some of the main relaxation models is presented in Chapter

ln(t)	Reversibility	Crossover
Curie Temperature Mizoguchi *et al* (1981)	Curie Temperature Greer and Spaepen (1981)	Curie Temperature Greer and Leake (1979)
Young's Modulus Scott *et al* (1981)	Young's Modulus Scott *et al* (1981)	Young's Modulus Scott *et al* (1981)
Stress at constant strain Woldt (1980)		
Strain at constant stress Scott *et al* (1981)		
Structure Egami (1978)		
Length Scott *et al* (1981)		
Resistivity Cost *et al* (1981)	Resistivity Cost *et al* (1981)	
	Magnetic anisotropy Chambron *et al* (1980)	
	Specific Heat Chen (1981a)	
		Index of Refraction Ritland (1955)

Table 1.1 : A summary of experimental work on relaxation phenomena.

2 together with the experimental evidence available in support of these models.

1.9 Scope of Thesis

Thus far, the general framework of the physics of amorphous alloys has been presented, where the glass formation criteria, the main preparation methods, the physical properties and potential applications, and the various experimental and theoretical approaches to their characterization have been sketched. In Chapter 2 we present a review of structural relaxation models, some of their shortfalls, and experimental evidence in support of them. The model of Primak (1955), for processes distributed in activation energy, is used as a basis for further development. By incorporating the configurational entropy, a relaxation expression for a quantitative prediction of structural relaxation and a qualitative description of microscopic level processes is produced. Chapter 3 describes the experimental apparatus and procedures for in-situ sub-T_g isothermal and isochronal annealing relaxation experiments on changes in length and resistivity in an amorphous $Fe_{40}Ni_{40}B_{20}$ alloy. Chapter 4 presents the results and discussion of these relaxation measurements in relation to the 'relaxation' scaling equation. Other related effects, including the glass transition, crystallization and diffusion, are considered within the framework of the 'relaxation equation' in Chapter 5. Chapter 6 includes the conclusion and suggestions for future studies.

Chapter 2

Theory

2.1 Introduction

Amorphous alloy specimens exhibit various relaxation effects which preclude the characterization of the glass by any single order parameter. The processes which result in structural relaxation with sub-T_g ageing have not been fully elucidated and are apparently complex. It is expected that these processes involve a spectrum of activation energies and possibly also of activation frequencies. A further complication is the choice of order parameters for the characterization of the relaxation at the microscopic level. The most obvious and indeed early choice of an order parameter was 'free-volume', which may be considered as the 'extra' volume frozen into the glass structure during the quenching process.

The free volume theory, which was originally formulated for the description of liquids and the glass transition, has many similarities with certain aspects of existing relaxation theories. The theory was developed for fluids assumed to be composed of hard spheres undergoing localized thermal oscillations. The total volume of the system is the sum of that 'occupied' by the spheres or molecules, and the remaining volume. This

latter volume, which permits diffusive motion, is termed the 'free volume'.

The free volume model is of considerable value in metallic glass systems where an harmonic, rather than the hard-sphere interatomic potential, is more appropriate. The soft sphere approach allows for regions of both positive and negative relative dilation and also for shear stresses and strains. These regions, which are supposed to contain between 10 and 20 atoms typically, are defined as p_s, n_s and τ_s defects, respectively (Egami *et al*, 1980). The defect density is then defined in terms of some threshold value for the stress associated with an effective defect. Relaxation processes then involve either conservative or non-conservative rearrangements of these defects. The former obviously allows for reversible and the latter for irreversible relaxation phenomena.

The results of relaxation experiments often display approximate $\ln(t)$ kinetics, and this can be understood in terms of various models. Primak (1955) gives a complete treatment for relaxation in systems with a broad activation energy spectrum, which in principle allows for the identification of the order of the relaxation reaction and the determination of an initial activation energy spectrum. The present experiment, in which relaxation of both length and resistivity are simultaneously monitored in a series of isothermal anneals in a suitable metallic glass ($Fe_{40}Ni_{40}B_{20}$), is intended to investigate the Primak theory mentioned above.

2.2 Relaxation Models

2.2.1 A Spectrum of Relaxation Times

Several investigators have studied the kinetics of relaxation in metallic glasses and have reported that the kinetics follow a first-order law with a broad distribution of relaxation times $H(ln\tau_r)$ (see, for example, Balanzat and Hillairet, 1982). The relaxation time τ_r is defined as the time for which the fractional change in a property is reduced by a factor of

$1/e$ (Gibbs *et al* (1983) and Chen (1977, 1981a and 1981b)). A formal equation relating this distribution to a change in a measured property P is given (Chen, 1983) by

$$P(t) - P_\infty = (P_o - P_\infty) \int_0^\infty H(ln\tau_r) \exp\left(\frac{-t}{\tau_r}\right) d(\ln\tau_r), \tag{2.1}$$

where P_o and P_∞ are property values at time $t = 0$ and ∞, respectively. While the description of the relaxation process in terms of a distribution in relaxation times $H(\ln\tau_r)$ is appropriate, the empirical expression

$$P(t) - P_\infty = (P_o - P_\infty) \exp\left[-\left(\frac{t}{\tau_r}\right)^n\right],$$

with $0 \leq n \leq 1$ is often employed. The characteristic relaxation time τ_r is assumed to be dependent on both temperature and on a 'structural order' parameter σ, i.e. $\tau_r = \tau_r(T, \sigma)$. σ is defined by macroscopic properties such as the fictive temperature T_f, the free volume V_f or the configurational entropy S_{conf} (Uhlmann, 1978). It is also noted that the analysis employed for sub-T_g relaxation does not apply for $T \ll T_g$ relaxation. Significant features of the analysis, as noted by Chen (1983), are:

1. The relaxation spectrum $H(ln\tau_r)$ for sub-T_g annealing involves a twofold broad distribution in (i) activation energy ($1 < E < 2.5$ eV) and (ii) frequency factor ($10^{14} < \nu < 10^{22}$ s^{-1}).

2. During $T \ll T_g$ anneals a small portion of the relaxation spectrum is sampled and stabilized. Upon heating, destabilization occurs, and the initial glass structure is recovered, i.e., the effect of the initial annealing is eliminated upon heating.

Woldt and Neuhauser (1980) have studied anelastic load relaxation in metal-metalloid glasses and analyzed the data according to an expression of the form

$$P = P_\infty + \sum_i P_i \exp\left(\frac{-t}{\tau_{ri}}\right),$$

where P_∞ and P_i are load parameters. In this case τ_{ri} is assumed to obey an Arrhenius expression of the form

$$\tau_{ri} = \tau_{ro}\exp\left(\frac{E_i}{kT}\right),$$

where E_i is the activation energy of a process having a characteristic relaxation time τ_{ri}. In the case of load relaxation the weighting factors P_i can be related to structural properties of the specimen (Woldt and Neuhauser, 1980).

2.2.2 Percolation Model

A model, within the framework of percolation theory, has been proposed by Chen (1981b). The model makes the following assumptions:

1. The structure of a glass and a liquid is heterogeneous. The inhomogeneity in monatomic materials arise from fluctuations in density. Cohen and Grest (1979) visualize a glass consisting of liquid-like regions of large free volume or high local free energy and solid-like regions with small free volume or low free energy.

2. Each of these regions undergo relatively infrequent transitions ($\ll 10^{13}$ Hz) between local minima well separated by energy barriers $\Delta\epsilon$ in configuration space (Goldstein, 1969). Each local minima represents a different structure, and a distribution in $\Delta\epsilon$ is responsible for a relaxation time τ_r being proportional to $\exp(-\Delta\epsilon/kT)$.

A relaxation time spectrum $H(\log\tau_r)$ is shown schematically (after Chen, 1981b) in Figure 2.1. The spectrum shows an asymmetric distribution around a central peak and a long tail at shorter annealing times. At temperatures $T_1 > T_g$ (Curve a), the whole spectrum extends only up to the time of measurement τ_r^*, so that the whole system undergoes frequent configurational transformation and is liquid-like. During quenching, the spectrum shifts to longer times such that smaller regions with $\tau_r > \tau_r^*$ behave as isolated solid-like clusters embedded in a liquid-like matrix.

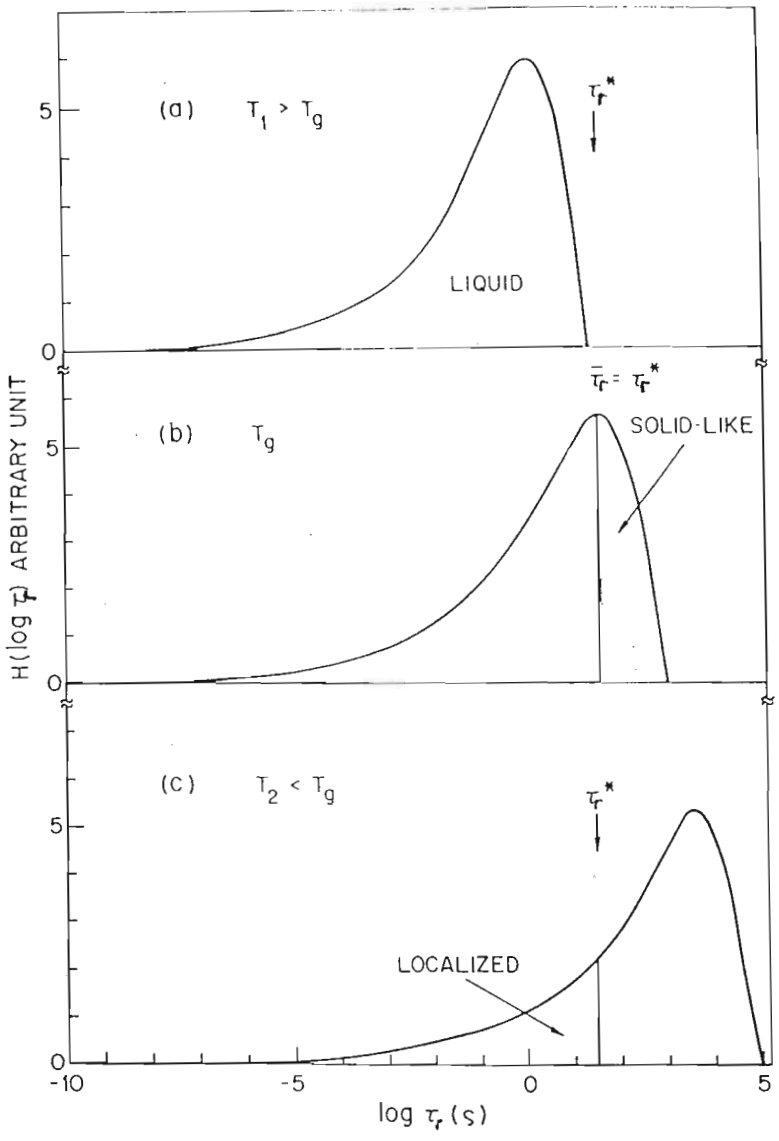

Figure 2.1: Relaxation time spectrum $H(\log\tau_r)$ for a metal glass at various temperatures (Chen, 1981b).

As the temperature approaches T_g (Curve b) the solid-like clusters increase in number and grow in size, and the glass transition is then related to a percolation process. The solid-like regions occupy only a small fraction of the system and are surrounded by a liquid-like matrix. The relaxation processes near T_g are, therefore, cooperative in nature since relaxation involves a number of atoms from the liquid-like matrix.

At a temperature $T_2 < T_g$ (Curve c) the solid like regions grow and the fraction of liquid-like regions decrease to below a percolation limit. The liquid like regions are now isolated from each other and are embedded in a rigid matrix. Relaxation then occurs locally in the liquid regions independent from each other.

This model predicts localized modes of relaxation for $T \ll T_g$ annealing. The model also predicts the concept of a distribution of glass transition temperatures and reproduces fairly well many ageing behaviours.

2.2.3 Short Range Ordering

Egami (1978) recognizes two distinct ordering processes;

1. Topological short range ordering (TSRO), which involves some form of structural reorganization and, in particular, possible elimination or, at least, reduction of free volume, and

2. chemical short range ordering (CSRO), which involves only nearest neighbour chemical reorganization.

Obviously, these two processes will in general make different relative contributions to any particular relaxing physical process. Certain such properties, for example, Curie temperature, magnetic anisotropy, and resistivity are found to have both reversible and irreversible relaxation behaviours at sub-T_g temperatures. The reversible relaxation has been attributed to CSRO, but can involve some species independent diffusion process.

Other properties, including density, within measurement resolution show only irreversible relaxation and are, therefore, associated with the elimination of free volume or TSRO.

Chemical Short Range Ordering

Since metallic glasses are metastable, the state of mixture of the alloy components is an important ordering parameter of the system. Generally, rapid quenching does not result in a completely random mixture, so that the chemical composition around the atoms of each alloying component differs from the average composition. The system is then said to possess chemical short range order. Since the effect of CSRO on observed properties is limited to within the first nearest neighbour shell, the simplest way to define CSRO is to use the deviation from the average in the nearest neighbour composition as a parameter. For a binary A-B alloy system this chemical short range order parameter is called the Warren-Cowley parameter α_p (Warren *et al* (1951) and Cowley (1950)) and is defined as

$$\alpha_p = 1 - \frac{Z_{AB}}{< Z > C_B} = 1 - \frac{Z_{BA}}{< Z > C_A}, \tag{2.2}$$

where Z_{ij} is the number of the i coordination on a j atom, C_i is the concentration of the ith component and $< Z >$ is the average coordination number. This parameter provides a good measure of the chemical affinity.

For more involved studies, the CSRO as a function of distance r from a chosen atom is needed, and this is best described by the composition fluctuation atomic pair correlation function ρ_{cc} (Bhatia and Thornton, 1970),

$$\rho_{cc}(r) = \frac{1}{4\pi r^2} \sum_{ij} \delta(r - r_{ij})(\eta_i^A - C_A)(\eta_j^B - C_B), \tag{2.3}$$

where r_{ij} is the distance between the ith and jth atoms and $\eta_i^A = 1$ if the ith atom is occupied by an A atom and 0 otherwise, and likewise for η_j^B. Although this formulation provides a good definition of CSRO for binary systems, experimental determination of the

parameters involved are difficult. Only a few attempts to measure these parameters have been made for metallic glasses and these include neutron diffraction using an isotopic substitution technique (Mizoguchi *et al*, 1978), X-ray diffraction utilizing the anomalous dispersion (Waseda, 1980) and EXAF measurements (Wong, 1981). The accuracy of these measurements are not high enough to provide an explanation for the physical and chemical properties in terms of the CSRO. It is possible, however, to relate some important changes in properties, due to annealing treatments or mechanical deformation, to changes in CSRO.

Topological Short Range Ordering

In network glasses, such as oxides and polymers, the topology of the structure is defined in terms of the connectivity of bonded atoms, and many physical and chemical properties are determined by the topological short range order. In metallic glasses, due to the metallic character of the atomic bonding, this definition is ill-defined. However, since the first nearest neighbour is reasonably defined by the first peak in the atomic pair distribution function, it is still possible to define TSRO in terms of the topology of Voronoi polyhedra (Finney, 1983), which are equivalent to the Wigner-Seitz cells in crystal structures. Since the distribution in nearest neighbour distances is significant, a more detailed account of the packing around atoms becomes necessary. A method of describing the local structure in terms of a set of local parameters was proposed by Egami *et al* (1980). One of the parameters include the atomic level stresses defined by

$$\sigma_i^{\alpha\beta} = \frac{1}{2\Omega_i} \sum_j f_{ij}^{\alpha} r_{ij}^{\beta}, \tag{2.4}$$

where $\alpha\beta$ denotes Cartesian components, Ω_i is the local volume of the ith atom, f_{ij} is the force between the ith and jth atom and r_{ij} is the distance between them. For a

system interacting via a two body central force potential $\Phi(r_{ij})$, Equation 2.4 reduces to

$$\sigma_i^{\alpha\beta} = \frac{1}{2\Omega_i} \sum_j \frac{1}{r_{ij}} \frac{d\Phi}{dr_{ij}} r_{ij}^{\alpha} r_{ij}^{\beta}. \tag{2.5}$$

Since the microscopic average of the local environment is spherically symmetric, Equation 2.5 may be expressed using spherical harmonics (Y_m^l) by

$$\sigma_i^{l,m} = \frac{1}{2\Omega_i} \sum_j r_{ij} \frac{d\Phi}{dr_{ij}} Y_l^m \left(\frac{\vec{r_{ij}}}{r_{ij}} \right). \tag{2.6}$$

In particular, the rotational invariants of Equation 2.5 are given by

$$P_s = \frac{\sqrt{4\pi}}{3} \sigma_i^{0,0} = \frac{1}{3}(\sigma^{XX} + \sigma_i^{YY} + \sigma_i^{ZZ}), \tag{2.7}$$

which is called the hydrostatic stress, and by

$$\begin{aligned} \tau_s &= \sqrt{\frac{4\pi}{15}} \left[\sum_m (\sigma^{2,m})^2 \right]^{\frac{1}{2}} \\ &= \left[\frac{1}{6} \left((\sigma^{XX} - \sigma^{YY})^2 + (\sigma^{YY} - \sigma^{ZZ})^2 + (\sigma^{ZZ} + \sigma^{XX})^2 \right) \right]^{\frac{1}{2}}, \end{aligned} \tag{2.8}$$

which represents the shear stress. An example of the distribution of P_s and τ_s, calculated for a model of amorphous iron (after Srolovitz *et al*, 1981), is shown in Figures 2.2 and 2.3, respectively.

The hydrostatic stress P_s is closely related to the local volume Ω_i, so that it describes fluctuations in the local density (Egami *et al*, 1980), and the shear stress τ_s describes the local distortion of the atomic environment from spherical symmetry. A detailed study by Srolovitz *et al* (1981) and Egami and Srolovitz (1982) show that the hydrostatic stress P_s is linearly related to the local coordination number Z_i. Therefore, the local pressure fluctuation is related to topological irregularities, considered, for instance, by Spaepen (1978) and Halperin and Nielson (1978) in the case of two-dimensional systems, and for the three-dimensional case by Kleman and Sadoc (1979). When Z_i is

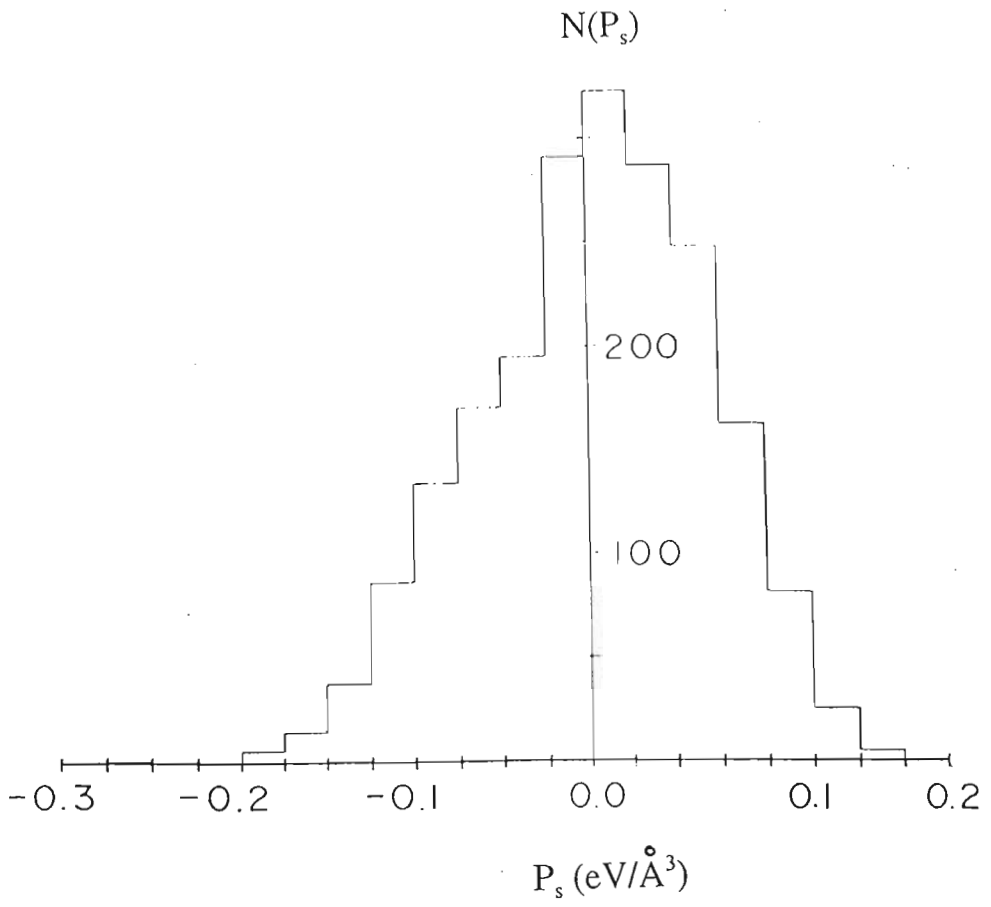

Figure 2.2: Distribution in hydrostatic stress P_s (Srolovitz *et al*, 1981).

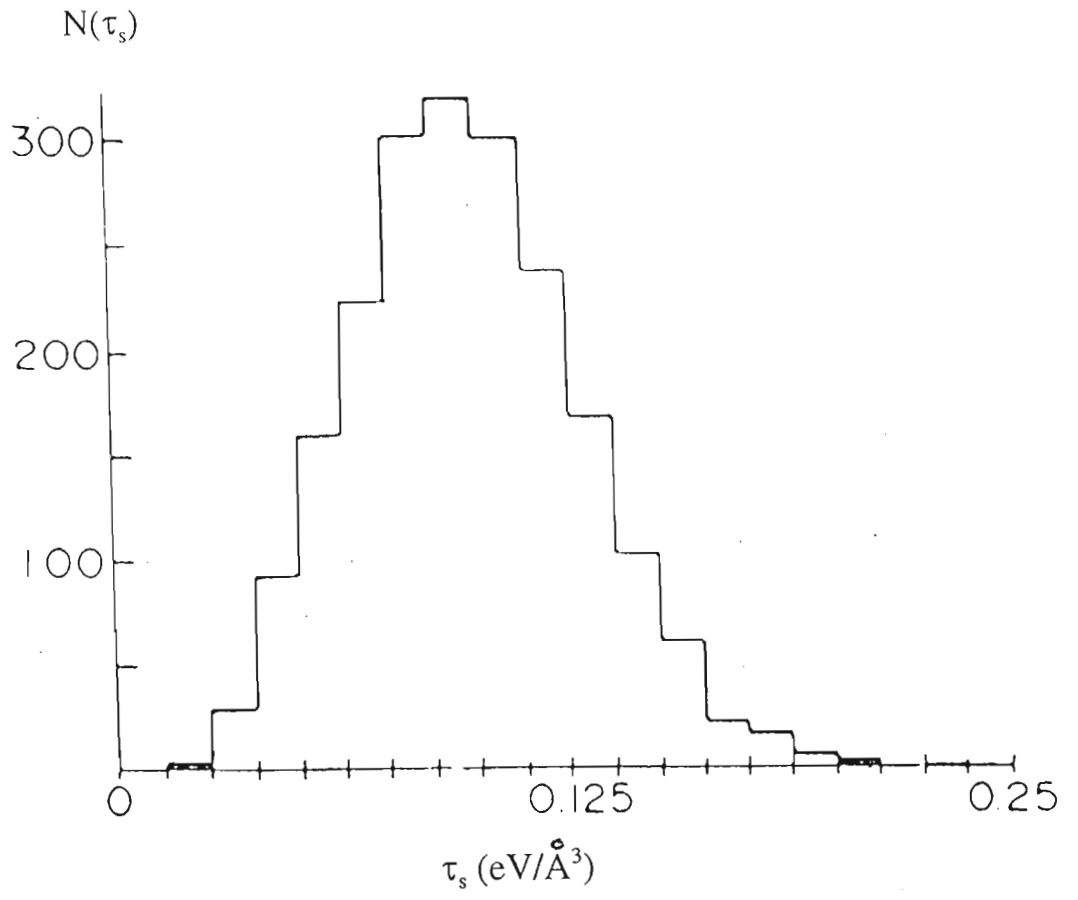

Figure 2.3: Distribution in shear stress τ_s (Srolovitz *et al*, 1981).

small, the atoms in the nearest neighbour shell have a surface tension which results in compression of the central atom and similarly, a large Z_i produces a surface compression and dilational stress of the central atom.

It is appropriate to view the hydrostatic stress as a compressional or dilational stress exerted on an atom fitted to a nearest neighbour shell whose size is smaller or larger than the atom. The shear stress, on the other hand, shows an even weaker correlation with the structural topology. Therefore, while the hydrostatic pressure is related to TSRO, the shear stress describes a different kind of short range ordering called distortional short range ordering (DSRO). Egami *et al* (1981) further categorize the hydrostatic pressure P_s according to compressional stresses p_s or dilational stresses n_s. The n_s type defects then correspond to regions of excess free volume (vacancies), whereas p_s type defects resemble regions of diminished free volume ('self interstitials'). The annihilation of excess free volume is then considered to occur via p_s-n_s recombination.

2.2.4 Kinetics of Processes Distributed in Activation Energy

The kinetics of processes distributed in activation energy, for isothermal annealing, may be described by a differential equation of the kind (Primak, 1955)

$$-(\frac{dq}{dt}) = kq^n, \tag{2.9}$$

where q is the concentration of some kind of defects undergoing kinetic processes, t is time, k is a rate constant and n is the order of the reaction. In practice q cannot be measured directly but only indirectly through a property or property change p which is proportional to the concentration of processes which can yet occur, i.e. $p = Iq$. Then, for processes which are activated at a particular value of activation energy,

$$-(\frac{dp}{dt}) = kI(p/I)^n, \tag{2.10}$$

where I is a constant called the importance factor. The rate constant k is usually assumed to follow an Arrhenius behaviour $A\exp(-\epsilon/\tau)$ for the activated energy ϵ, $\tau(=kT)$ and A a constant having dimensions of frequency. Integrating Equation 2.10, for the measured value of the property, one obtains

$$p(t) = p_o\left[1-(1-n)Bt\exp(-\epsilon/\tau)\right]^{1/(1-n)}, \tag{2.11}$$

where p_o is the value of p at $t=0$ and $B = A(I/p_o)^{1-n}$. This equation also holds when the processes are distributed in activation energy, but now p and p_o are distribution functions of ϵ with dimensions [unit of the property being observed/eV], which cannot be measured directly. Only ΔP, the change in a property P, can be measured and is found by integrating over all activation energies. Thus

$$\Delta P(t) = \int_0^\infty p_0(\epsilon)\theta_n(\epsilon,t)d\epsilon, \tag{2.12}$$

where $\theta_n = \left[1-(1-n)Bt\exp(-\epsilon/\tau)\right]^{1/(1-n)}$ is termed the characteristic isothermal annealing function and is shown schematically in Figure 2.4. θ_n is for most of the range of ϵ nearly zero (at small values of ϵ) or nearly one (at large values of ϵ) and varies from zero to one over only a small range of ϵ (several times τ).

If the initial activation energy spectrum $p_o(\epsilon)$ is very broad, then the annealing behaviour is dominated by the exponential dependence of ϵ appearing in θ_n. The point of inflection appearing in θ_n, designated by ϵ_o, is termed the characteristic activation energy and is defined by

$$\epsilon_o = \tau\ln(Bt). \tag{2.13}$$

During active thermal annealing all processes possessing activation energies $\epsilon \leq \epsilon_o$ will be activated. The rate of property change with annealing is then given by

$$\begin{aligned} -\frac{d\Delta P}{dt} &= -\frac{d}{dt}\int_o^\infty p d\epsilon \\ &= \int_o^\infty p_o\left(-\frac{d\theta_n}{dt}\right)d\epsilon. \end{aligned}$$

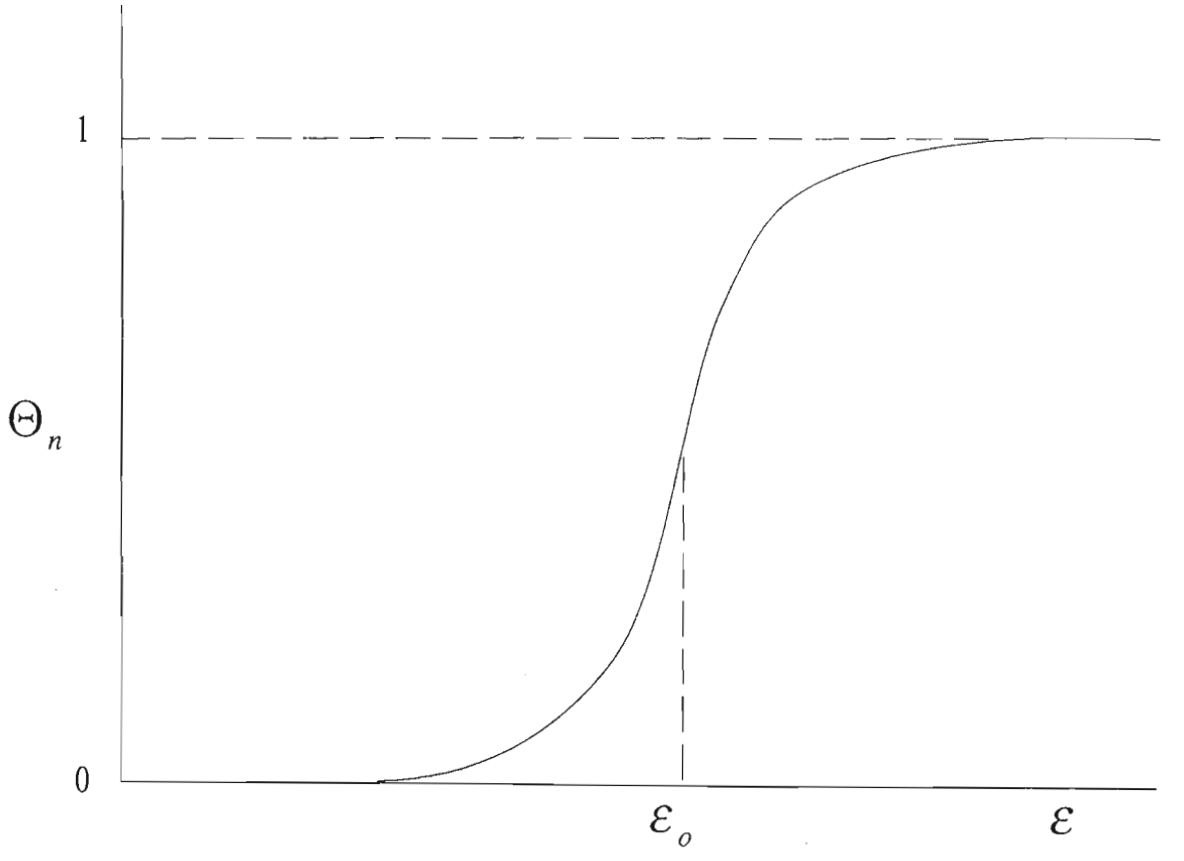

Figure 2.4: The characteristic annealing function θ_n vs ϵ.

Now

$$\frac{d\theta_n}{dt} = -B\exp(-\epsilon/\tau)\left[1-(1-n)Bt\exp(-\epsilon/\tau)\right]^{n/(1-n)}$$

and

$$\begin{aligned}\frac{d\theta_n}{d\epsilon} &= \frac{1}{\tau}B\exp(-\epsilon/\tau)\left[1-(1-n)Bt\exp(-\epsilon/\tau)\right]^{n/(1-n)} \\ &= -\frac{t}{\tau}\frac{d\theta_n}{dt},\end{aligned}$$

so that $d\theta_n/dt$ and $d\theta_n/d\epsilon$ are proportional to each other and therefore possess maxima at the same value of ϵ. The maximum in $d\theta_n/d\epsilon$ occurs at the characteristic activation energy ϵ_o, and hence processes that are activated at the characteristic activation energy make the maximum contribution compared to other processes occurring simultaneously. Furthermore, from the value and slope of the characteristic annealing function θ_n evaluated at the characteristic activation energy ϵ_o, we have

$$\theta_n(\epsilon_o) = n^{1/(1-n)}$$

and

$$\frac{d\theta_n}{d\epsilon}(\epsilon_o) = \frac{n^{n/(1-n)}}{\tau}.$$

It is apparent that most processes occurring simultaneously lie in a narrow band of activation energies of magnitude several times $n\tau$.

As time proceeds, the initial activation energy spectrum is swept out as the characteristic annealing function advances in activation energy as shown in Figure 2.5. Now, for an activation energy spectrum which is wide relative to τ, θ_n may be approximated by a step function, with the step located at ϵ_o. We consider, without loss of generality, the case $n = 1$. Equation 2.12 can now be written as

$$\Delta P(t) = \int_{\epsilon_o}^{\infty} p_o(\epsilon)d\epsilon. \tag{2.14}$$

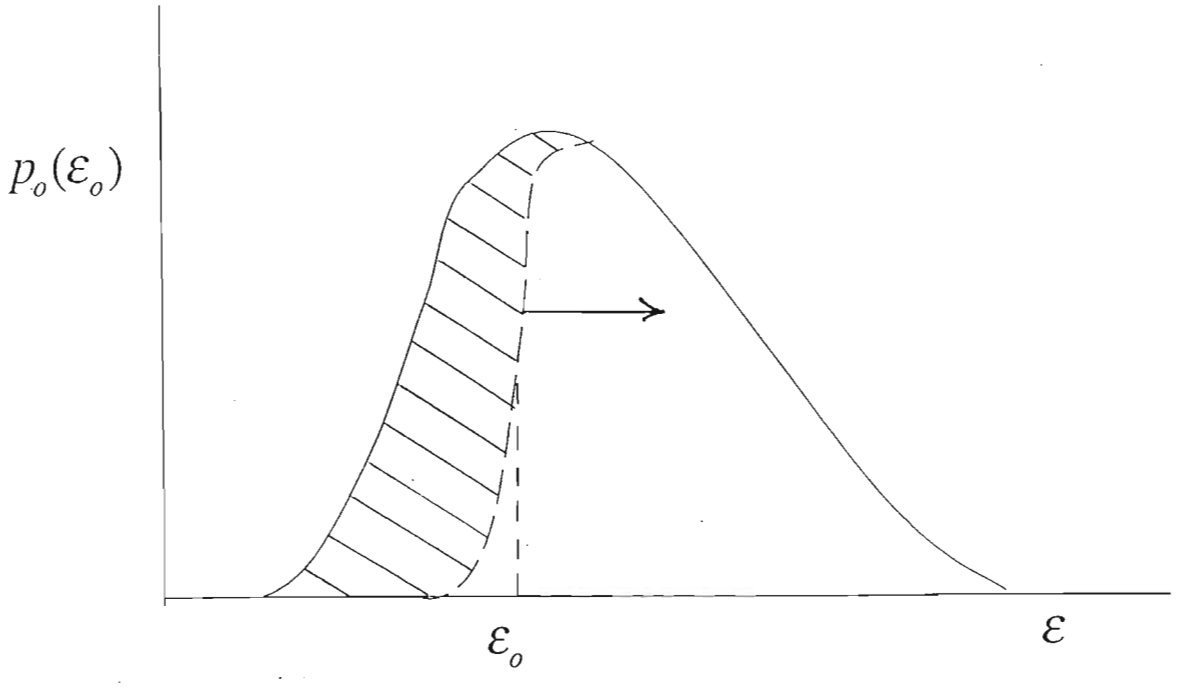

Figure 2.5: A schematic representation of the initial activation energy spectrum $p_o(\epsilon_o)$ being swept out as the characteristic annealing function θ_n advances in activation energy.

The rate of change in ΔP with annealing is now

$$\frac{d\Delta P(t)}{dt} = -p_o(\epsilon_o)\frac{d\epsilon_o}{dt}, \tag{2.15}$$

and, using Equation 2.13, this becomes

$$p_o(\epsilon_o) = -\frac{t}{\tau}\left(\frac{d\Delta P}{dt}\right). \tag{2.16}$$

It is generally assumed that $p_o(\epsilon_o)$ is constant over the region of activation energies undergoing active annealing. One therefore obtains, from Equation 2.16, an expression for the fractional change in property (Gibbs *et al*, 1983)

$$\frac{\Delta P}{P_o} = -p'_o(\epsilon_o)\tau ln(Bt), \tag{2.17}$$

where B is a constant having dimensions of frequency, P_o is the value of the property being observed at the start of the experiment and $p'_o(\epsilon_o) = p_o(\epsilon_o)/P_o$. Note that, since $p'_o(\epsilon_o)$ and $p_o(\epsilon_o)$ are linearly related, we will in future references to Equation 2.17 refer to $p'_o(\epsilon_o)$ as $p_o(\epsilon_o)$, where now $p_o(\epsilon_o)$ has dimensions [eV^{-1}].

Now, for processes activated during thermal annealing, $\ln(t)$ kinetics will be observed provided that $p_o(\epsilon_o)$ is reasonably constant. Although the model does provide a qualitative explanation of the $\ln(t)$ law observed, for example, in the relaxation of the Curie temperature and Young's modulus, it has no predictive power as to the quantitative changes in the various relaxing properties. This will be shown to be attributed to complications in the frequency factor.

From Equation 2.17 it can be seen that the effect of the frequency factor B is to cause a 'simple' displacement along the activation energy axis. An estimation of $p_o(\epsilon_o)$ from Equation 2.17 will reveal the correct approximate shape for the activation energy spectrum but does not correctly fix its location on the activation energy axis (Primak, 1955). For the range of annealing times ($0 < t \leq 2000$ s) chosen here, the activation

energy spectrum revealed, for a particular temperature, is several tenths of an electron-volt compared to the several electron-volt wide initial activation energy spectrum. The whole spectrum can, however, be revealed by isothermal annealing at several different temperatures, but there will be no correlation between parts of the spectrum revealed at different temperatures if the frequency factor is incorrectly chosen. The frequency factor B is usually chosen to be given by the Debye frequency, $\nu = 10^{13}$ Hz. However, no definite value has been proposed. Results obtained by Chen (1981a), from calorimetric measurements in $Fe_{40}Ni_{40}P_{14}B_6$, yielded values for the effective frequency factor ν ranging from 10^{12} s^{-1} at 550 K to 10^{20} s^{-1} at 600 K. Berry and Pritchet (1976), working on internal friction measurements in $Fe_{40}Ni_{40}P_{14}B_6$, obtained a value of 10^{25} s^{-1} for ν at 600 K. Balanzat (1980) obtained a value of approximately 10^{14} s^{-1} for ν at 520 K, from resistivity recovery measurements in $Fe_{40}Ni_{40}P_{14}B_6$. At T_g, ν rises to 10^{46} s^{-1} (Berry and Pritchet, 1976), which is considered to have no intrinsic physical meaning, and in any event the alloy would crystallize above T_g. The calculated values for ν in the isoconfigurational state are apparently much higher than the Debye frequency. This may indicate that either a first order reaction or that Primak's model is inadequate.

We have extended the Primak's model in order to account for the temperature dependence of B, as suggested by Doyle (unpublished). This treatment, presented in Section 2.4, yields a 'relaxation scaling equation' for structural relaxation. The results of structural relaxation measurements are reviewed and compared with respect to this 'relaxation equation'.

2.3 A Review of Relaxation Phenomena

Egami and Srolovitz (1982) predict expressions, in terms of the average hydrostatic stress P_s and shear stress τ_s, for equilibrium TSRO, namely

$$< P_s^2 >= (B_s/k^\alpha \Omega)\tau \quad (T < T_g), \tag{2.18}$$

$$< \tau_s^2 >= (2G_s/k^\gamma \Omega)\tau \quad (T > T_g), \tag{2.19}$$

where B_s is the bulk modulus, G_s is the shear modulus, and k^α and k^γ are constants of the order of unity. Although Equations 2.18 and 2.19 extrapolate to zero at 0 K, $< P_s^2 >$ and $< \tau_s^2 >$ freeze at non-zero temperatures, which define the glass temperature T_g. This can also be inferred from the temperature dependence plot of both $< P_s^2 >$ and $< \tau_s^2 >$ for an amorphous iron shown in Figure 2.6 (Egami and Srolovitz, 1982). For a model amorphous iron system they are $T_g = 760$ K and $T_g' = 2120$ K, which correspond to the freezing in of the pressure P_s and shear τ_s fluctuations, respectively.

The effects of annealing are varied and complex, and some are irreversible while others are reversible below T_g. The irreversible structural relaxation is best shown by the linear increase in viscosity with time (Taub and Spaepen, 1980) and changes in the RDF observed by X-ray diffraction (Egami, 1978). Srolovitz *et al* (1981) find that the changes in the RDF are satisfactorily explained in terms of the change in $< P_s^2 >$ alone. Therefore, it is concluded that irreversible structural relaxation results largely from the reduction in $< P_s^2 >$. This conclusion can be inferred from Figure 2.6. Note that $< \tau_s^2 >$ freezes at a higher temperature than $< P_s^2 >$, where the atomic relaxation time is of the order of 10^{-11} to 10^{-12} s. $< \tau_s^2 >$ can, therefore, relax to its minimum value during rapid quenching at a rate of approximately 10^5 to 10^6 K/s (Egami, 1983). On the other hand, $< P_s^2 >$ can be frozen at a value larger than its equilibrium value. This value is characterized by the so called fictive temperature T_f at which the frozen value of $< P_s^2 >$ is in equilibrium. Subsequent annealing relaxes $< P_s^2 >$ towards its low

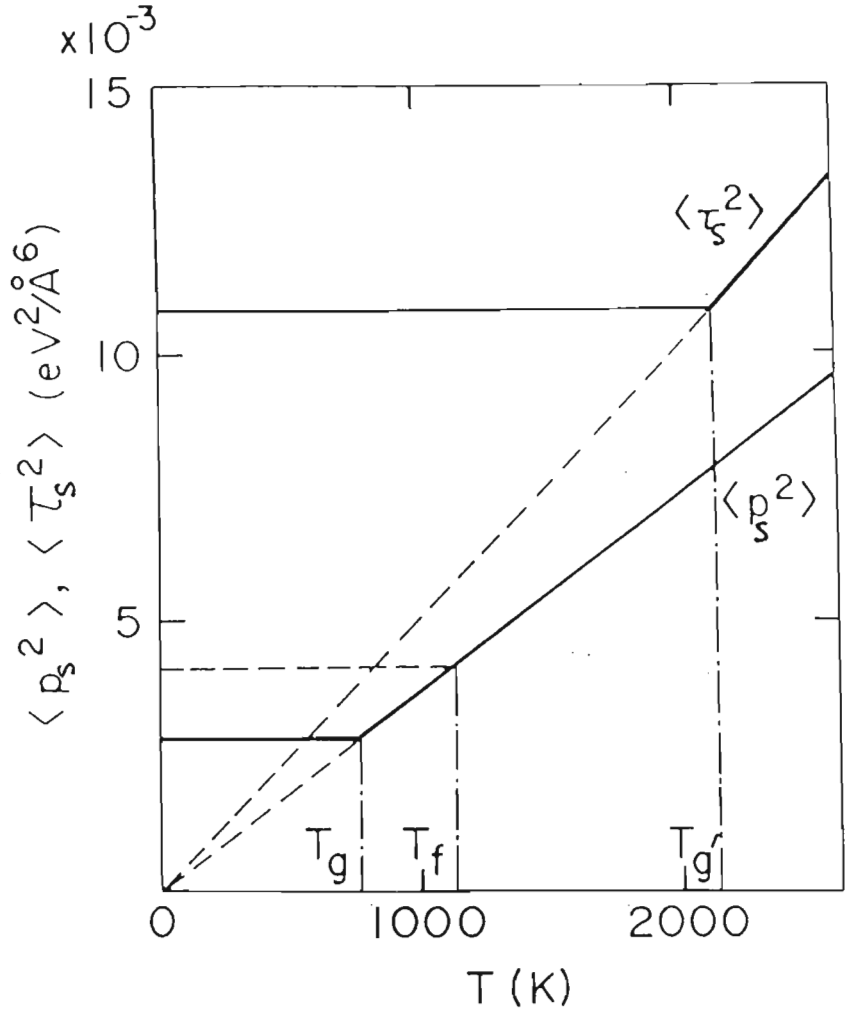

Figure 2.6: Temperature dependence of $< P_s^2 >$ and $< \tau_s^2 >$ calculated for a model amorphous Iron. T_g is the glass temperature, T_f the fictive temperature and T_g' the upper glass transition temperature (Egami and Srolovitz, 1982).

temperature value, while $< \tau_s^2 >$ does not change any further. The change in $< P_s^2 >$ is due to recombination of compressional p_s and dilational n_s stresses leading to a reduction in the excess free volume. Since the change in $< P_s^2 >$ is proportional to the change in free volume, the change in $< P_s^2 >$ should also affect the viscosity and diffusivity. Egami *et al* (1980) use the free volume theory to relate diffusivity to $< P_s^2 >$, thus

$$D \sim \exp\left(\frac{-c}{(< P_s^2 > - < P_s^2 >_{eq})}\right), \tag{2.20}$$

where $< P_s^2 >_{eq}$ is the equilibrium value of $< P_s^2 >$ and c is a constant.

Van den Beukel and Radelaar (1983) propose a model to describe the changes in TSRO during structural relaxation of metallic glasses. The temperature dependence of the viscosity of metallic glasses is generally described by the so-called Vogel-Tammann-Fulcher equation (see Section 1.2)

$$\eta = \eta_o \exp(B/(T - T_o)), \tag{2.21}$$

where B is a constant and T_o is an ideal glass temperature. This expression is theoretically justified by the free volume theory for liquids (Cohen and Turnbull, 1959), which yields for the viscosity

$$\eta = \eta_o \exp(\gamma V^*/V_f), \tag{2.22}$$

where V_f is the free volume per unit volume, γ is a constant of the order of 1 and V^* is the atomic volume per unit volume. Comparing Equations 2.21 and 2.22 yields

$$V_f = A(T - T_o) \tag{2.23}$$

and

$$B = \frac{\gamma V^*}{A}. \tag{2.24}$$

Equation 2.21 has been fitted to experimental data both for liquid and glassy states, and it is generally found that the fitting constants η_o, B and T_o differ markedly for the liquid and glassy state of the same material (Van den Beukel and Radelaar, 1983).

Taub and Spaepen (1980) reporting on viscosity measurements in $Pd_{80}Si_{20}$ find η to be temperature dependent according to $\eta \sim exp(Q_n/kT)$, where Q_n is an activation energy of 1.99 eV. Although in conflict with Equations 2.21 and 2.22, this form for η is in agreement with a solid like model of diffusion in metallic glasses developed by Spaepen (1977), which gives

$$\begin{aligned} \eta &= \eta_o \exp(Q_n/kT)\exp(\gamma V^*/V_f) \\ &= \eta_o \exp(Q_n/kT)\exp(B/(T-T_o)). \end{aligned} \tag{2.25}$$

Van den Buekel and Radelaar (1983), using Equation 2.25 as a starting point, describe the annealing rate of free volume (TSRO) as a function of annealing time and temperature, namely by

$$\frac{d\eta}{dt} = -\eta_o \exp(Q_n/kT)\frac{\gamma V^*}{V_f^2}\exp(\gamma V^*/V_f)\frac{dV_f}{dt}. \tag{2.26}$$

Taub and Spaepen (1980) observed $d\eta/dt$ to be constant and proportional to $\exp(-Q'/kT)$, with Q'=0.33 eV in $Pd_{80}Si_{20}$ alloys, during isothermal annealing. From Equation 2.26 it then follows that

$$\frac{dV_f}{dt} = c\frac{V_f^2}{\gamma V^*}\exp(-Q_a/kT)\exp(-\gamma V^*/V_f), \tag{2.27}$$

where c is a constant and $Q_a = Q_n - Q'$ is the activation energy required for the annihilation of free volume. In PdSi, $Q_a = (1.99-0.33)$ eV $= 1.66$ eV (Taub and Spaepen, 1980). Equation 2.27 is found to satisfactorily describe the annealing out of V_f at temperatures below T_g.

For isothermal annealing at temperatures below T_g, integration of Equation 2.27 yields

$$\exp(\gamma V^*/V_f) - \exp(\gamma V^*/V_{fo}) = ct\exp(-Q_a/kT) = c'(T)t, \tag{2.28}$$

where $c'(T) = c\exp(-Q_a/kT)$ and V_{fo} is the initial free volume per unit volume. As an example, Figure 2.7 shows a plot of V_f as a function of $\log(c't)$ for $\gamma V^* = 0.1$ and three

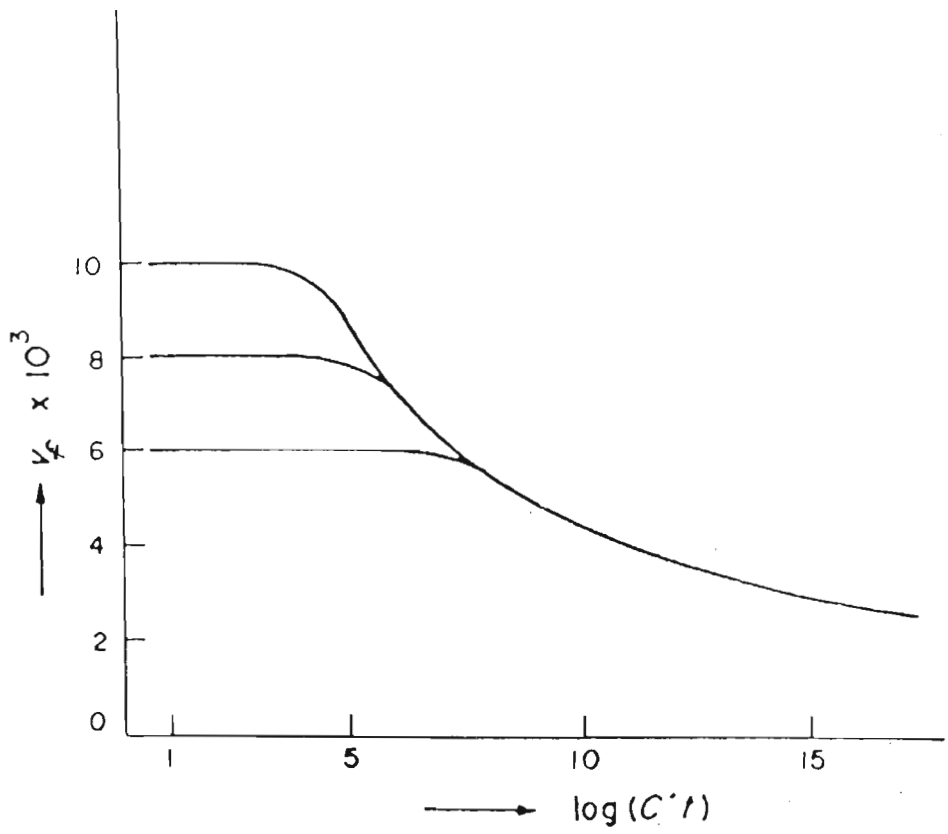

Figure 2.7: V_f versus $\log(c't)$ for three initial values of V_{fo} (Van den Beukel and Radelaar, 1983).

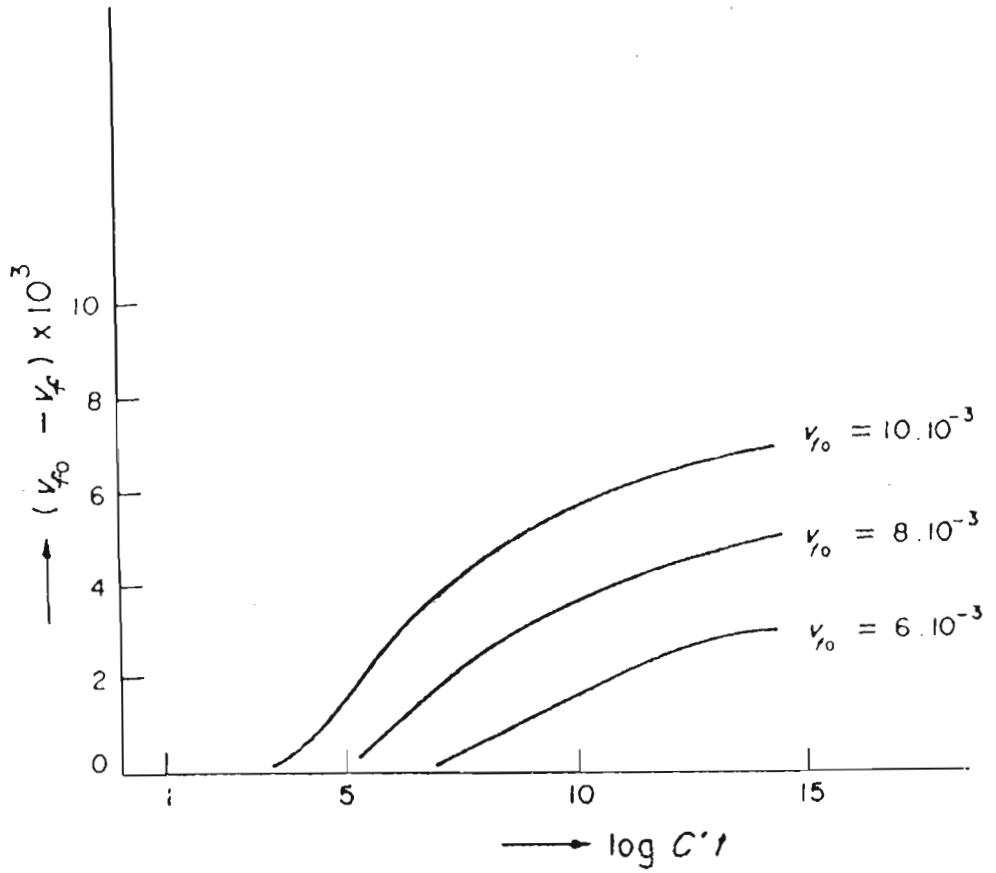

Figure 2.8: $\Delta V_f = V_{fo} - V_f$ versus $\log(c't)$ for three initial values of V_{fo} (Van den Beukel and Radelaar, 1983).

different values of V_{fo}, and Figure 2.8 shows a plot of $\Delta V_f = V_{fo} - V_f$ against $\log(c't)$. Some structure sensitive properties, such as length or Young's modulus, are expected to change in proportion to ΔV_f during structural relaxation. Girt *et al* (1980), and Scott and Kursomovic (1982) reporting on isothermal changes of these properties show a shape in qualitative agreement with the curves of Figure 2.8. The activation energy Q_a can be determined from isothermal measurements at different temperatures. When different combinations of time t_i and temperature T_i yield the same V_f, a plot of $\log(t_i)$ versus T_i yields Q_a.

Irreversible structural relaxation related to TSRO can change the local CSRO of an alloy. It is recognized that the CSRO defined by the Warren-Cowley parameter α_p, in Equation 2.2, can be altered only when the local pressure P_s is changed. When the local topology is altered, the value of α_p is changed by atoms involved directly in the topological change, namely forming or breaking of bonds. Since the mechanism which changes the CSRO is not unique, the kinetics of CSRO should reflect these mechanisms. For example, a small part of the change in Curie Temperature T_c appears to be irreversible, and may be a consequence of irreversible structural relaxation involving TSRO. A significant part of the change in T_c, however, is reversible. There is evidence that the kinetics of changes in T_c are dependent upon the thermal history (Chambron and Chamberod, 1980). This dependence, however, is relatively weak and distinct from irreversible structural relaxation.

In multicomponent metallic glass alloys, like $(FeNi)_{80}(BP)_{20}$, relaxation processes are often ascribed to some kind of chemical/compositional short-range ordering (or clustering) of atoms (Drijver *et al*, 1981). The ordering is limited to two kinds of atoms A and B, and the equilibrium short-range order can be described by the Warren-Cowley parameter α_p. For simplicity the high-temperature approximation for α_p is used, namely

$$\alpha_p = 2\frac{C_A C_B W}{kT}, \tag{2.29}$$

where $W = V_{AB} - \frac{1}{2}(V_{AA} + V_{BB})$ is the ordering energy and V_{ij} is the interaction potential between atoms i and j. An estimate for the ordering energy W can be deduced from calorimetric measurements. When the CSRO is in equilibrium and the temperature is raised substantially from T_1 to T_2, then according to Equation 2.29, α_p changes by

$$\Delta\alpha_p = \frac{2C_A C_B W}{k}\left(\frac{1}{T_2} - \frac{1}{T_1}\right). \tag{2.30}$$

It can be shown (Van den Beukel and Radelaar, 1983) that this corresponds to an absorbed enthalpy of

$$\Delta H = -C_A C_B Z W \Delta\alpha_p, \tag{2.31}$$

where Z is the coordination number. From measurements on an Fe-B based glass (Majewska *et al*, 1981) values for W range between 1 and 2 kJ/mol.

Calorimetric scans are generally taken after pre-annealing the samples for a time t_a at a temperature T_a. Figure 2.9 (after Van den Beukel and Radelaar, 1983) shows the results for T_a = 400 K (t_a=10^5 and 10^6 s) and for T_a = 450 K (t_a=10^3, 10^4 and 10^5 s). The shortest annealing times (10^5 and 10^3 s respectively) were chosen so that equilibrium at the subsequent annealing temperatures were only just attained. For these annealing times the decrease in free volume is still negligible, whereas for larger times an increasing part of the free volume is annealed out for each annealing temperature. The magnitude of the endothermic peak increases with increasing t_a. This is due to the fact that the excess free volume continues to anneal out after equilibrium CSRO has been attained. This irreversible relaxation is thought to involve recombination of p_s-n_s defect pairs. If defects are trapped in local potential wells, they can move reversibly without mutual annihilation. Relaxation processes, therefore, involve either conservative or non-conservative rearrangement of these defects. The former rearrangement obviously allows for reversible and the latter for irreversible relaxation phenomena.

Boesch *et al* (1970) studied the crossover effect in a B_2O_3 glass, and Greer and Leake (1979) extended this work to $Fe_{80}B_{20}$ metallic glass. The data was fitted using a

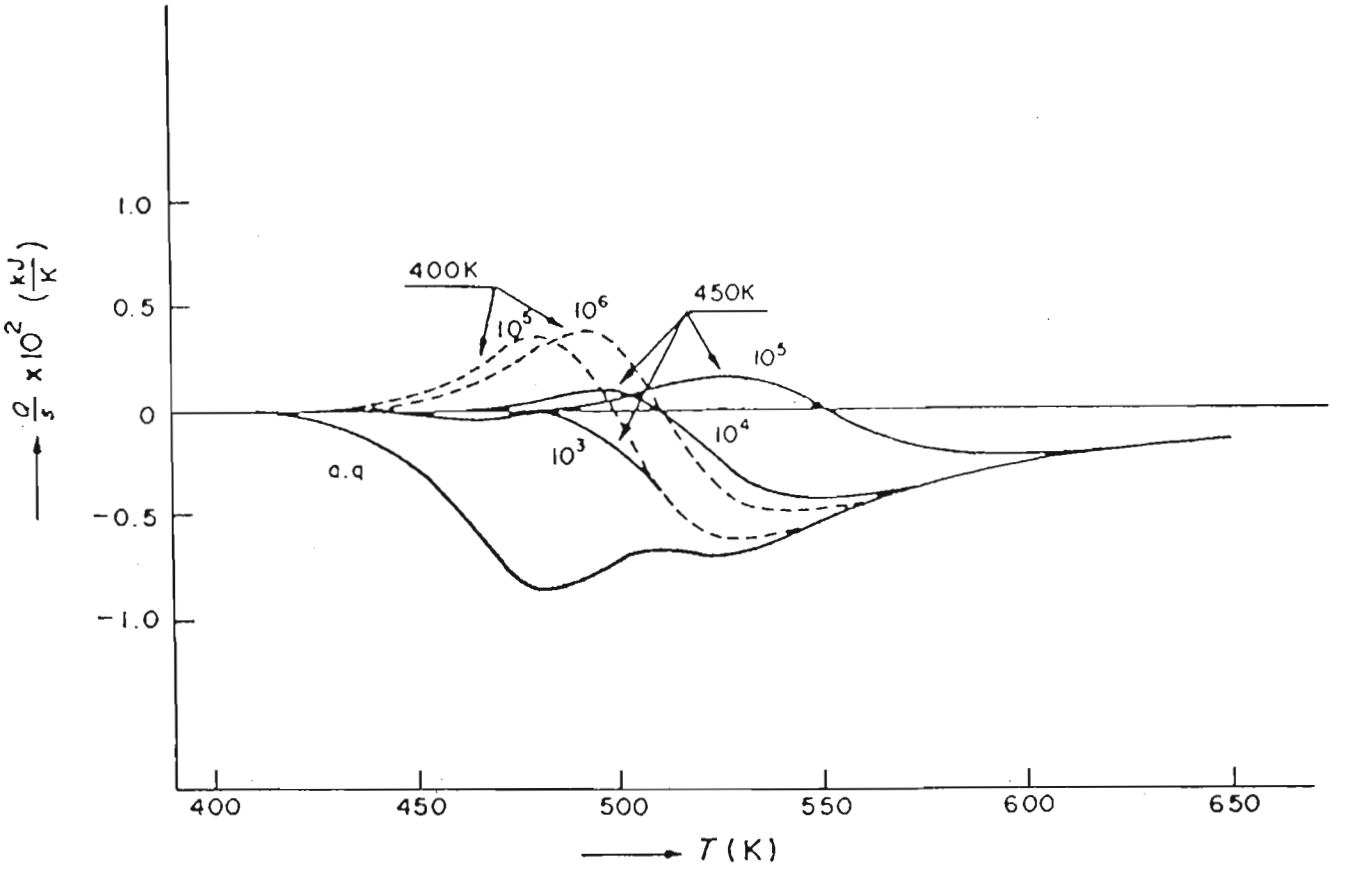

Figure 2.9: Evolution of heat during continuous heating of an as-quenched glass and of glasses pre-annealed at 400 and 450 K during the times indicated (Van den Beukel and Radelaar, 1983).

two relaxation time empirical model of the form

$$P(t) = A_o \pm \left[A_1 \exp(\frac{-t}{\tau_{r1}}) \pm A_2 \exp(\frac{-t}{\tau_{r2}})\right],$$

where $P(t)$ is the measured property, A_0, A_1 and A_2 are constants, and τ_{r1} and τ_{r2} are characteristic relaxation times. Using a similar approach, Cost and Stanley (1984) studied the fine structure of the spectrum of relaxation times from the changes in electrical resistance during sub-T_g annealing procedures, using the direct spectrum analysis (DSA) method. This method obtains an approximation of the relaxation time spectrum by an analysis of the total relaxation response curve. Results on a FeNiPB amorphous alloy reveal a multi-modal spectrum, for a relaxation response curve, with four relatively narrow well separated peaks of varying height, as shown in Figure 2.10. Although the significance of the fine structure is difficult to understand without extensive investigation, the authors attribute it to the microstructure of the metallic glass. They predict that there may be four different kinds of regions or domains in the glass, each of which has a different structure, in which the atomic rearrangements for the ordering process take place at different rates. Although a reasonable fit with experimental results is obtained, there is a conceptual difficulty in relating a spectrum of relaxation times with physical properties of the system.

Chen (1981a) investigated relaxation processes in $Fe_{40}Ni_{40}P_{14}B_6$ below the glass transition temperature. Apparent specific heats of the glass were measured calorimetrically, following isothermal annealing treatments, over a range of super-ambient temperatures. The results show endothermic peaks followed by a broad exothermic reaction at higher temperatures up to T_g. The latter reaction is accepted as corresponding to structural relaxation towards a more stable glassy state. The endothermic peaks imply stabilization of a portion of the relaxation spectrum, which upon further heating destabilizes. The results also show that the increase in specific heat ΔC_p and the temperature at the endothermic peak varies linearly with annealing time. The change in ΔC_p can

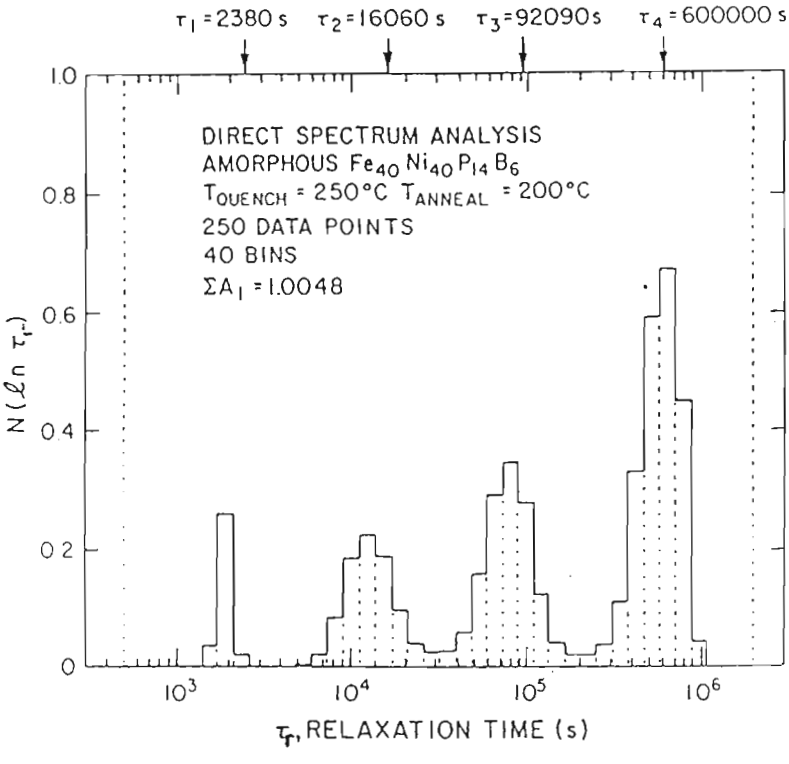

Figure 2.10: Histogram of the relaxation time spectrum for FeNiPB (Cost and Stanley, 1984).

be associated with a varying activation energy E_o, which varies from 1.5 to 2.8 eV in the range $500 < T < 660$ K (Chen, 1981a). Comparing this with the activation energy Q_n for viscous flow, Chen (1980) found that E_o approaches Q_n at the glass transition temperature T_g involving a rapid increase in E_o from 2.9 eV at 660 K to 6.7 eV at 705 K. This behaviour is indicative of cooperative movement of a group of atoms close to T_g.

Chen and Inoue (1984) have carried out investigations on enthalpy relaxation in PdNiSi glasses. The specimen geometry included both ribbon and wires, and each were subjected to a variety of heat treatments. They conclude that the classification of relaxation processes into two types, namely CSRO and TSRO, is an oversimplification and suggest that recoverable relaxation is due to short range localized relaxation and irrecoverable structural relaxation results from annihilation of defects. They also note that the endothermic peaks are lower in the binary PdSi alloy than in the ternary PdNiSi alloy. The magnitude of the peak for the specific heat was also seen to decrease as the Si content of both samples increased from 16.5 to 22.0 atomic %. They suggest that mixing two metal elements (Pd and Ni in this case) disturbs the short range order whereas, addition of metalloid atoms (Si) enhances the structural and compositional ordering. Therefore, the magnitude of the specific heat peak is correlated to the degree of structural disorder.

To recapitulate, the relaxation processes causing the endothermic peak are reversible, while the processes leading to the exothermic reaction are irreversible. The reversible relaxation is believed to arise from short-range localized structural relaxation in the stabilised portion of a more-or-less rigid matrix. The irreversible relaxation is due to structural stabilization resulting from the annihilation of defects leading to a reduction of free volume. The annihilation of defects may be termed medium-range cooperative structural relaxation involving only local regions of the glassy material. The stabilized local regions arising from annihilation of defects expand over the whole system and the relaxation processes become long range cooperative structural relaxation,

commonly observed for sub-T_g annealing.

Chen (1983) studied the change in Curie Temperature T_c of a $Fe_{40}Ni_{40}P_{14}B_6$ glass subjected to cyclic ageing between 473 K and 532 K for successive annealing periods of $t_a = 30$ min. Figure 2.11 shows the results together with the corresponding endothermic specific heat ΔC_p after each anneal. The main features of these results are:

1. Each increase in temperature (to 523 K) eliminates or reduces the structural relaxation incurred during the previous low temperature (473 K) anneal, i.e. the disappearance of the low temperature spectrum '1', and a rapid drop in T_c by about 4 K. It is then followed by a gradual increase in T_c, reminiscent of a memory phenomenon. The effect of the high temperature anneal is represented by the ΔC_p peak '2'.

2. Each decrease in annealing temperature (to 473 K) recreates the low temperature spectrum superimposed on the high temperature one and T_c is raised gradually by about 4K.

3. Each successive annealing at 523 K leads to a gradual development of the ΔC_p spectrum and an increase in T_c but with a slower rate, becoming negligibly small at later stages of cyclic ageing.

Leake *et al* (1984) investigate relaxation in a metallic glass in terms of the activation energy spectrum using isothermal annealing and crossover experiments. They make measurements of Curie temperature T_c in $Fe_{80}Ni_{20}$ alloys and compare the results with theoretical estimates, which are based on a distribution of activation energies. This model assumes a 'fixed' difference between the initial spectrum $Q(E)$ and the equilibrium spectrum $Q_s(E)$ for the chosen annealing temperature. Crossover effects are explained in terms of the activation energy spectrum by considering the movement of an annealing function along the activation energy axis where the annealing function (see Section 2.2.4)

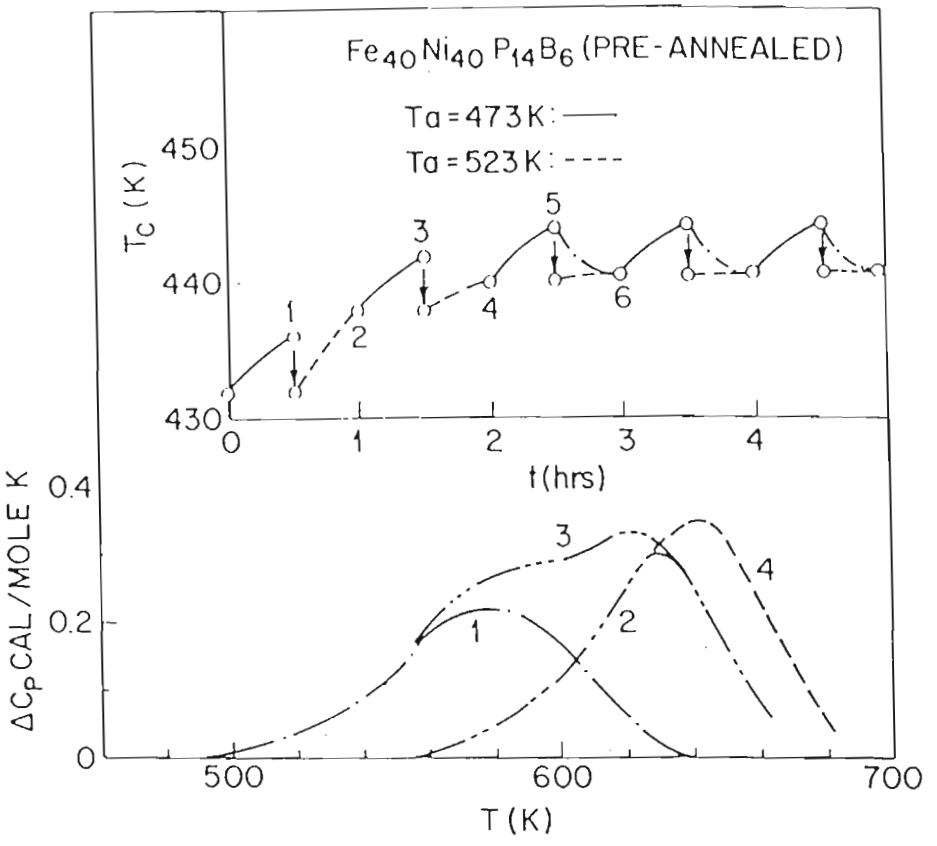

Figure 2.11: Changes in T_c and the corresponding enthalpy evolution of the $Fe_{40}Ni_{40}P_{14}B_6$ glass (Chen, 1983).

is approximated to a step function. As shown by Gibbs *et al* (1983) this model predicts that the minimum change in Curie temperature ΔT_c would occur when the characteristic energy ϵ_o specifying the position of the step is the same at the beginning of the higher temperature anneal as at the end of the lower temperature anneal. The step function now allows the property changes to continue as if the specimen had been annealed only at the new temperature. By plotting the spectra of ΔT_c as a function of ϵ_o, Gibbs and Evetts (1981) earlier showed that the curves do not coincide immediately after the minimum has occurred, but do so after some time indicative of crossover effects.

Tarnoczi (1985) measured the Curie temperature T_c with structural relaxation annealing procedures on a $Fe_{16}Ni_{65}B_{16}$ metallic glass. An as-quenched sample was annealed at 519 K and measurements were taken of the Curie temperature as a function of annealing time. It is assumed that structural relaxation can be described by two functions, with short and long characteristic time variations. The characteristic parameters of the slow process are expected to be obtained by choosing an appropriate function to fit the second part of the curve. A single exponential function, usually suggested as a fit, is found to be inappropriate and it is suggested that, instead of the usually accepted two function relaxation, structural relaxation starting with an as-quenched sample involves three processes. Pre-annealed samples, on the other hand, were shown to fit well to a two exponential function. Tarnoczi suggest that the explanation of these results can be based on the supposition that the third process is a slow process which results from relatively long range diffusion of large defects. Thus, it is concluded that structural relaxation in metallic glasses can be divided into reversible and irreversible components. The irreversible part would appear to be due to the annealing out of macroscopic defects, which originate from inhomogeneous thermal contraction during rapid cooling from the melt. The reversible part of the relaxation involves the attainment of some dynamic equilibrium of defects and is composed of a rapid and a slow process. The rapid process

may be characterized by a lower activation energy and the slower process by a larger activation energy.

Gibbs *et al* (1983) have tested the predictions of an activation energy spectrum model for stress relaxation in amorphous $Fe_{40}Ni_{40}B_{20}$. The model is shown to be of considerable value in understanding relaxation kinetics in metallic glasses. The following predictions of the activation energy spectrum model with regard to $\ln(t)$ kinetics have been shown to hold:

1. $\ln(t)$ behaviour is re-established after a pre-anneal when sufficient time has elapsed for the annealing function to have reached a part of the spectrum unaffected by the pre-anneal.

2. The gradient $\Delta P/\ln(t)$ is constant for a given T in a regime where $\ln(t)$ kinetics is observed.

The conclusion from this work is that $\ln(t)$ kinetics are not fundamental to a metallic glass, but merely arise from the limited range of time and temperature chosen for a particular experiment. If ideal measurements were made from zero time at the final annealing temperature, where all the effects of storage, the original quench and any pre-anneals are included, the curve would be sigmoidal with a central region approximately linear with $\ln(t)$.

Egami (1978) modeled the problem of $\ln(t)$ kinetics by assuming that the relaxation of a property P has an activation energy that is linearly related to the instantaneous magnitude of the measured property. Thus,

$$\frac{dP}{dt} = B\exp\left(\frac{-\alpha P}{kT}\right), \tag{2.32}$$

where B and α are constants. Using the changes found in the second X-ray diffraction peak, Egami (1978) was able to fit this data with a $\ln(t)$ response. By including a

'back flux' of processes as well as a 'forward flux' it is possible to achieve stabilization of a measured property with isothermal annealing for a sufficiently long time (Kuhlman, 1948). There is, however, a difficulty in relating the activation energy, in this way, to the measured property.

The first report involving isothermal kinetics of densification were claimed by Kursumovic *et al* (1980). Figure 2.12 shows the results of changes in length (densification) during isothermal annealing of $Fe_{40}Ni_{40}B_{20}$ alloys. $\ln(t)$ kinetics are indeed approximately observed, but these are superimposed with oscillations that are considered as additional processes to that of the underlying $\ln(t)$ relaxation. The oscillatory behaviour was tentatively attributed to changes in anisotropic short range order. The oscillatory behaviour is now understood to arise from annealing in the presence of oxygen and to the behaviour of the oxide layer on the specimen, which is distinctly different from that of unoxidised samples (Marcus, 1979).

From above, it is apparent that no single model is capable of explaining all three ($\ln t$, reversibility and crossover) relaxation phenomena. Also, no model has a quantitative predictive power nor have they yielded a tractable mathematical formalism. Argon and Kuo (1980) use a more complex analysis based on the work of Primak (1955), which gives a complete treatment for relaxation in systems with a broad activation energy spectrum, and in principle allows for the identification of the order of the relaxation reaction and the determination of the initial activation energy spectrum. This theoretical treatment is fully described in Section 2.2.4 and forms the basis of the current work discussed next.

2.4 Development of a 'Relaxation Equation'

Any model of a metallic-glass structure must show that the glass is metastable with respect to a thermodynamic ground state, and must help to explain the mechanisms

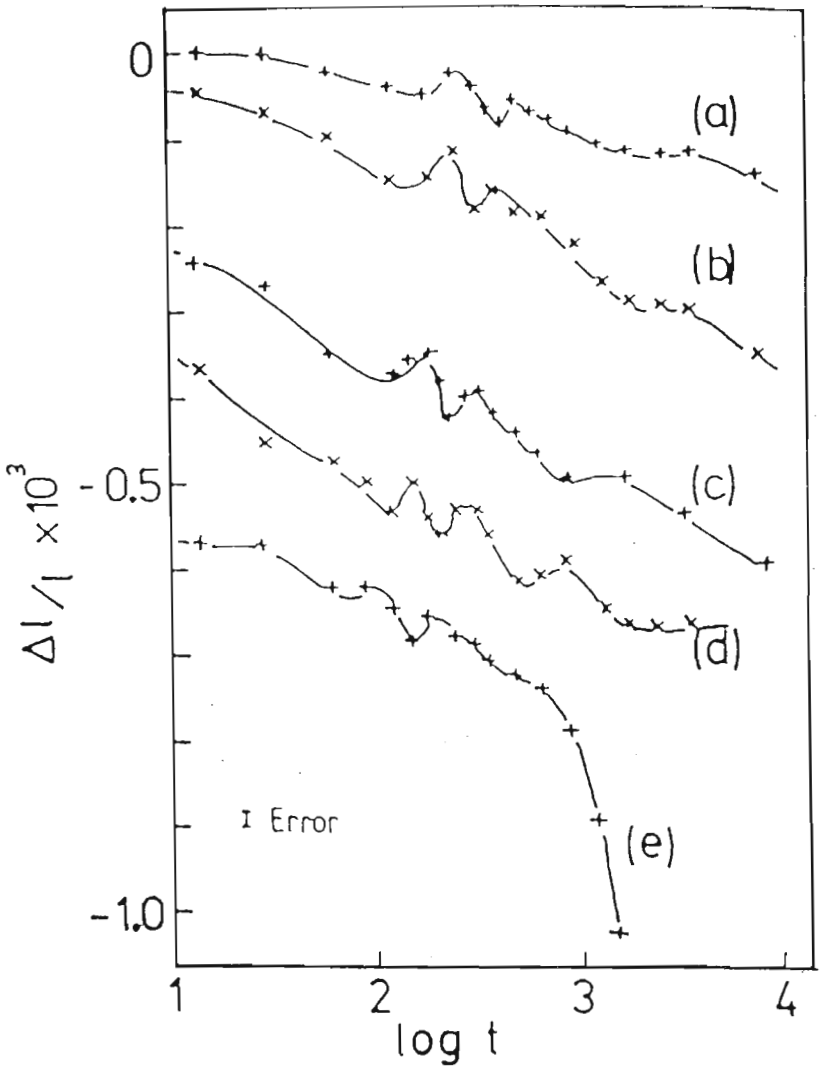

Figure 2.12: Changes in length during short-time annealing of amorphous $Fe_{40}Ni_{40}B_{20}$. The annealing temperatures are (a) 323 K, (b) 573 K, (c) 598 K, (d) 623 K and (e) 673 K (Kursmovic *et al*, 1980).

involved in any relaxation process. One approach to understanding the changes taking place during relaxation is to consider the energies of the various local metastable states. Thus, in order to rearrange a system of atoms into a new and more stable structure the system must first pass through some states of higher energy, for example, states in which the initial atomic bonds have been broken and new ones not yet formed. Consider Figure 2.13, which represents a one dimensional plot of potential energy in configuration space, for a two level system. The movement of the atom from the metastable position X to a more stable position Z is opposed by the energy barrier ϵ_A. In general, tunneling effects play little part in such systems because the mass of the atom is large enough to make the tunneling rate negligible for the types of energy barriers commonly encountered in physico-chemical problems. Thus, until the atom can temporarily acquire the necessary extra energy to carry it over the barrier, it will remain in the metastable position X. The smallest energy ϵ which will allow it to go over is the activation energy ϵ_A of the reaction.

All metastable states have a finite driving force tending to produce transformations to a more stable state. Despite this, amorphous alloy systems are capable of existing indefinitely in metastable forms. Configurations of the basic particles in a metastable system is one for which the Gibbs Free Energy G is a relative minimum but numerically greater than the value associated with a stable configuration. In order to affect an atomic rearrangement, energy must be available. The additional free energy necessary for an atom to surmount this thermodynamic barrier to transformation is supplied by thermal fluctuation, a process termed thermal activation. The free energy change, between the initial and final states, accompanying a thermally activated reaction is not altered, i.e. the acceleration of the reaction rate is accomplished without alteration of the driving force. The reaction velocities will, however, depend very much upon the magnitude of the activation free energy and the random thermal motion.

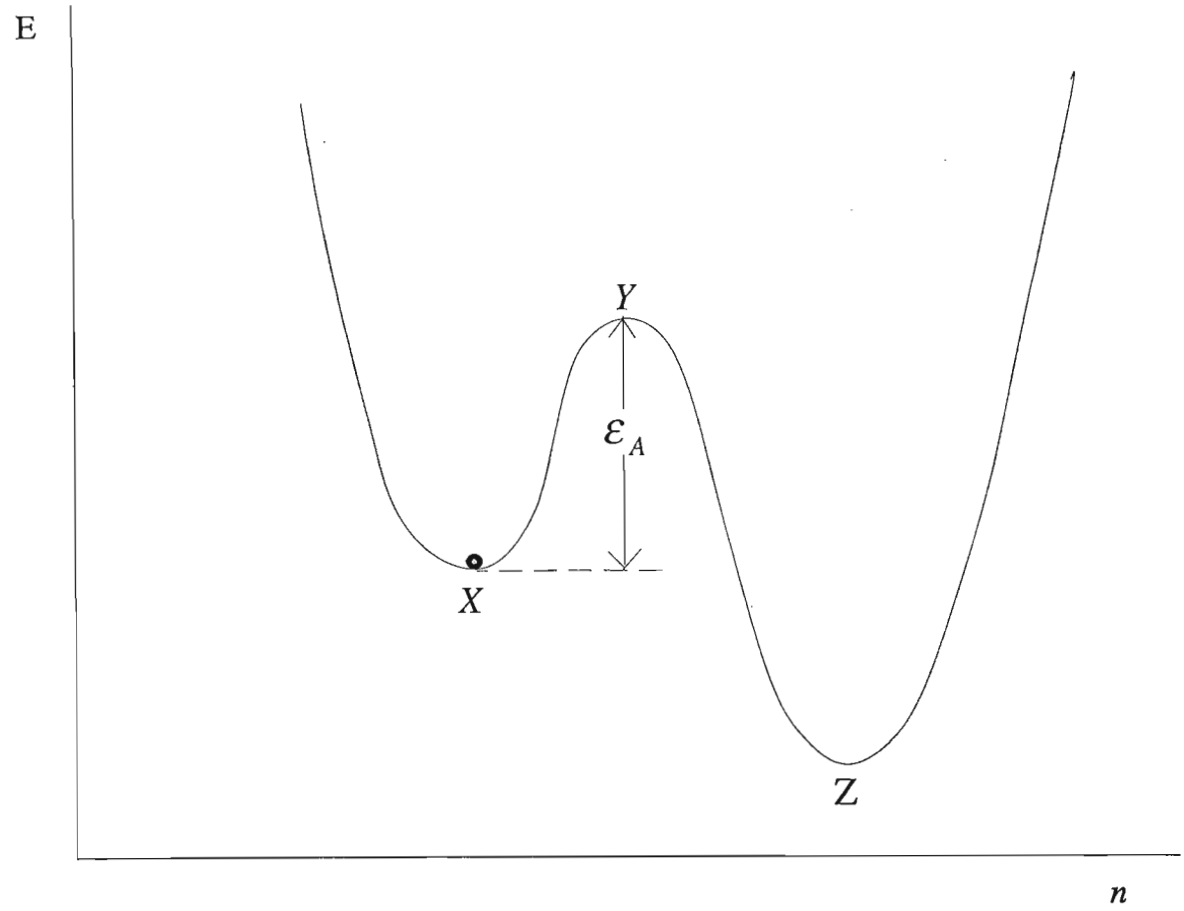

Figure 2.13: Potential energy plot for a two level system.

Geometrically, each spatial lattice site has associated with it a potential energy well of the form depicted. A population of double wells represent a particular structural configuration with atoms either in position X or Z. In a real amorphous structure there exist a spectrum of coupled wells with each atom being able to jump to a number of neighbouring wells with differing energies. The action of an atomic jump changes the energy levels of the neighbouring wells. Gibbs *et al* (1983) discuss several aspects associated with this simplistic model. These may be summarized as follows:

1. As stated above, there exist a population of double wells with different activation energies. In terms of this model there will be different types of processes with different activation energies ϵ. The measured property change will then depend on the type of processes occurring with that value of ϵ.

2. 'Well' systems involving the activated motion of groups of atoms must also be considered. The wells are coupled such that any atom jump changes the nearest neighbour configuration and, therefore, the well structure relative to nearby atoms. It is likely that the various activation barrier heights will be evenly distributed, involving a low activation energy surrounded by processes with relatively high activation energies.

3. An activated process changes the number density distribution of available processes that can yet occur. For example, a low activation energy jump to reduce a large excess free volume can create two or more smaller regions of excess free volume, which represent new processes with higher energies of activation. However, this does not in any way alter the model (Primak, 1955).

Thus, the macroscopic result of a transition is achieved by a large number of repetitions of one or more basic atomic processes. The elementary processes vary from the movement of single atoms, to quite complicated mechanisms involving the cooperative action of

many atoms. The various possible mechanisms are outlined in Section 2.5. Structural relaxation involves a number of different basic microscopic processes each with its own characteristic activation energy ϵ, and in these cases it is not possible to attach any particular significance to the experimental activation energy determined from the slope of an Arrhenius plot. This is indeed the case in the present system under study.

Since the driving force is due to thermal activation, only processes with activation energies $\epsilon > kT$ will be activated. In a metastable state any particular atom spends most of its time near the minimum at X. We consider only those movements of the atom in the direction of the barrier. For small displacements Δx about the minimum at X, the 'potential' energy $\epsilon(x)$ varies as $(\Delta x)^2$. This results in simple harmonic motion since, the restoring force $d\epsilon/dx$ increases linearly with Δx. We thus approximate the actual motion at X by simple harmonic motion with frequency ν at small amplitudes. The particle thus makes ν attempts per second at the barrier. Such an attempt is successful when the particle has energy ϵ_A or more. A property of simple harmonic motion is that the frequency is independent of amplitude. This leads to the quantization of energy levels, spaced at intervals $h\nu$, where h is Planck's constant. If we seek the probability that the particle has energy $\epsilon_A + nh\nu$, where n = 0,1,2,.. etc, then using the classical distribution, we obtain for this probability

$$\begin{aligned} P &= \frac{\sum_{n=0}^{\infty} \exp[-(\epsilon_A + nh\nu)/kT]}{\sum_{n=0}^{\infty} \exp[-nh\nu/kT]} \\ &= \exp(-\epsilon_A/kT). \end{aligned} \tag{2.33}$$

Hence, the frequency f for crossing the barrier is

$$f = \nu \exp(-\epsilon_A/kT). \tag{2.34}$$

This equation applies strictly only when the number of energy states available to the particle is the same at X and Y. If there are w states at Y for every one at X, then the probability of the particles acquiring the activation energy ϵ_A is correspondingly

increased by a factor w. As a measure of disorder we can relate w to the number of distributions belonging to a thermodynamic state, or more particularly to the entropy of activation ΔS. w is related to the entropy of activation through the Boltzman-Planck relation

$$\Delta S = k\ln(w).$$

To take proper account of such effects, we must replace (Christian, 1965) the concept of potential energy of activation ϵ_A, by the Gibbs free energy of activation G, where

$$\Delta G = \epsilon_A - T\Delta S - p\Delta V.$$

In this work the $p\Delta V$ term is neglected since the volume change is relatively small at a constant pressure of 1 Atm. With the activation energy properly accounted for, Equation 2.34 now becomes

$$f = \nu_o \exp(\Delta S/k)\exp(-\epsilon_A/kT), \tag{2.35}$$

where ν_o is of the order of the Debye frequency ($\sim 10^{13}$ Hz). Comparing Equations 2.34 and 2.35, we obtain

$$\nu = \nu_o \exp\left(\frac{\Delta S}{k}\right). \tag{2.36}$$

With respect to the two-level model, ΔS corresponds to the entropy difference between the activated state and the initial state. This calculation of the entropy difference requires a detailed knowledge of the activated configuration and, since this can never be isolated for experimental study, it is only possible to make reasonable guesses about its nature. For some simple atomic processes reasonably successful attempts have been made by the use of semi-empirical methods. In particular, Zener (1951a) relate the change in vibrational entropy accompanying the movement of interstitial solutes, through a b.c.c. lattice, with the temperature dependent elastic constants. This approach has proved successful in accounting for experimental values of ΔS.

ΔG, the Gibbs free energy of activation, is the isothermal work at constant volume done in moving an atom from an equilibrium position to the top of the adjacent potential energy barrier. A local dilation of the 'lattice' has to be induced (by thermal fluctuation) to create a void sufficient to permit atomic rearrangement. The work done is largely associated with the elastic strain energy of the distortion.

Now,

$$\Delta S = -\left(\frac{d\Delta G}{dT}\right)_p \tag{2.37}$$

and if it is assumed that all the work is associated with the elastic strain energy, then from elasticity theory (Zener, 1951a)

$$\Delta G \propto \mu,$$

where μ is the shear modulus of the 'lattice'. In order to avoid evaluating the proportionality constant it is appropriate to consider the reduced parameter $\Delta G/\Delta G_o$, where ΔG_o represents the Gibbs free energy of activation at 0 °K. Hence,

$$\frac{\Delta G}{\Delta G_o} \sim \frac{\mu}{\mu_o}, \tag{2.38}$$

and this expression is satisfied only if the proportionality factor is independent of temperature. Combining Equations 2.37 and 2.38 gives

$$\Delta S \sim -\Delta G_o \frac{d(\mu/\mu_o)}{dT}.$$

Zener (1951a) defines ΔG_o as the driving energy E at all temperatures. Hence,

$$\begin{aligned} \Delta S &= -E\frac{d(\mu/\mu_o)}{dT} \\ &= -\frac{E}{T_m}\frac{d(\mu/\mu_o)}{d(T/T_m)} \\ &= \beta\frac{E}{T_m}, \end{aligned} \tag{2.39}$$

where $\beta = -d(\mu/\mu_o)/d(T/T_m)$ is a dimensionless scaling quantity, T_m is the melting temperature of the alloy and E is the driving energy ($\sim kT$). Since $d\mu/dT$ is always negative (Christian, 1965), β is a positive scaling constant and hence the expression for the entropy change is necessarily positive.

Equation 2.39 is stated (Zener, 1950) to be formally similar to a correlation proposed by Dienes (1950), namely,

$$\Delta S = \frac{E}{T_m} - \text{constant}.$$

Including this analysis in Equation 2.39, i.e. incorporating the negative constant, we obtain,

$$\Delta S \sim \beta \frac{kT}{T_m} - c_s, \tag{2.40}$$

where c_s is a constant. It should be noted that Equation 2.40 now allows for negative entropy changes if $c_s > \beta kT/T_m$. It has been assumed, Stearn and Eyring (1940), that both positive and negative values for ΔS occur in nature; the former corresponding to a loosening of the lattice and the latter to a stiffening. This point is of importance and will be discussed in Chapter 4. If, for the case n=1, we replace the frequency factor B appearing in Equation 2.17 by the atomic jump frequency ν given by Equation 2.36, with the entropy changes accounted for by Equation 2.40 then,

$$\begin{aligned} \frac{\Delta P}{P_o} &= -\tau p_o(\epsilon_o)\ln(\nu t) \\ &= -\tau p_o(\epsilon_o)\left[\ln(t) + \ln\left(\nu_o \exp(\Delta S/k)\right)\right] \\ &= -\tau p_o(\epsilon_o)\left[\ln(t) + \ln(\nu_o) + \beta\frac{T}{T_m} - c\right], \end{aligned} \tag{2.41}$$

where $c = c_s/k$. We call this expression the 'relaxation equation' for structural relaxation. Note that in comparison with Equation 2.17 the additional terms appearing in the relaxation equation arise due to the inclusion of the configurational entropy change introduced through the atomic vibrational frequency. The entropy change, in Equation 2.40,

is shown to be proportional to temperature and therefore, by Equation 2.36, the atomic vibrational frequency scales as $\exp(T)$. This temperature dependence accounts for the range of vibrational frequencies, in $Fe_{40}Ni_{40}P_{14}B_6$, varying from 10^{12} Hz at 550 K to 10^{46} at 660 K (see Section 2.2.4). In fact a plot of $\ln(\nu)$ vs T, for $Fe_{40}Ni_{40}P_{14}B_6$, as shown in Figure 2.14, with $\nu(\tau)$ taken from the literature (Chen (1981a), Berry and Pritchet (1976) and Balanzat (1980)), yields an approximately linear fit. Hence, the vibrational frequency does not assume a constant value over a range of annealing temperature as has been tacitly assumed in other published application of Primak's model. This has important consequences because the assumption of a constant vibrational frequency, over all temperatures, results in parts of the initial activation energy spectrum $p_o(\epsilon_o)$, revealed at different temperatures, to be displaced along the ϵ_o axis. Since, however, the vibrational frequency is temperature dependent, the effect upon the characteristic activation energy ϵ_o will be a simple displacement along the activation energy axis, which will be shown to produce a consistent fit over all temperatures investigated.

2.5 Structural Relaxation Mechanisms

Consider a binary alloy system composed of atomic species A and B. There are three basic mechanisms for the relative displacement of A and B atoms in crystalline materials (Christian, 1965). These mechanisms can also be interpreted as the basic processes occurring in amorphous alloy systems. The first of these, shown in Figure 2.15, involves the direct interchange of atoms on neighbouring sites. If this place exchange is imagined to occur by rotation of the atoms about their common centre of separation, it is expected that considerable distortion of the surrounding structure will be required. The process results in both A and B atoms being displaced in opposite directions relative to the remaining atoms.

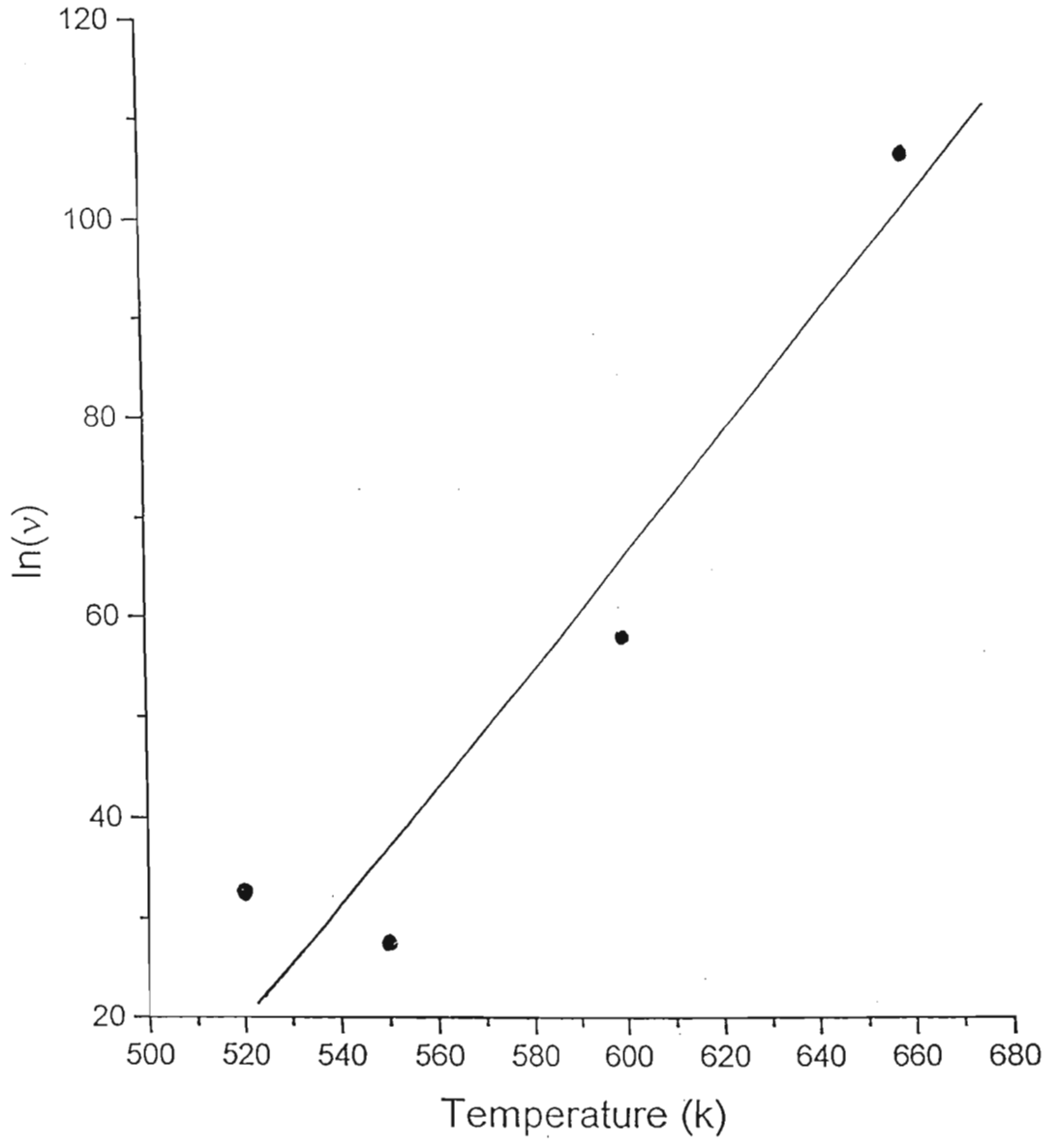

Figure 2.14: $\ln(\nu)$ vs Temperature for $Fe_{40}Ni_{40}P_{14}B_6$ ($\nu(\tau)$ taken from Chen (1981a), Berry and Pritchet (1976) and Balanzat (1980)).

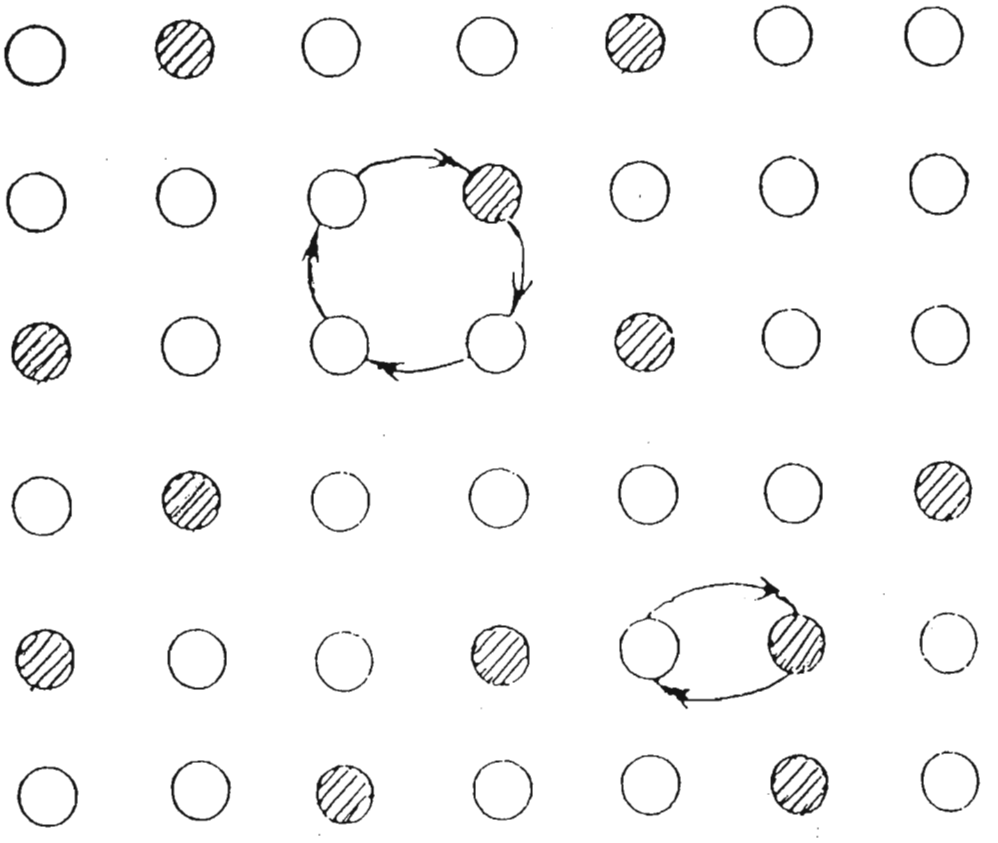

Figure 2.15: Schematic representation of a place exchange mechanism.

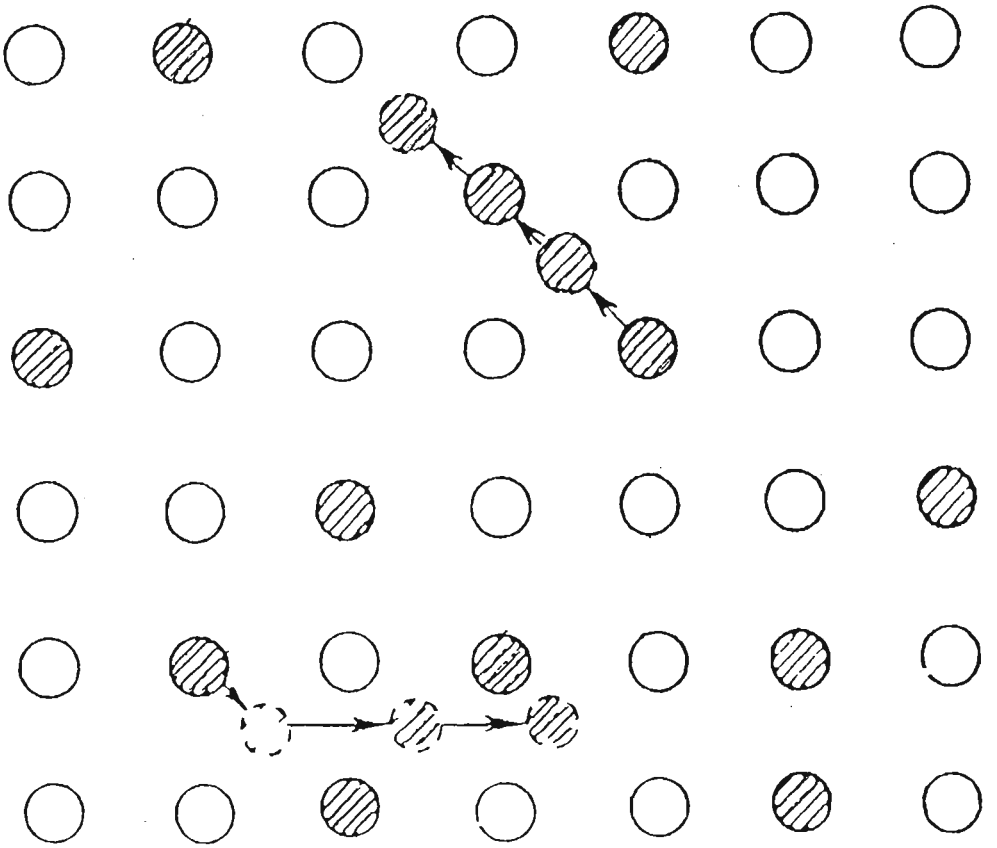

Figure 2.16: Schematic representation of interstitial diffusion.

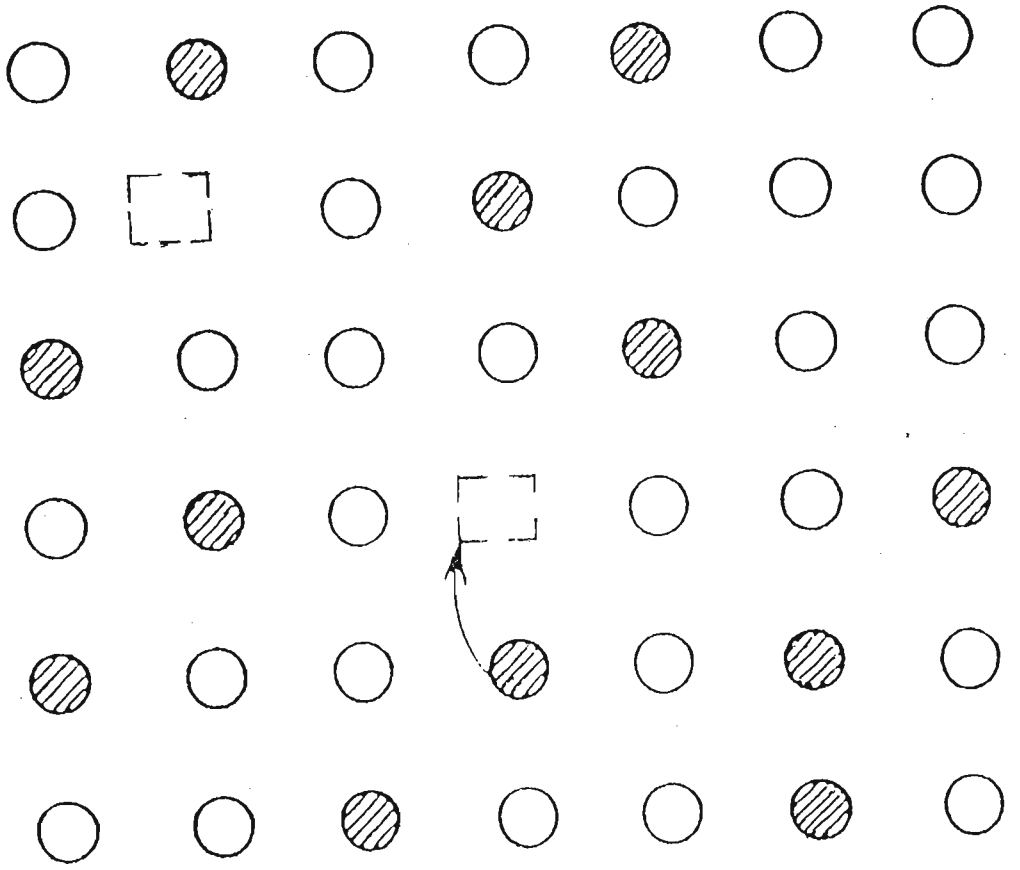

Figure 2.17: Schematic representation of migration of vacancies (free volume).

The second basic mechanism is the displacement of atoms through the interstices of the lattice as shown in Figure 2.16. An individual atom migrates by leaving a normal site and successfully occupying a series of interstitial sites. Such migration is only energetically favourable if the structure is relatively 'open', as in amorphous alloy systems due to the excess 'free volume'.

The third mechanism for atomic migration depends on the presence of vacancies (excess free volume) in the structure, as shown in Figure 2.17. An atom next to a vacant site may jump into that site, thus in effect changing places with the vacancy. The relative motion of A and B atoms result from the migration of vacancies through the lattice. If only B atoms can change places with a vacancy, the motion of B would take place with reference to an unchanging lattice frame of A atoms.

These mechanisms were thought to cover all possible processes for diffusion in the solid state. However, it is now recognised that cooperative motion of a large number of atoms is also feasible. The first type of cooperative process, suggested by Zener (1951b), is an extension of the place exchange mechanism, called ring diffusion. A small number of atoms move together in a ring, thus enabling the distortion (free volume) to be spread over a larger volume, and thereby reducing the free energy of the system. It is also noted that as the number of atoms in the ring increases the activation energy first falls steeply and then rises slowly.

A cooperative diffusion mechanism suggested by Nachtrieb and Hendler (1954) is based on the idea that structural relaxation occurs in the immediate vicinity of a vacancy (excess free volume). The disordering of a small number of atoms, amongst which the excess free volume is distributed, leads to rapid rearrangements by processes equivalent to diffusion in the liquid phase. The excess free volume itself is supposed to move through the structure by local 'melting' and 'freezing' of atoms one or two at a time. If the atomic configuration remained constant during migration, this would be

equivalent to vacancy diffusion. However, it is supposed that rearrangements occur at about the same rate as the movement of the free volume itself. According to this theory, the various atomic mechanisms described above may thus all be involved to some extent in the actual relaxation process.

It is usually assumed that one of the possibilities, outlined above, will be favoured at the expense of others, and thus dominate the diffusion process. The atoms, as postulated in the preceding section, vibrate about their equilibrium positions but spend most of their time in the vicinity of an atomic site represented by a minimum in the potential energy plot. In order to effect a rearrangement, an atom must temporarily acquire energy greater than the mean thermal energy of vibration. This activation energy depends on the nature of the process concerned. With reference to Equation 2.33, the probability of a particular process occurring decreases exponentially with the free energy of activation. The mechanism with the lowest activation energy will, therefore, be much more important than any other process with a slightly larger activation energy. Hence, the ratio of the probabilities of an atom moving in two different ways will strongly deviate from unity.

Competition between two or more mechanisms need only be considered if different geometries exist which favour different mechanisms. For example, in a crystalline system the activation energy for grain boundary diffusion is normally much lower than that for migration through the lattice. The lattice makes a greater contribution to the overall diffusion rate at high temperatures because fewer of the atoms are in grain boundary regions. As the temperature is lowered the effect of the lower activation energy for boundary motion becomes progressively more important, and at sufficiently low temperatures diffusion occurs predominantly along the boundaries. Similarly, one would also expect competing mechanisms in an amorphous system, especially with an evolving atomic configuration under structural relaxation.

Chapter 3

Experimental

3.1 Introduction

The structure sensitive properties of amorphous alloys exhibit a relaxation phenomenon when subjected to thermal treatments. Relaxation is enhanced by super-ambient temperature ageing or annealing. It is generally not possible to explain relaxation in disordered systems by the assumption of only one kind of kinetic process. To explain relaxation of the electrical resistivity of amorphous metal films Vand (1943) assumed independent kinetic processes of first order, possessing a single frequency factor, and distributed quasi-continuously in activation energy. He derived two methods for determining the original distribution from annealing experiments, namely

1. isothermal annealing - annealing in specimens at a constant temperature for different time periods, and

2. tempering - annealing whilst increasing the temperature at a uniform rate.

The latter approach presupposes that (a) the property can be measured while the substance is being heated, (b) the thermal coefficient of the property is known, and (c) the

temperature of the specimen can be increased at a constant rate, i.e. without the occurrence of phase changes, etc. As a result of these experimental difficulties, and to a lesser extent the increased mathematical complexity, the former approach has been adopted in the present investigation.

Theoretical descriptions of structure sensitive property variations are based almost entirely on the so-called chemical rate theory which introduces reaction rates on the basis of reasonable kinetic models. In essence the determination of a reaction rate consists of the determination of the concentration of possible kinetic processes q as a function of time yielding dq/dt directly (see Section 2.2.4). This approach is used only occasionally for transformation in solid metals and alloys, where qualitative metallography and X-ray techniques can be used for analytical purposes. In general, these techniques are of poor accuracy, are slow, tedious and require the examination of either

1. a series of samples reacted for various times with all other experimental conditions being held constant, or

2. one sample with the reaction being interrupted by some means whilst the analysis is carried out.

Both methods demand that the reaction be stopped at any required instant. The usual way is to rapidly decrease the temperature to some base measuring temperature. The difficulty with method (1) is to ensure consistency from sample to sample. The objection to (2) is that the analysis technique may change the kinetics.

The alternate approach, which is adopted in the present investigation, is to observe the change of some property that is a function of the concentration of available kinetic processes. Suitable properties include relaxation changes in linear dimensions (Kursomovic *et al*, 1980), electrical resistivity (Marcus, 1979), and magnetic properties (Luborsky, 1980). Specifically selected in this work are the measurements of length and

resistivity. The advantage of using these properties are rapidity and ease of automatic recording, with minimal disturbance to the available kinetic processes of the sample during the measurement stage. The disadvantage is that the absolute values of concentration q are not obtained. It is generally assumed, however, that there is a linear relationship between the value of the property observed and the concentration q. On the basis of this assumption the reaction rate is equal to the rate of change of the physical property.

The behaviour of amorphous alloys below the glass transition temperature is complicated. In order to perform true isoconfigurational measurements, the specimen must be annealed for long times at a temperature higher than that of the measurement temperature to ensure that structural relaxation does not take place during the time of measurement. Also, rapid heating and cooling is necessary to ensure minimal change in kinetics during the heating and quenching stages. Such isoconfigurational experiments are difficult, but have been performed on a number of transition metal-metalloid glasses (see, for example, Chaudhari *et al*, 1983).

3.2 As-Prepared Specimen Characteristics

The $Fe_{40}Ni_{40}B_{20}$ (Vacuumschmelze 0040) ribbon specimen was produced by the RQPC method and supplied by Dr Hilzinger of Vacuumshmelze GmbH. It has dimensions 3.0±0.1 mm wide by 0.025±0.002 mm thick along the entire length of the specimens investigated. The nominal composition of the sample was confirmed, using energy dispersive X-ray analysis (EDXA), by Miss F Graham of the Electron Microscope Unit, University of Natal, Durban. Analysis of the spectrum, shown in Figure 3.1, yielded 42.2±0.8 % Fe, 37.2±0.5 % Ni and 20.6±3.7 % B by elemental weight, which is in approximate accord with the manufacturers specification. Note the EDXA analysis, shown here, only serves to ensure that the composition of the alloy is roughly in the correct

composition range, and should not be interpreted as the exact composition.

The samples were cut into 20 cm lengths and cleaned with a methanol solution. To ensure maximum reproducibility in property variation, all samples were cut from the same specimen spool and prepared in batches. The samples, after attachment with a thermocouple (see Section 3.4), were then placed in a sample holder and stored in a desiccator. The sample holder consisted of a sheet of stiff paper with two rows of slits cut 5 mm wide and approximately 18 cm apart. Both ends of the sample were then fed into opposite slits. This ensured that

1. the thermocouples were not subjected to any undue stress, and
2. some of the bend stress, associated with winding the ribbon sample onto the spool, was alleviated.

3.3 Description of Apparatus

The instrumentation used here was developed to facilitate structural relaxation measurements of length and resistivity, and to test the predictions of the 'relaxation equation', developed in Section 2.4. The facility allows

1. isothermal annealing in an inert or vacuum atmosphere,
2. the use of direct heating currents for rapid heating,
3. a water cooled coaxial shield to aid in rapid cooling and to provide for an accurately controlled 'base' temperature, and
4. simultaneous measurements of length and electrical resistivity.

The apparatus was built at the Physics Workshop (University of Natal, Durban) headed by Mr W de Beer. The apparatus is shown schematically in Figure 3.2 and

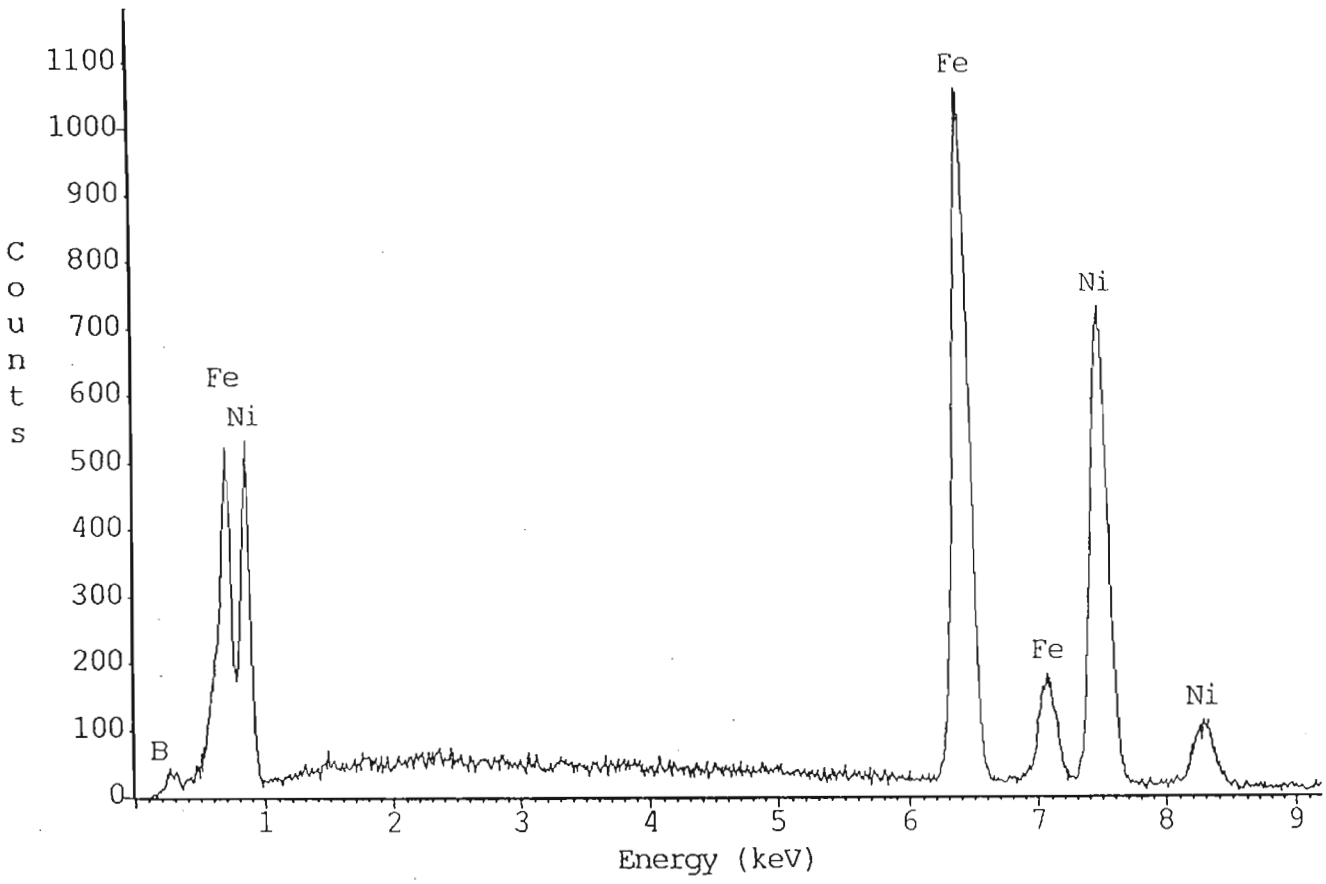

PROZA Correction Acc.Volt.= 20 kV Take-off Angle=30.00 deg
Number of Iterations = 5

Element	k-ratio (calc.)	ZAF	Atom %	Element Wt %	Wt % Err. (1-Sigma)
Ni-K	0.38261	1.103	21.83	42.21	+/- 0.78
Fe-K	0.38272	0.971	20.20	37.15	+/- 0.49
B -K	0.03132	6.591	57.97	20.64	+/- 3.68
Total			100.00	100.00	

Figure 3.1: Energy Dispersive X-ray Analysis of $Fe_{40}Ni_{40}B_{20}$.

photographically in Figure 3.3. With reference to Figure 3.2, the ribbon specimen J is firmly supported, on each end, by two rectangulr stainless steel vice clamps D. The top half of each clamp can be completely removed or secured with a specimen in place, by four stainless steel screws located at each corner of the clamp. The clamps were lined with nylon to provide for electrical and thermal insulation of the specimen, and for support of the heating contacts T and the four terminal resistance measurement probes S. The resistance and heating leads, after being stripped off their insulation, were soldered onto elongated rectangular copper pins. The pins, firmly pressed into grooves cut into the nylon lining, served as pressure contacts. The heating contacts were positioned furthest away from the ribbon ends so that as little of the actively annealed specimen lay inside the clamps. This helped reduce any end-effect errors that could have arisen in the temperature profile.

The solenoid magnet and cooling cylinder E, also shown schematically in Figure 3.4, was designed in accordance with the following criteria:

1. the need for a high magnetic field homogeneity (for magnetization measurements not considered in this work), particularly the axial field in the region of the detector coil,

2. a clear access through the solenoid bore for easy insertion of the ribbon specimen, and

3. a water cooling jacket, within the solenoid bore, to allow a flow of temperature regulated coolant around the specimen environment. This was to ensure that a base temperature of $\sim$ 27 °C was maintained, and to assist in rapid cooling after annealing.

The cooling cylinder consist of two thin-walled stainless steel cylinders, of different radii, concentrically positioned and the ends between them hermetically sealed by soft solder-

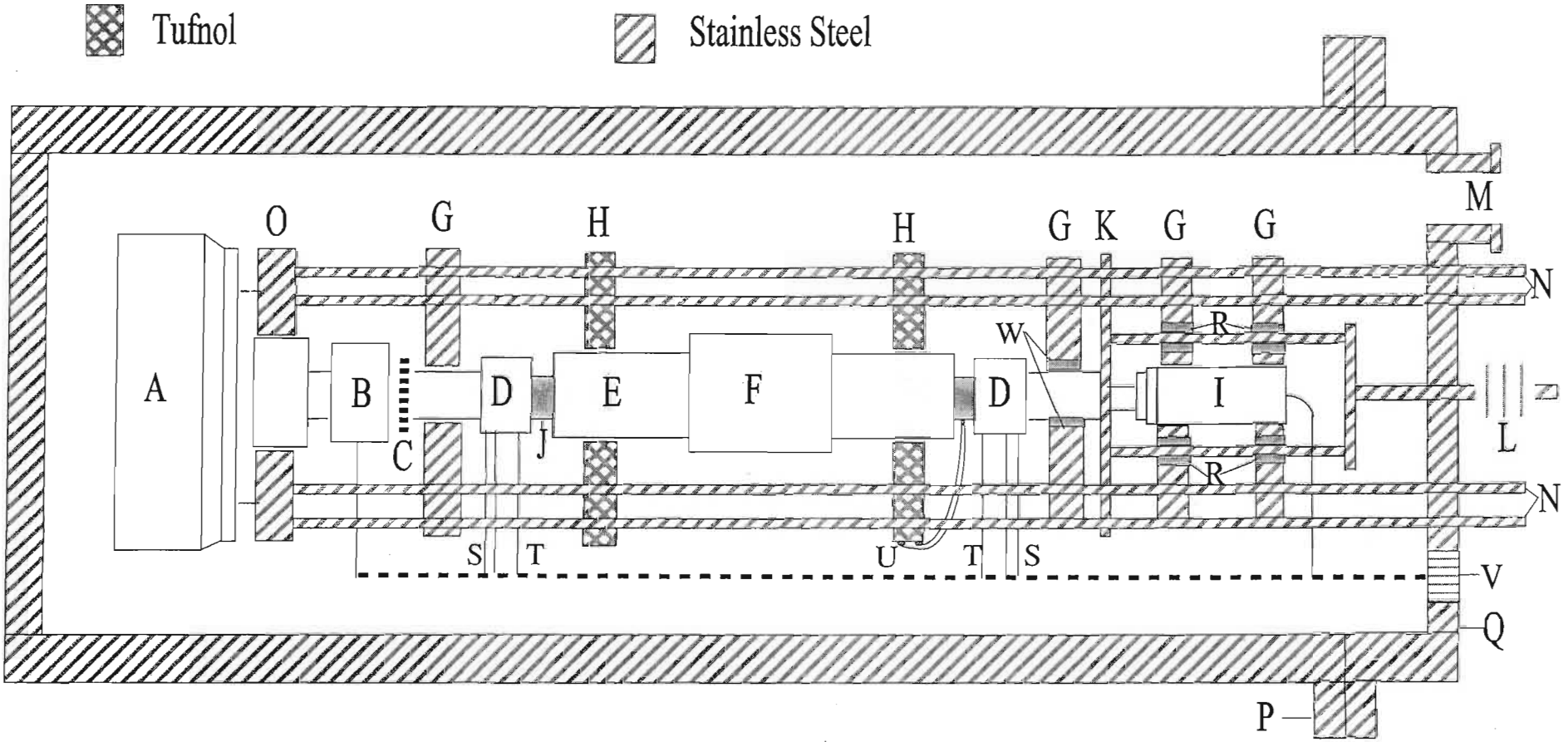

Figure 3.2: Schematic of apparatus for simultaneous measurement of length and resistivity during sub-T_g annealing.

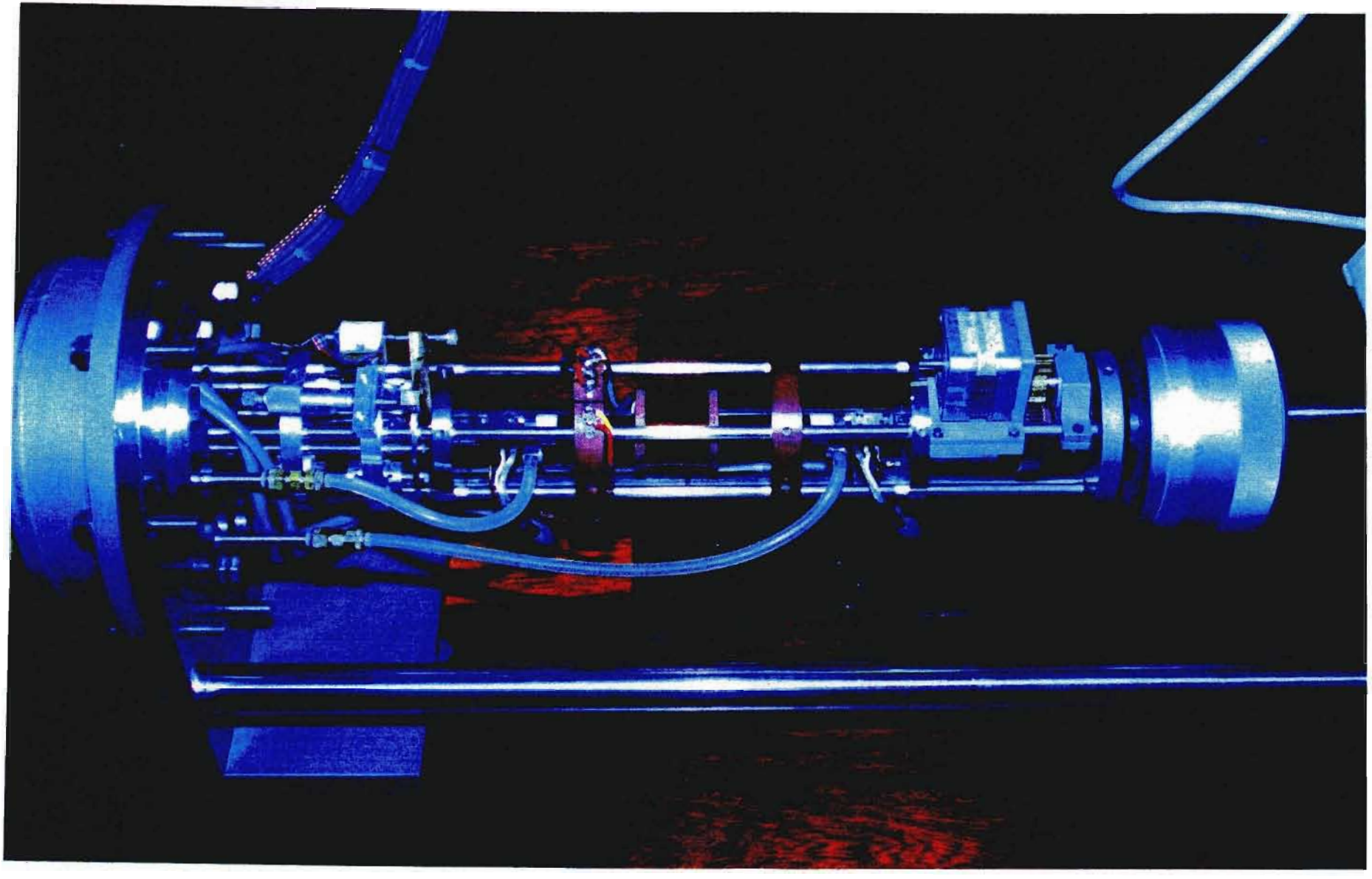

Figure 3.3: Photograph of apparatus for simultaneous measurement of length and resistivity during sub-T_g annealing.

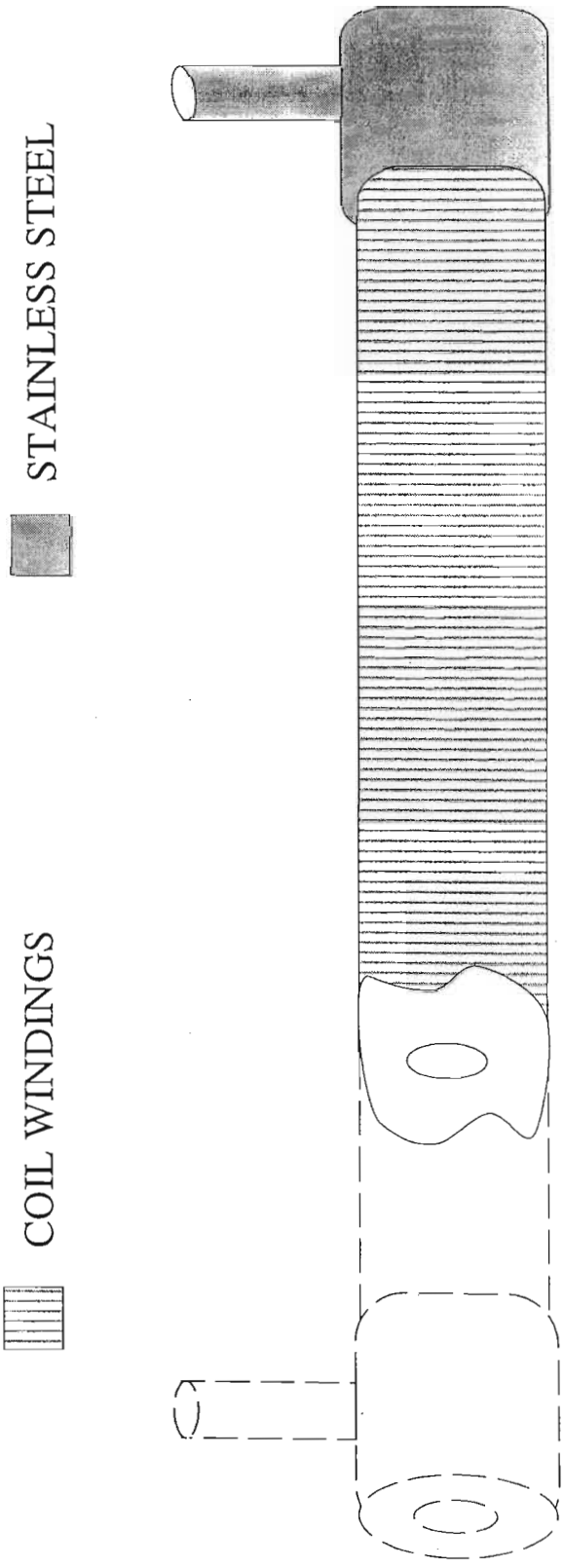

Figure 3.4: Schematic of the solenoid magnet with a water cooling jacket.

ing. The outer cylinder consist of a central tube of length 15 cm and diameter 10 mm with two endcaps, of length 1 cm and diameter 12 mm, welded onto either ends. The inner cylinder is a 17 cm long tube of 7 mm diameter.

Two 15 mm long and 2.5 mm diameter stainless steel tubes were then bored and soldered into the endcaps, as shown in Figure 3.4, to provide for an inlet and outlet access for the flow of temperature regulated water. The inlet and outlet tubes were connected, in series with the support tubes N (see later), to a Julabo heater/pump via 5 mm diameter PVC piping. The PVC pipes were clamped over the inlet and outlet tubes with specially designed hose clamps. The Julabo heater/pump (not shown here), immersed in a 20 L water bath, regulated the temperature of the bath to a preset temperature of 27±1 °C. A small quantity of household bleach was added to the water bath to prevent the growth of algae, which was found to hinder the water flow and ultimately the efficiency of temperature regulation around the sample stage.

A solenoid coil, wound on the indented region of the outer cylinder with 29 gauge insulated copper wire, consisted of 1420 turns stacked in four layers. The axial homogeneity of the solenoid, although not required in this work, was checked using a commercial gaussmeter and variations were found to be less than ±1% over the central 10 cm region of the solenoid. A magnetometer detector coil F, slipped over the solenoid magnet, was positioned in the central core region. The detector coil consisted of several thousand turns of 42 gauge copper wire wound onto a tufnol bobbin.

The left specimen clamp D is coupled directly to a linear variable differential transformer (LVDT) I and the right clamp to a micrometer screw A. The micrometer screw can be driven by a stepper motor B through a gear coupling system C. The stepper motor control is interfaced to a PC thus, allowing its functions to be fully computer controlled. The stepper motor can be rotated either in a clockwise or counter-clockwise direction with a choice of stepping speeds. With a specimen firmly secured between the

clamps, the micrometer screw together with the stepper motor allows for;

1. balancing and calibration of the LVDT, and

2. tensioning of the sample.

Support for the system was provided by four stainless steel tubes N which extended from the outside of the specimen chamber, through the end plate Q, to a hollow disc O. The support tubes were internally connected through O so that a continuous water flow, from the temperature controlled water bath, could be circulated through them in series with the water cooling jacket. Additional support was provided for by a much heavier stainless steel tube, fixed to the end plate Q, on which the entire assembly rested. The solenoid magnet, specimen clamps, micrometer screw and the LVDT were aligned and supported by circular support discs threaded through the support tubes N, and fastened into position by screws that extended through the collar of the discs. All support discs G were made of stainless steel. Support for the solenoid stage, however, was provided for by tufnol discs H. The solenoid magnet was also locked into position by plastic screws extending through the collar of the tufnol discs. A pair of contacts U, for the themocouple leads, was located on the collar of the left-most disc H. Thermocouple leads extending from a temperature controller were permanently secured on the contacts U Thermocouple leads from the sample (see Section 3.4) were then soldered onto these contacts.

The discs G supporting the specimen clamps were designed to allow for lateral movement. To reduce friction on the system, the support disc of the specimen clamp on the side of the LVDT was fitted with a special bracer bearing W. To ensure minimum friction, the bearing was frequently oiled with a high grade vacuum oil. The specimen clamp on the side of the LVDT was also coupled to an adapter plate K. The shaft of the LVDT was fixed to the adapter plate so that relative movement of the plate was

translated to the LVDT shaft. The specimen was kept tensioned (~0.4 N) by a cage arrangement extending from the adapter plate to the outside of the chamber where it was spring tensioned by spring L. The rods that extended from the adapter plate K to the spring L were fed through low friction ball bracers R, located in the walls of the support plates G. The ball bracers R, apart from providing for a relatively free conveyance of the cage arrangement, provided primary support for the adapter plate K.

All electronic leads were ducted through two Cannon 19 connectors to the supporting electronics via the interface plate Q. The connectors were mounted onto the interface plate with 'o' rings to provide a vacuum tight system. The chamber cover P was supported by two cylindrical glide rails that allowed it to slide open or shut. To ensure adequate vacuum sealing during the measurement series, the collar of the chamber cover was fitted with an 'o' ring. The cover was then fastened, against the 'o' ring, onto the interface plate Q with stainless steel bolts. The vacuum flange M, connected to a vacuum line, has three inlet admissions controlled by valves. The main inlet was connected to a diffusion pump and used when a hard vacuum ($\sim 10^{-4}$ Torr) was required. Another inlet was connected to an argon (or helium) cylinder and used to flood the specimen chamber with the argon (or helium) gas, required for annealing under an inert atmosphere. The third inlet admited air into the specimen chamber. The vacuum line was, therefore, used for pumping and purging of the specimen chamber.

3.4 Specimen Temperature Regulation

There exist two conventional heating methods for isothermal annealing, namely furnace annealing and direct Joule heating. The furnace annealing method, although extensively used, has several disadvantages, namely

1. since a finite time is required for convective heating of the sample to the furnace set-point temperature, there exist complications in establishing the effective annealing time,

2. the sample needs to be removed and rapidly quenched to a 'base' temperature before each property measurement, and

3. difficulty in adapting to an inert or vacuum atmosphere.

The direct Joule heating method, however, which has not been extensively used in metals research, has many potential advantages over conventional furnace annealing, namely;

1. rapid heating to a setpoint temperature,

2. minimal temperature gradients over the specimen length,

3. easy adaptability to all atmospheres (inert or vacuum), and

4. rapid cooling to a base temperature.

The need for an inert atmosphere is evident from the densification measurements of Kursomovic *et al*, where the annealing procedure, conducted in free air and thus prone to oxidation effects, resulted in an oscillatory behaviour superimposed on the relaxation response (see section 2.3). In fact, Marcus (1979) reporting on resistivity measurements in Pd-Si-Sb claim that samples annealed in the presence of oxygen showed a brownish discoloration and that resistivity behaviour was irreproducible and distinctly different from that of unoxidized samples. Preliminary experiments to confirm the feasibility of the direct Joule heating method was conducted by Doyle (unpublished). Temperature measurements, using ultra-fine thermocouples spot-welded onto the specimen, showed a maximum temperature variation of ± 1 °C along the specimen when heated in the range

150 °C to 250 °C, by passing a direct current through them. This temperature variation was considered adequately uniform for the proposed annealing experiment.

A difficulty with the investigative approach used here is the method of attachment of a thermocouple to the ribbon. The thermocouple junction must attain yet not perturb the local temperature. Also, the thermocouple probe should be held in intimate contact with only a small portion of the ribbon to avoid steep temperature gradients in the vicinity of the measuring junction. To minimize this temperature measuring error, the following precautions were exercised;

1. the local morphology of the ribbon at the surface was disturbed as little as possible by the presence of the thermocouple, and

2. the thermal resistance between thermocouple and ribbon surface was kept to a minimum.

The precautions listed above are realized if the thermocouple junction is kept relatively small and spherical. A spherically small thermocouple junction ensures minimum surface contact between thermocouple and sample. An added advantage is the symmetry of a spherical junction; since any asymmetry in the thermocouple junction leads to an erroneous thermocouple voltage and, therefore, to spurious errors in temperature measurement.

Bare ultra-fine (48 gauge) thermocouple wires with nominal compositions $Ni_{90}Cr_{10}$ (Chromel) and $Ni_{95}(Al+Mn+Si)_5$ (Alumel) were used to fabricate type K thermocouples. The thermocouple ends were welded together under reducing conditions, using an oxy-acetylene torch. Support during welding was accomplished by twisting the wires together, about three turns, and leaving the ends to be welded extended about 2-5 mm side by side beyond the twist so that when the ends were melted, the thermocouple junction was held to both wires by the surface tension. This established a permanent, low resistance

electrical contact. The junction was found to be optimally formed when the twisted end was pointed down during welding.

The thermocouples were then very lightly spot-welded onto the 20 cm length ribbon specimens, in a manner that would not have caused any undue stress to the specimen and thermocouple probe. Care was also exercised in minimizing cold-working and contamination (for example, salt from perspiration) of the thermocouples. Although the spot-welding technique is simple, a certain amount of skill is required to obtain consistent and satisfactory welds. Excessive heating and pressure result in localized crystallization of the sample and deformation of the thermocouple junction, respectively. Although the former will be masked, its presence is still undesirable. The latter leads to a flattening out of the junction, thus destroying the symmetry which leads to an erroneous thermocouple voltage. The thermocouple leads were, after attachment to the specimen, electrically insulated by coating with nail varnish.

The temperature controller used was a commercial unit (Lakeshore, model DRC-91C). A model 9305 thermocouple input card, an accessory to the DRC-91C unit, utilized a secondary sensor to monitor the reference junction (room) temperature and provided curve compensation for the type K thermocouple. An offset adjustment, adjacent to the thermocouple input block, was used to compensate for any thermocouple variation and system irregularities. Maximum control flexibility was provided for by a three mode PID (Proportional, Integral and Derivative) controller. Individual settings for proportional band, reset time, and rate time allowed the controller to be fine-tuned. The DC output heating current from the temperature controller was chopped, using a chopper stabilized amplifier, at a frequency of 1 KHz. The resulting AC heating current allowed for compensation of any asymmetry effects in the thermocouple junction.

3.5 Length Measurement

Length measurement was accomplished by the linear variable differential transformer. The LVDT signal was detected using phase sensitive detection (lock-in amplifier) to increase the signal to noise ratio, thus permitting accurate amplitude measurements. The LVDT was calibrated by means of the micrometer screw, where any lateral displacement of the micrometer screw was translated to the LVDT. The micrometer screw had a resolution of 1 μm when the usual steps were taken to overcome gear play. The LVDT response as a function of displacement is shown in Figure 3.5. The ultimate sensitivity of the LVDT was approximately 0.05 ± 10^{-2} mm, and limited by friction in the tensioning spring and by the LVDT itself.

The optimum operating parameters of the lock-in-amplifier were found to be:

- Reference signal frequency - 5 KHz
- Sensitivity - 20 mV,
- Time constant - 300 ms,
- Reference signal voltage - 0.1 V.

3.6 Resistance Measurement

The resistance measurement technique employed in this investigation is an extension of the well known AC Kelvin double bridge method. The standard Kelvin bridge was considered unsuitable for the present work since the lead resistance is comparable with the sample resistance. To circumvent this difficulty, voltage followers were introduced into the bridge arms, as shown in Figure 3.6. The voltage followers, which are essentially unity gain operational amplifiers, acted as high impedances to AC currents. Therefore,

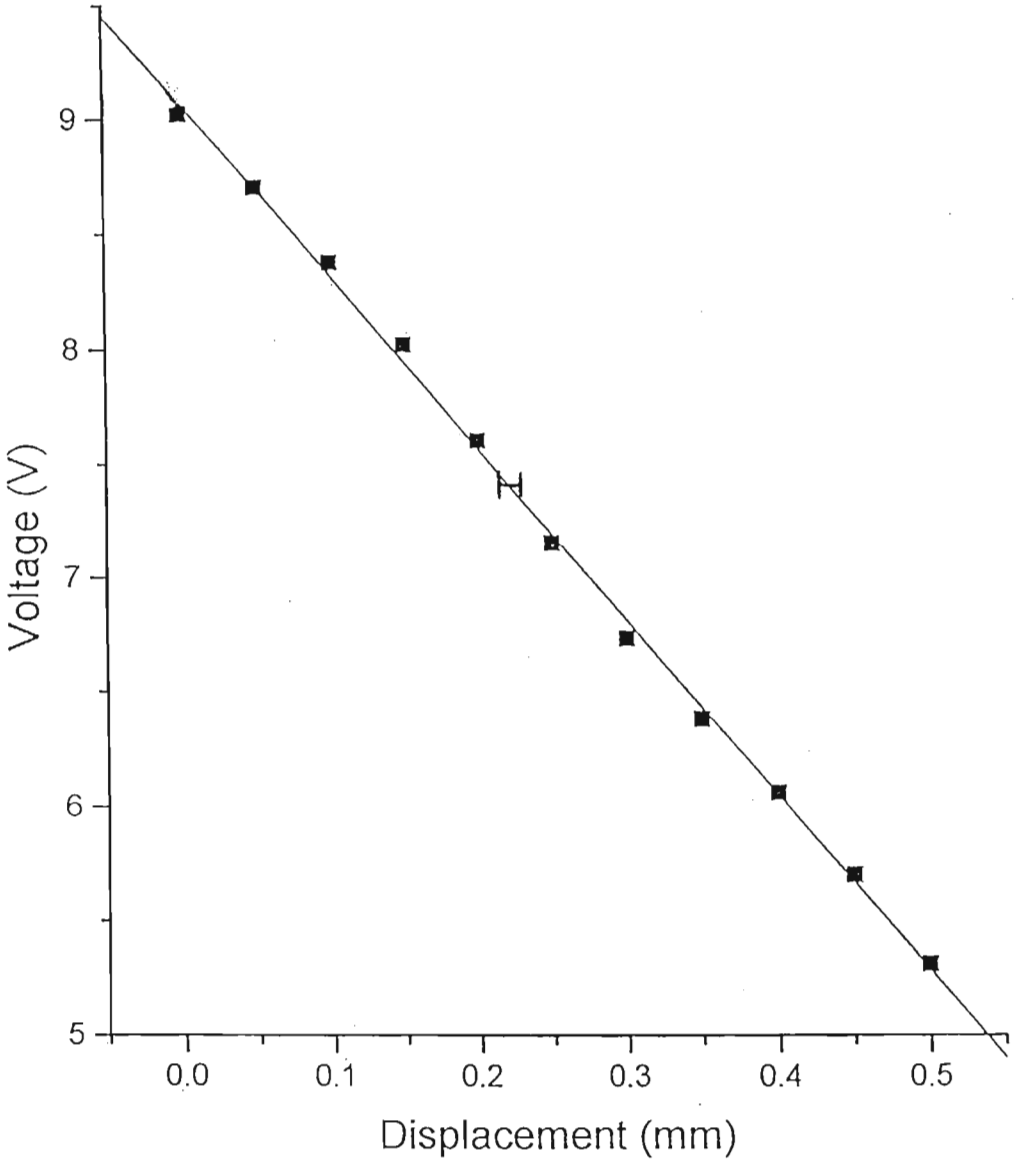

Figure 3.5: LVDT response as a function of displacement.

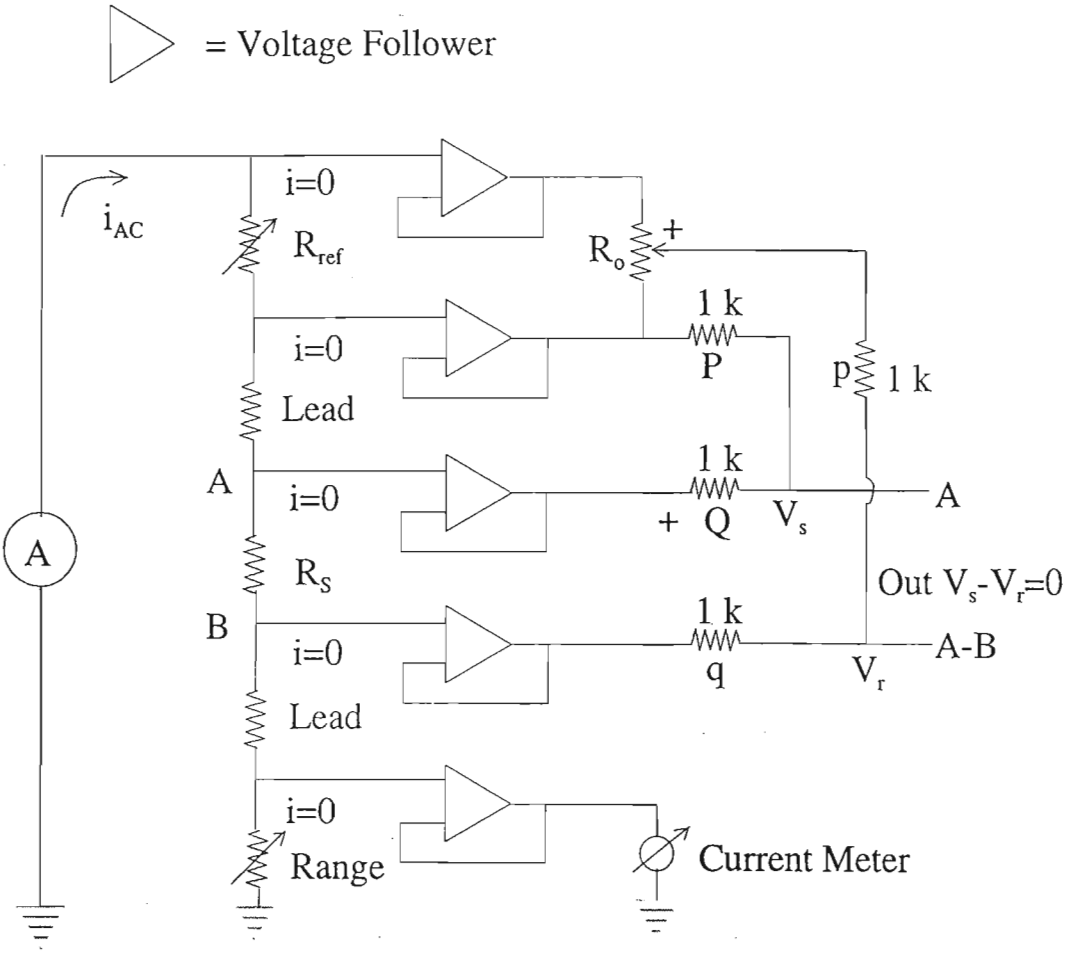

Figure 3.6: Schematic of the four terminal AC bridge employed for resistivity measurement.

in spite of the relatively high lead impedance, there was negligible current in the voltage leads. The voltage followers permited us to introduce a second important modification. Since the current in the voltage leads were negligible, we introduced a decade voltage divider R_o, as shown in Figure 3.6. Introduction of the voltage followers and voltage divider allowed direct comparison of the reference resistance R_{ref} with the sample resistance R_S, without the need for changing the resistance ratios in the bridge arms. Therefore, fixed resistors of 1 kΩ were used for P, Q, p and q, as shown in Figure 3.6, leading to unit resistance ratios (P/p and Q/q) in the arms. The AC bridge was able to detect resistance changes as small as $1x10^{-5}$ Ω. All results were obtained in the form of a relative variation in resistance $\Delta R/R_o$ (from which the relative variation in resistivity $\Delta\rho/\rho_o \sim \Delta R/R_o$).

A lock-in-amplifier also provided for phase sensitive detection. The optimum parameters of the lock-in-amplifier were found to be:

- Reference signal frequency - 2.5 KHz,
- Sensitivity - 100 mV,
- Reference signal voltage - 10 mV,
- Time constant - 1 s.

3.7 Data Capture and Control

The data capture and control hardware system, as shown schematically in Figure 3.7 and photographically in Figure 3.8, comprised of a PC with supporting IEEE 488 and PC-30 interfaces, an HP data acquisition unit (model 3421A), a pair of lock-in-amplifiers, a temperature controller and a bank of relays.

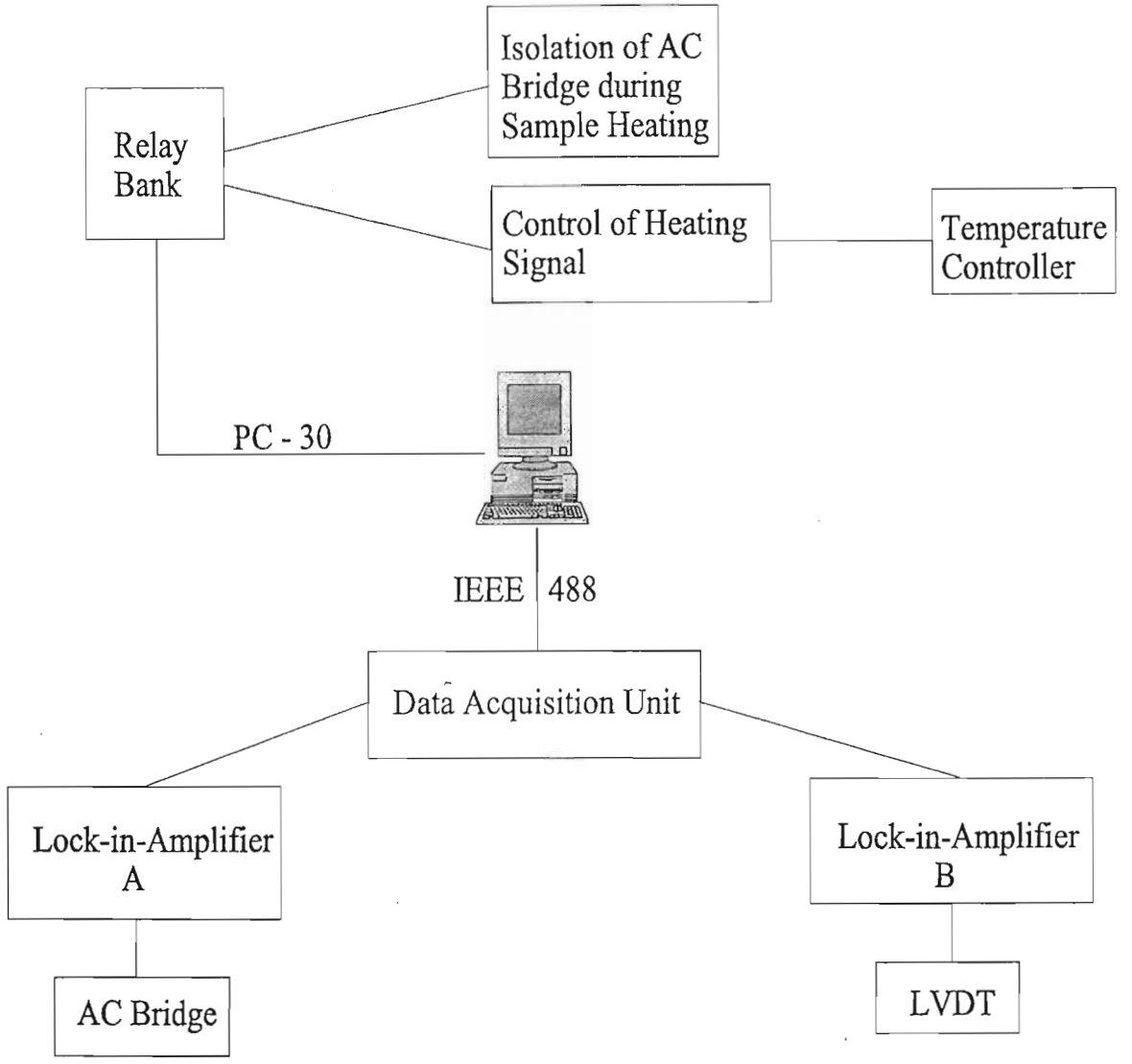

Figure 3.7: Schematic of the data capture and control peripherals.

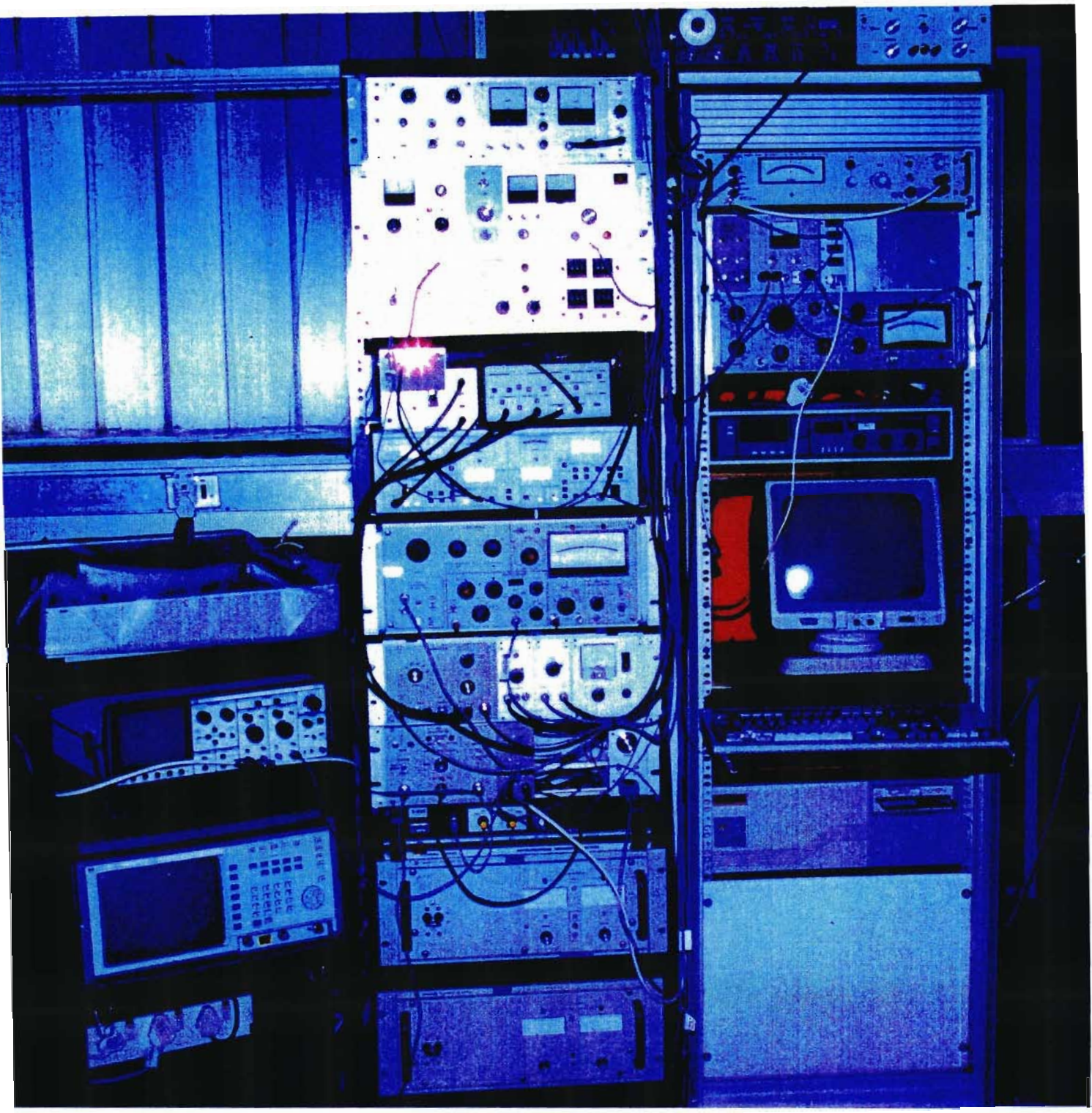

Figure 3.8: Photograph of the supporting electronics.

Each interface was dedicated to a specific hardware facility. Both length (LVDT) and resistivity (AC bridge) measurements from the respective lock-in amplifier were relayed to the HP data acquisition unit, digitized and, thereafter, relayed via the IEEE 488 bus to the PC. The data was then sequentially stored in a file and later retrieved for analysis. The PC-30, an A/D - D/A converter, formed part of the main control peripheral. The D/A PC-30 converter was programmed in 'Turbo Basic' to send properly coordinated control signals, using the PC's internal clock as a timer, to a bank of relays. The relays were programmed to

1. switch the heating current, from the temperature contoller, ON or OFF thus, controlling the time needed for active annealing, and

2. isolate the AC bridge from the heating current.

The annealing program, at each isothermal temperature, consisted of a total annealing time of 2000 s, with the length and resistivity values sampled at the following time intervals (in seconds):
10, 20, 30, 40, 80, 120, 160, 200, 240, 360, 420, 520, 600, 800, 1000, 1200, 1400, 1600, 2000.
The hardware peripherals and the control software allowed for complete automation and, therefore, eliminated any operator errors in timing. Before sampling, the specimen temperature was rapidly lowered to the 'base' temperature. The total annealing time was therefore divided into sub-intervals, where each sub-interval was determined by the time period between consecutive sampling times, for example, the sub-interval between the 200^{th} and the 160^{th} sampling is 40 s. The control pulses required for annealing at each sub-interval, shown schematically in Figure 3.9, was coordinated as follows:

1. connections to the AC Bridge were isolated, thus protecting it from the relatively high heating current,

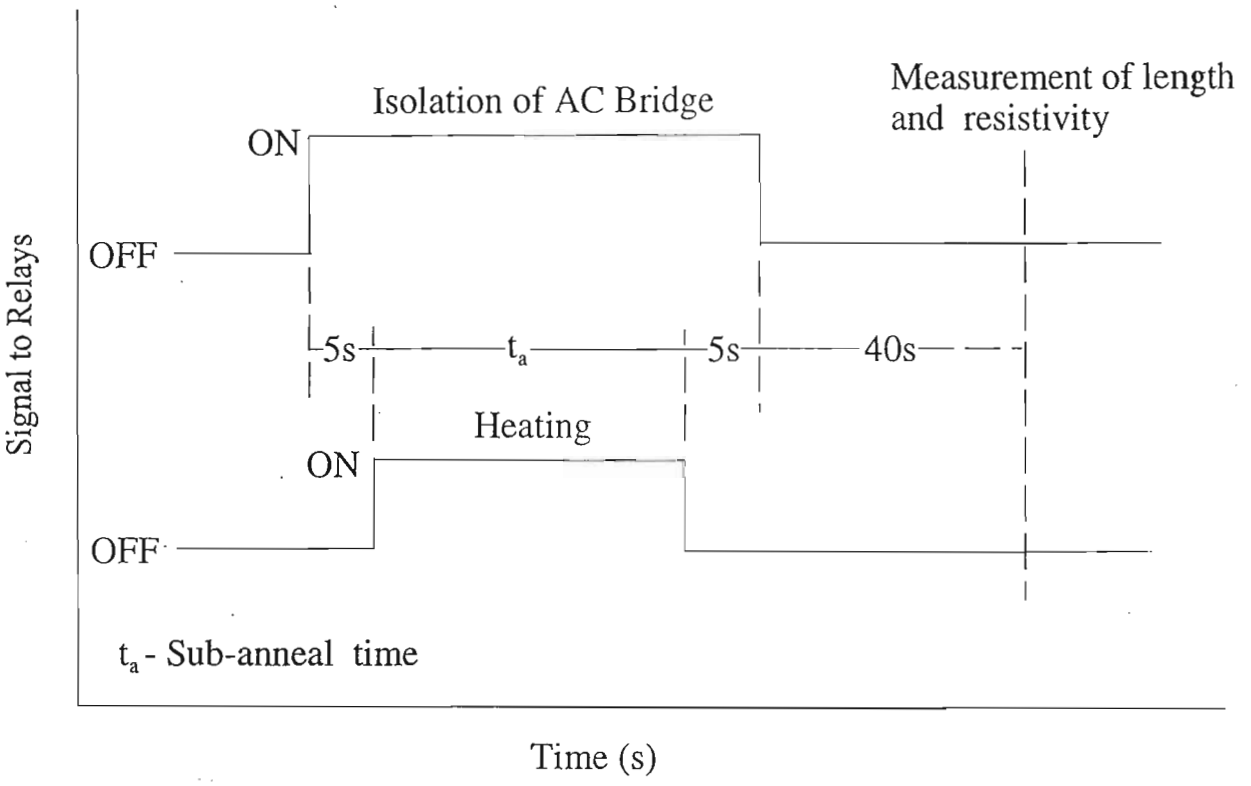

Figure 3.9: Control pulse schedule for a sub-anneal.

2. the heating current was then activated and controlled for the desired sub-interval,

3. after annealing at each sub-interval the heating current was turned off and the specimen temperature rapidly fell to the regulated 'base' temperature ($\sim$ 27 ^{o}C),

4. the electronics were then allowed to stabilize for 40 s before the relevant properties were measured, and

5. the next sub-interval anneal was then initiated.

This procedure was repeated for each sub-interval until the entire program for the total annealing time was completed.

3.8 Modus Operandi

Both length and resistance measurements were conducted at a 'base' temperature, i.e. at the regulated temperature of the cooling water that flowed through the cylindrical cooling and support tubes. The water flow was initiated at least an hour before the start of the experiment to allow the specimen environment to come into thermal equilibrium with the cooling water. A new specimen for each annealing temperature, fitted with a thermocouple, was then clamped into position, and the thermocouple leads were soldered onto the thermocouple contacts. The micrometer screw was then activated via the stepper motor to bring the LVDT within range on the associated Lock-In-Amplifier panel. The chamber covers was then bolted shut and the apparatus was thoroughly cleared of air by pumping down to a pressure of approximately 10^{-4} Torr, after which it was purged with argon to a pressure of approximately 1 Atm and allowed to come into thermal equilibrium with the cooling water. The control software was then activated, and the data collected was analyzed. The control software, which allows complete automation of the annealing program, is listed in Appendix A.

Chapter 4

Results and Discussion

4.1 Introduction

The experimental results obtained here will be analysed and compared with the predictions of the extended Primak model, considered in Section 2.4. We have chosen to study the annealing response of two structure sensitive properties (namely length and resistivity) so that a check on the consistency of the scaling parameters, inferred from the experimental results, is possible.

4.2 Experimental Results

The experimental results for relaxation of density (length) and resistivity, with sub-T_g super-ambient isothermal annealing procedures, are shown in Figures 4.1 and 4.2, respectively. The same data plotted against $\ln(t)$ in Figures 4.3 and 4.4, respectively, show, with the exception of a small regime at low T and low t, that '$\ln(t)$ kinetics' is obeyed over most of the T-t field investigated. These results do not show any oscillatory behaviour of the type observed by Kursomovic *et al* (1980) (see Section 2.3), as is ex-

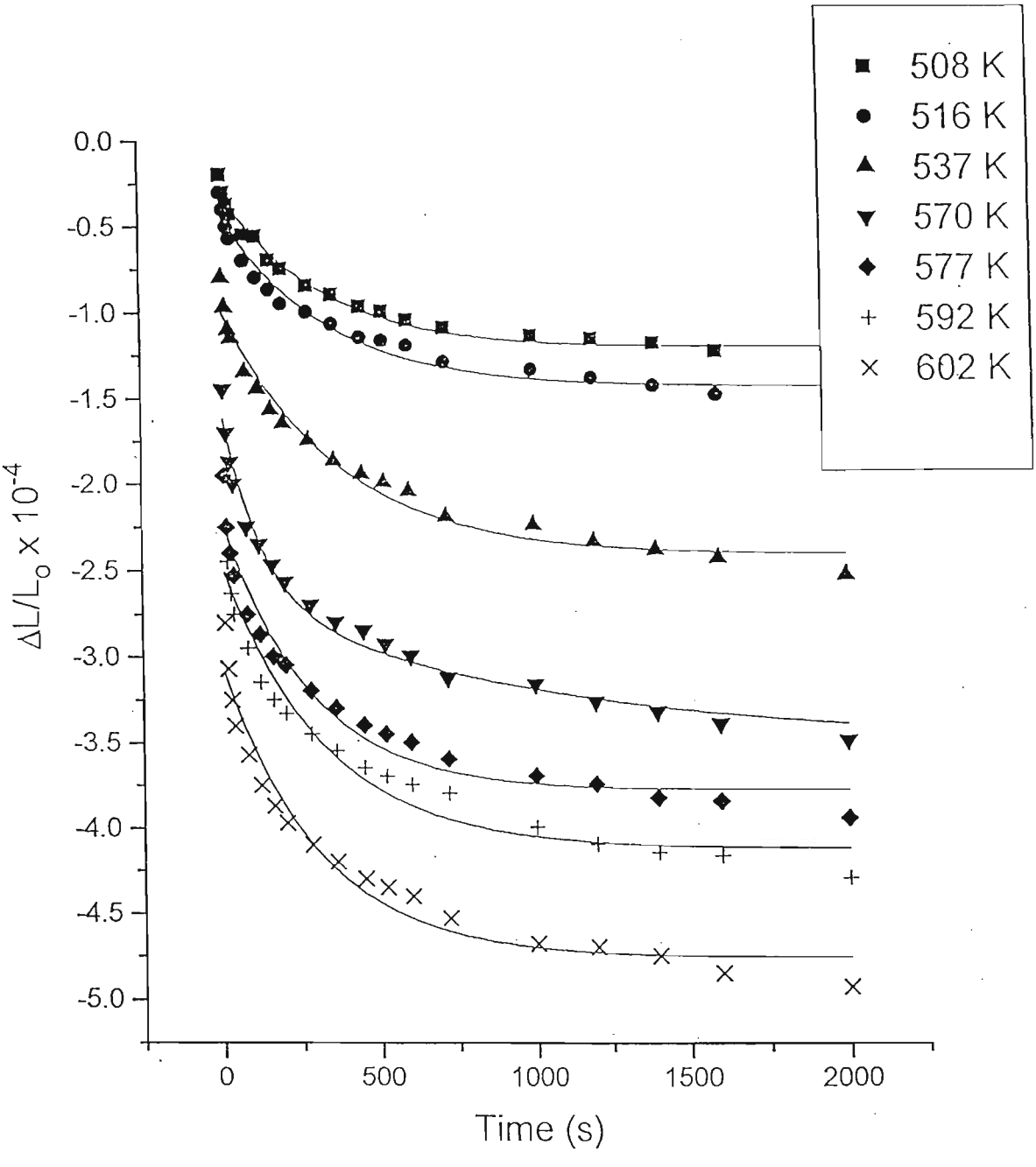

Figure 4.1: Fractional change in length vs annealing time, for the various isothermal annealing temperatures indicated.

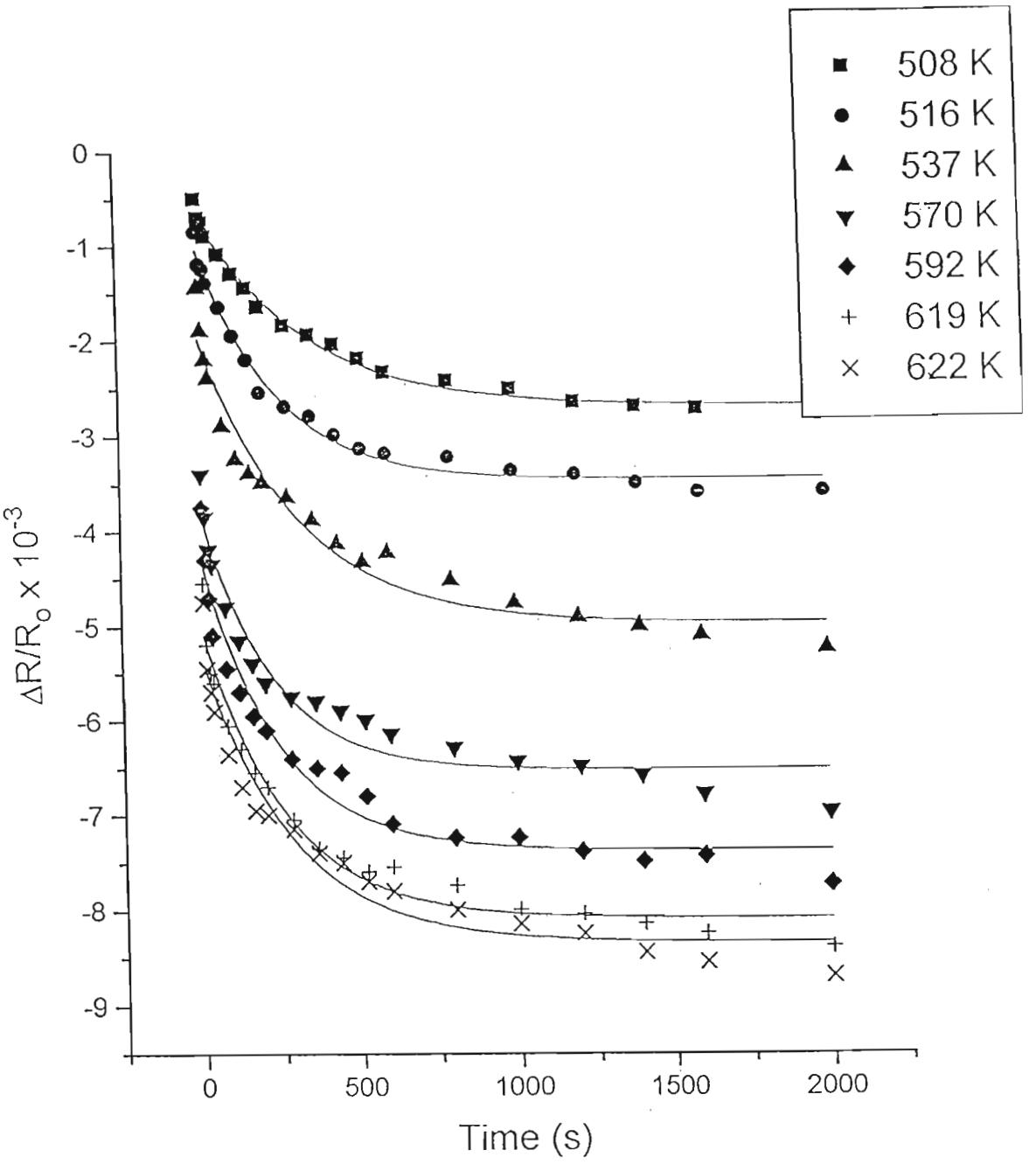

Figure 4.2: Fractional change in resistivity vs annealing time, for the various isothermal annealing temperatures indicated.

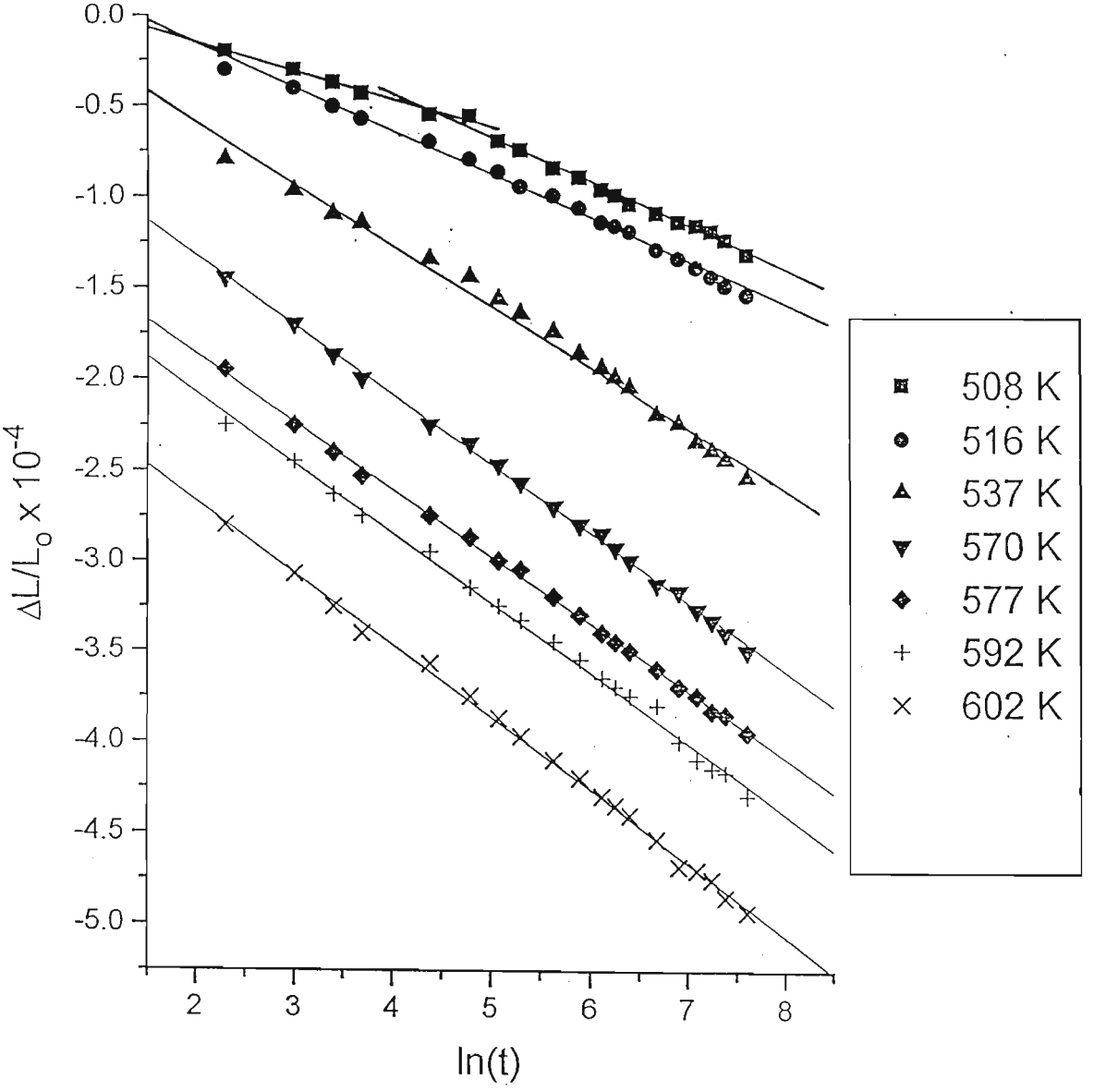

Figure 4.3: Fractional change in length vs $\ln(t)$, for the various isothermal annealing temperatures indicated.

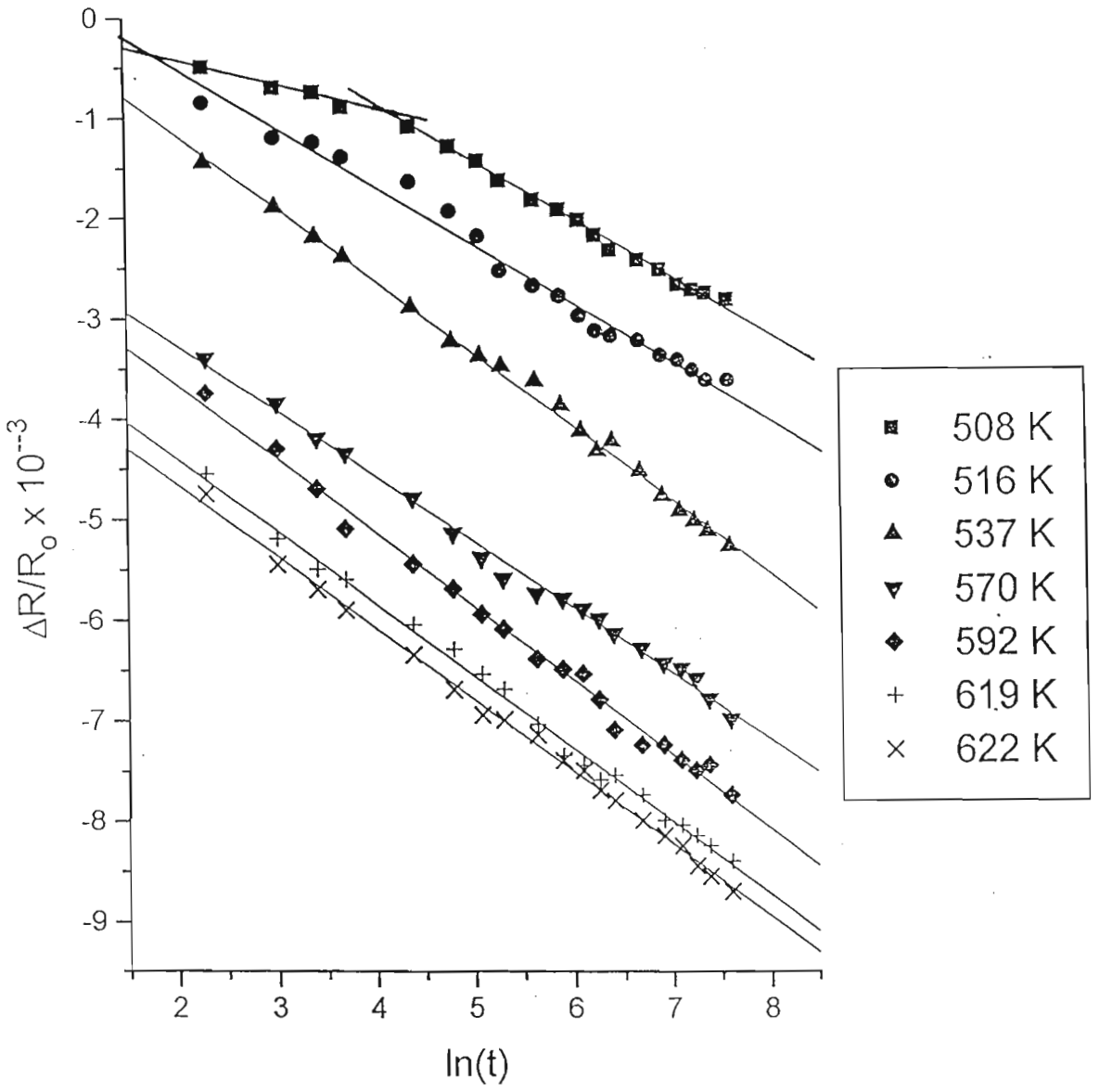

Figure 4.4: Fractional change in resistivity vs $\ln(t)$, for the various isothermal annealing temperatures indicated.

pected for measurements made in an inert atmosphere. These plots (Figure 4.3 and 4.4), which include data for a number of independent isothermal anneals, form a family of nearly straight lines that are roughly parallel to each other. This implies that the product of the initial activation energy distribution $p_o(\epsilon_o)$ and the temperature τ $(= kT)$, appearing in the gradient $(-\tau p_o(\epsilon_o))$ of Equation 2.17, is approximately constant over the range of annealing temperatures investigated. It is, therefore, generally assumed that $p_o(\epsilon_o)$ remains constant during isothermal annealing. This condition is considered to be important for the observation of $\ln(t)$ kinetics (see, for example, Gibbs *et al*, 1983). The validity of this assumption is, however, questioned in the following section.

4.3 The Initial Activation Energy Spectrum $p_o(\epsilon_o)$

4.3.1 The Behaviour of $p_o(\epsilon_o)$

The initial activation energy spectrum $p_o(\epsilon_o)$ is generally considered a complete representation of the kinetic behaviour for a suitable property P with isothermal annealing. Honig (1954) discusses an exact mathematical inversion of the isothermal annealing data $P(t)$ to obtain $p_o(\epsilon_o)$ by means of a Laplace transform. To use such a method, it is necessary to know the exact analytical form of dP/dt over the entire T-t field. Since, however, only processes in a small range of activation energies occur simultaneously, and only a small portion of the possible range of activation energies can be observed in an isothermal annealing program, Primak (1955) refutes the practical application of Honig's method. Furthermore, interpretation of the data consists of finding the initial activation energy spectrum $p_o(\epsilon_o)$ revealed at each isothermal temperature and then, through a proper choice of the order n and the frequency factor ν, the complete activation energy spectrum can be obtained. This, however, cannot be done using the form of Equation 2.17 because of complications associated with unknown variations in the frequency factor ν

with temperature T. In the absence of a treatment to obtain the exact form of the initial activation energy spectrum, $p_o(\epsilon_o)$ has been generally assumed, for simplicity, to be a constant.

Plots of $\tau p_o(\epsilon_o)$ versus temperature T, as extracted from the slope of the isotherms in Figures 4.3 and 4.4 using Equation 2.17, are shown in Figures 4.5 (length) and 4.6 (resistivity). The slope of these plots, which is proportional to $p_o(\epsilon_o)$, has two different values over the temperature range investigated. It is, therefore, immediately apparent that the assumption of a constant initial activation energy spectrum is invalid. The value of $p_o(\epsilon_o)$ at temperatures below approximately 540 K is higher than that above 540 K. This behaviour has not been reported in similar isothermal relaxation investigations.

The two value behaviour of $p_o(\epsilon_o)$ is, however, apparent in calorimetric investigations. Shown in Figure 4.7 is a plot of a heat flow curve for a $Fe_{40}Ni_{40}B_{20}$ sample, obtained by Scott (1981) using differential scanning calorimetry. The figure shows a change in slope at a temperature of approximately 540 K in agreement with the trend found in Figures 4.5 and 4.6. In order to make a direct comparison between the two sets of results, we need to associate the heat flow curve to the initial activation energy spectrum $p_o(\epsilon_o)$. The thermal spectrum, presented in Figure 4.7, was obtained by heating an as-quenched sample to 400 °C, quenching it to room temperature and immediately reheating it to 400 °C at a heating rate of 20 K/min (i.e. tempering). The second heat flow curve was then subtracted from the first to give the enthalpy decrease.

Primak (1955) provides a mathematical treatment for tempering, in which the temperature of the sample is raised according to the relation

$$t = c\tau,$$

where $1/c$ is the heating rate. Primak obtains an approximate solution for the construc-

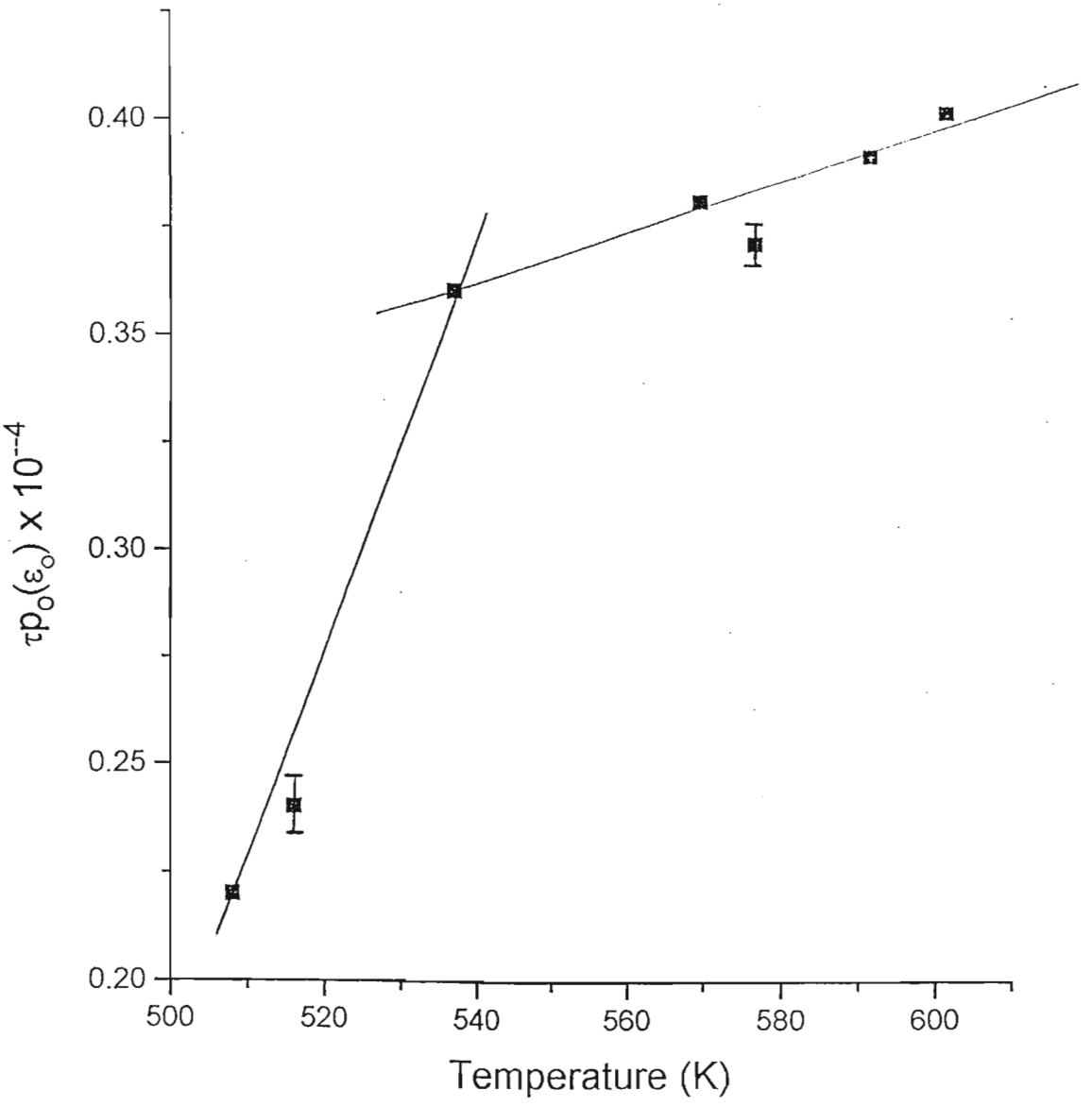

Figure 4.5: $\tau p_o(\epsilon_o)$, inferred from length measurements, vs temperature T.

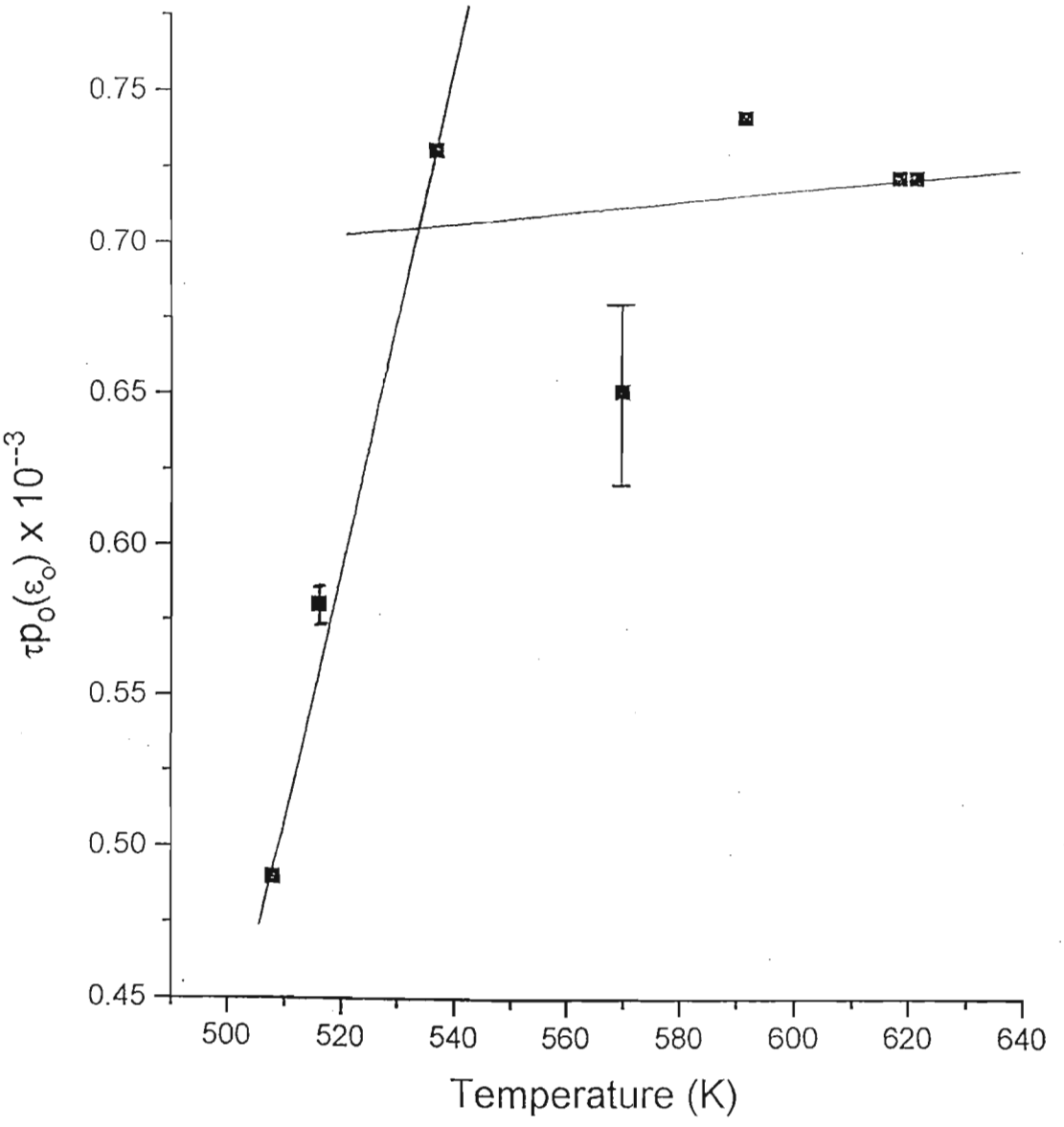

Figure 4.6: $\tau p_o(\epsilon_o)$, inferred from resistivity measurements, vs temperature T.

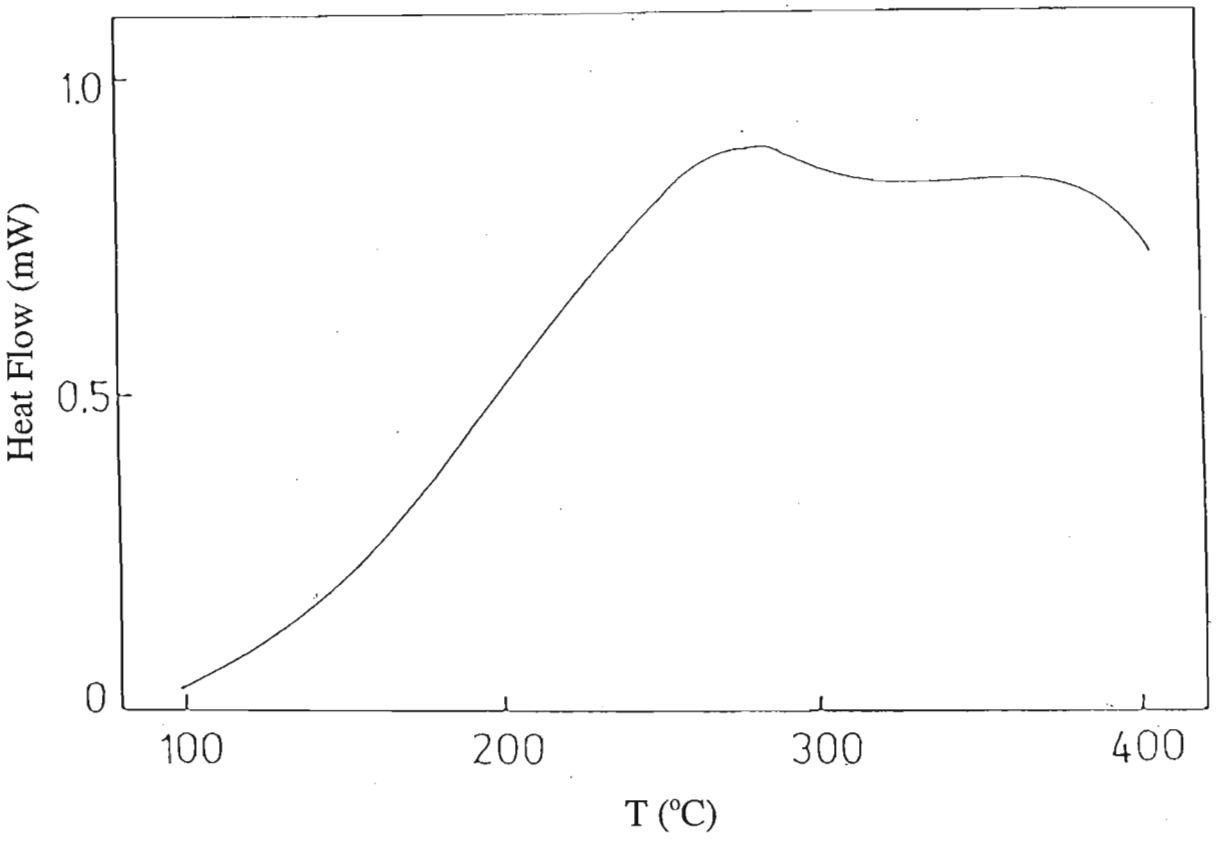

Figure 4.7: Heat flow curve for $Fe_{40}Ni_{40}B_{20}$ (Scott, 1981).

tion of the initial activation energy spectrum, namely

$$p_o(\epsilon_o) = -\frac{d\tau}{d\epsilon_o}.\frac{dP}{d\tau}$$

with

$$\epsilon_o = \tau\left[\ln(\nu c\tau) - \ln\left(\frac{\epsilon_o}{\tau} + 2\right)\right].$$

Since $d\epsilon_o/d\tau$ is slowly varying with temperature, the initial activation energy spectrum may be written as

$$p_o(\epsilon_o) \propto -\frac{dP}{d\tau}, \tag{4.1}$$

provided that the heating rate of the sample is constant.

If we now associate the heat flow in Figure 4.7 with the measured value of the property P in Equation 4.1, then its gradient is proportional to $-p_o(\epsilon_o)$. If we fit Figure 4.7 with two linear curves then, the trend observed would be approximately consistent with a bi-valued $p_o(\epsilon_o)$ over the same range of temperatures that were investigated in the present work. Scott (1981), however, does not propose any formal explanation for the observed behaviour. This behaviour will be discussed next, in terms of the intrinsic diffusion mechanisms responsible for structural relaxation in such systems.

4.3.2 Relaxation Processes that Determine $p_o(\epsilon_o)$

It has been established above, that $p_o(\epsilon_o)$ assumes two different approximately constant values over the range of temperatures investigated. Using Equation 2.13 for ϵ_o, the activation energy for which a breakdown in $\ln(t)$ kinetics is observed at low T-low t corresponds to approximately 1.5 eV. Also the activation energy at which $p_o(\epsilon_o)$ changes its value is approximately 1.8 eV. The range of activation energies scanned during isothermal annealing can, therefore, be subdivided into three regimes, namely below 1.5 eV, between 1.5 and 1.8 eV, and above 1.8 eV, respectively.

Now, structural relaxation can be considered as a stress relief mechanism in which p_s-n_s stress defects recombine and, therefore, it is worth pointing out some of the understanding that can be gained from studies of mechanical properties (stress dependent) in respect of $p_o(\epsilon_o)$. In particular, the following points are worth noting:

1. Annealing-induced embrittlement is composition dependent. Iron based glasses, especially with large metalloid additions, embrittle very easily (Luborsky and Walter, 1976).

2. Annealing-induced embrittlement correlates well with structural relaxation (Kimura and Ast, 1980).

Chi *et al* (1978) have investigated the influence of quench rate on the kinetics of embrittlement in $Fe_{40}Ni_{40}N_{20}$ and attempt to explain this behaviour from the viewpoint of structural relaxation. They suggest that the glass becomes brittle when it attains a critical atomic configuration. Now $Fe_{40}Ni_{40}B_{20}$ alloys show qualitatively the same relaxation modes as do $Fe_{40}Ni_{40}P_{14}B_6$ alloys (Kronmuller and Moser, 1983). This suggests a common origin for structural relaxation in the two alloys and, therefore, also possibly for the mechanics of fracture. Shown in Figure 4.8 is the surface bend strain at fracture E_f, of amorphous $Fe_{40}Ni_{40}P_{14}B_6$, as a function of annealing temperature (Kimura and Ast, 1980). The annealing induced embrittlement shows two well defined stages when surface strain at fracture is taken as a fracture parameter. With reference to Figure 4.8, in Stage I, fracture follows plastic flow and in Stage II, fracture occurs before the onset of plastic flow. Shown in Figure 4.9 (Kimura and Ast, 1980) is the decay of the total enthalpy of Region I, where Region I is shown in Figure 4.8, obtained from the DSC curve of $Fe_{40}Ni_{40}P_{14}B_6$. Also shown in Figure 4.9 is the decay of the microfracture strain σ_f. Thus, structural relaxation of $Fe_{40}Ni_{40}P_{14}B_6$, when monitored in terms of the irreversible enthalpy of relaxation, results in two activation energies for relaxation, namely, 0.94 eV

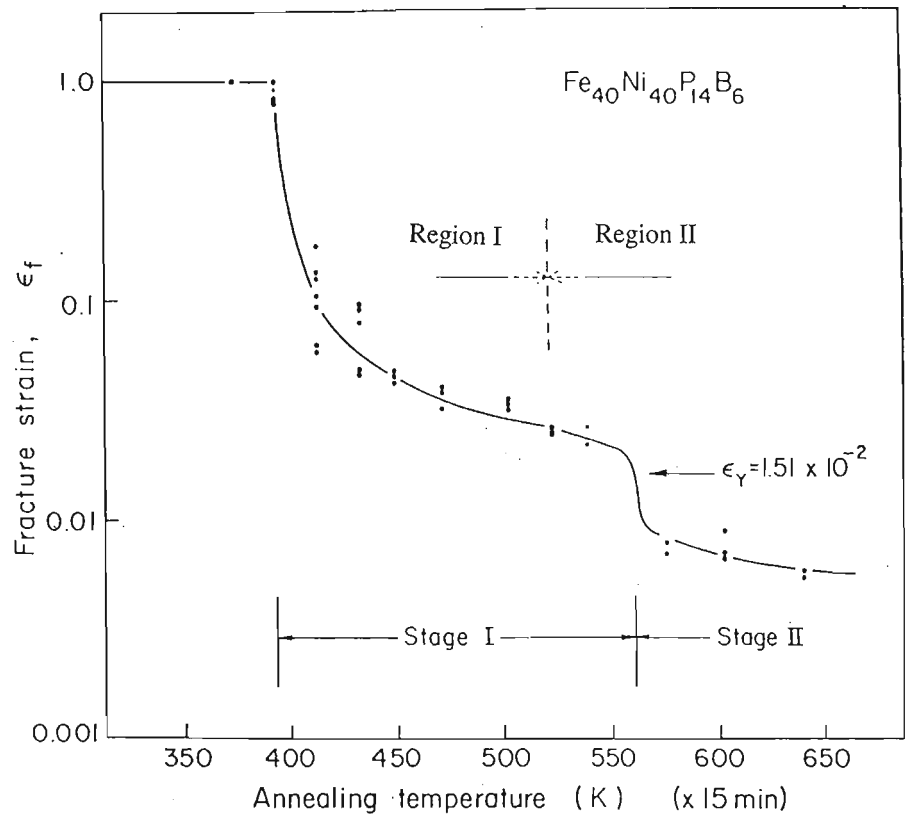

Figure 4.8: Relation of surface bend strain at fracture E_f, of amorphous $Fe_{40}Ni_{40}P_{14}B_6$, to the annealing temperature (Kimura and Ast, 1980).

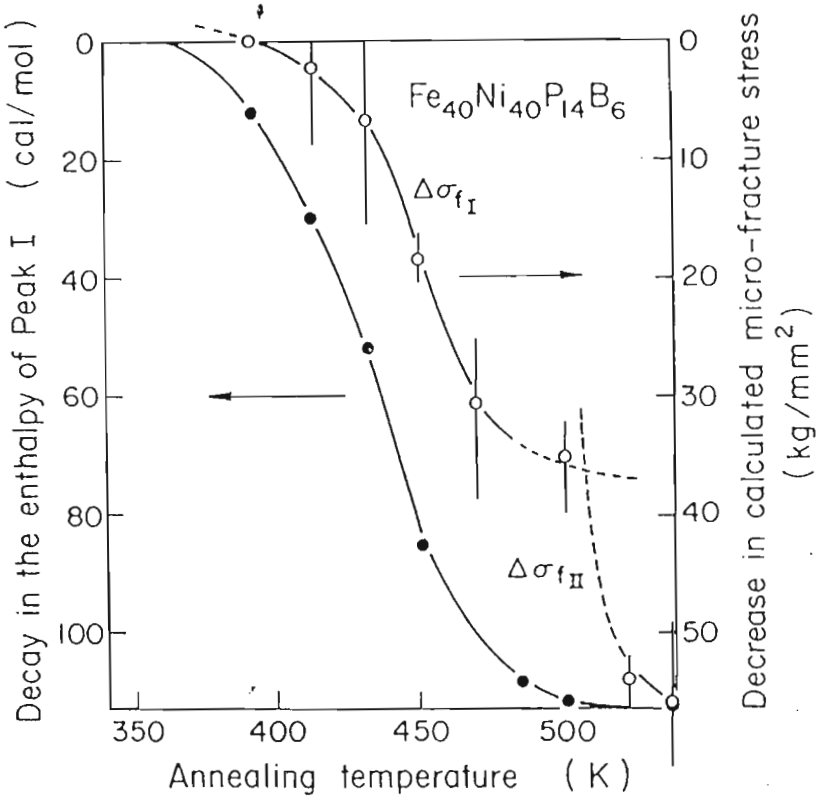

Figure 4.9: Decay of the total enthalpy in Region I and decay of the local microstructure strain in Stage I, for $Fe_{40}Ni_{40}P_{14}B_6$ (Kimura and Ast, 1980).

associated with Region I and 1.8 eV associated with Region II, where Regions I and II are shown in Figure 4.8.

Shown in Figure 4.10 are plots for the annealing time, required to reach various fracture strains in $Fe_{40}Ni_{40}P_{16}B_6$, as a function of $1/T$. The activation energies obtained are 0.94 eV for embrittlement in Stage I and 2.47 eV for Stage II. The activation energy of 0.94 eV for Stage I correlates well with that obtained for structural relaxation of Region I. Hence, structural relaxation of Region I is attributed to the decay of microstructure stresses in Stage I embrittlement. The activation energy of 0.94 eV is relatively low and, therefore, a local ordering process is thought to be responsible for the embrittlement of Stage I and hence, for structural relaxation of Region I.

The value of 2.47 eV for Stage II, deduced from embrittlement, is somewhat higher than the value of 1.8 eV for Region II. Stage II is assumed to be complicated by irreversible changes upon heating and reversible short range order changes during thermal cycling. Chi *et al* (1978) demonstrate the influence of the quenching rate on the kinetics of embrittlement in amorphous $Fe_{40}Ni_{40}B_{20}$ alloys, and find two activation energies of 0.9 eV for low quench rates and 2.6 eV for high quench rates. Taking into account the two stage behaviour in fracture mechanics of bending, one may suggest that $Fe_{40}Ni_{40}B_{20}$ produced by low quench rates exhibit a two stage behaviour (Stage I and II), while those produced by high quench rates exhibit a one stage behaviour (Stage II only). The two activation energies obtained by Chi *et al* (1978), therefore, correspond to those of structural relaxation of Regions I and II respectively and hence can be associated to the observed trend of the initial activation energy spectrum $p_o(\epsilon_o)$, as noted in our work.

Ascasibar and Hernando (1985) report a similar trend in the magnetization behaviour of $Fe_{40}Ni_{40}P_{14}B_6$. They note that during the relaxation process the initial activation energy spectrum $p_o(\epsilon_o)$, as inferred from changes in magnetization energy, varies over the entire energy range swept (1.44 - 2.05 eV). The variation in $p_o(\epsilon_o)$ was obtained

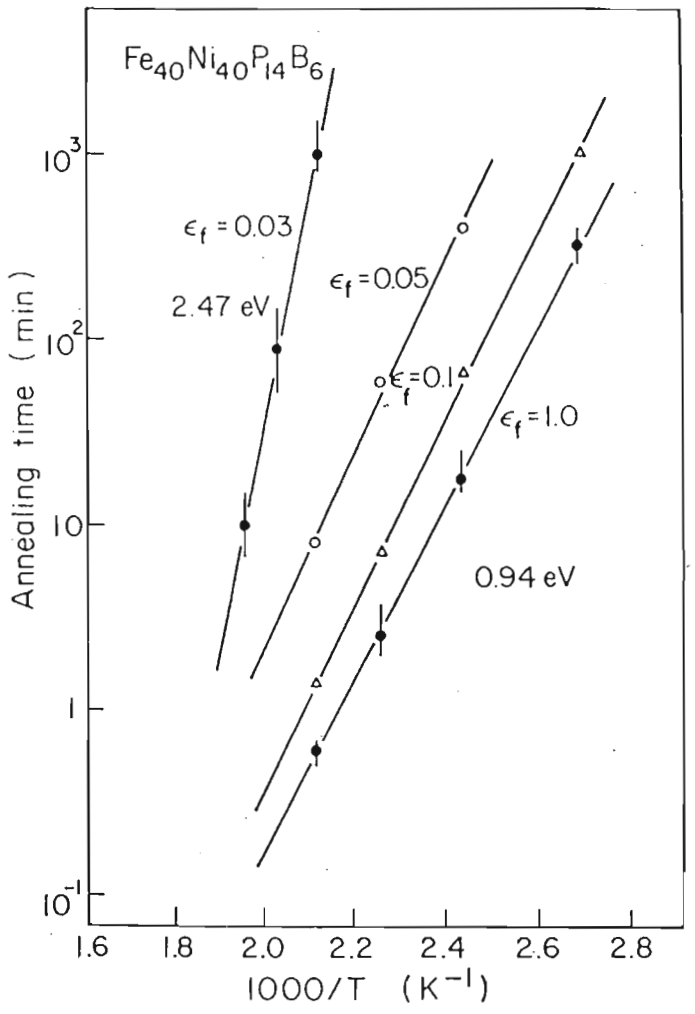

Figure 4.10: Plots of the annealing times, required to reach various fracture strains in $Fe_{40}Ni_{40}P_{14}B_6$, as a function of $1/T$ (Kimura and Ast, 1980).

by dividing the energy range into smaller intervals so that $p_o(\epsilon_o)$ can be considered constant over each of these regions. A profile of $p_o(\epsilon_o)$ as a function of energy, as shown in Figure 4.11, was obtained and used to explain the non-observation of $\ln(t)$ kinetics as indicated by the changes in magnetization energy. The shape of the curve, in Figure 4.11, has a change of slope at approximately 1.85 eV indicating a boundary between two different types of relaxation processes. It is noted that at lower energies the activated processes contribute to magnetic softening of the material by reducing the domain boundary pinning, and thus lowering the energy necessary to magnetize it. Ascasibar and Hernando (1985) conclude that the energy range between 1.4 and 1.85 eV correspond to atom diffusive motion, and that two sub-intervals can be distinguished within this range, namely

1. that for lower energies up to approximately 1.6 eV, corresponding to metalloid atom motion, with the higher mobility due to the smaller size, and

2. between 1.6 and 1.85 eV, diffusion is dominated by the movement of Fe and Ni atoms.

It is also asserted that energies exceeding 1.85 eV activate another type of process which the authors cannot account for.

It is interesting to note that the partitioning of the energy range by Ascasibar and Hernando (1985) is in good agreement with our results. We, however, relate the initial processes, with activation energies below approximately 1.5 eV, to diffusion of the Fe and Ni atoms by means of an indirect vacancy-mediated mechanism, in which vacancies (voids) serve as mobile diffusion vehicles. Also, with progressive annealing the excess free volume decreases and the activation energy for processes correspondingly increases. As the excess free volume contracts during relaxation, diffusion of the larger metallic atoms is reduced due to a decrease in the size of the diffusion vehicles (free volume).

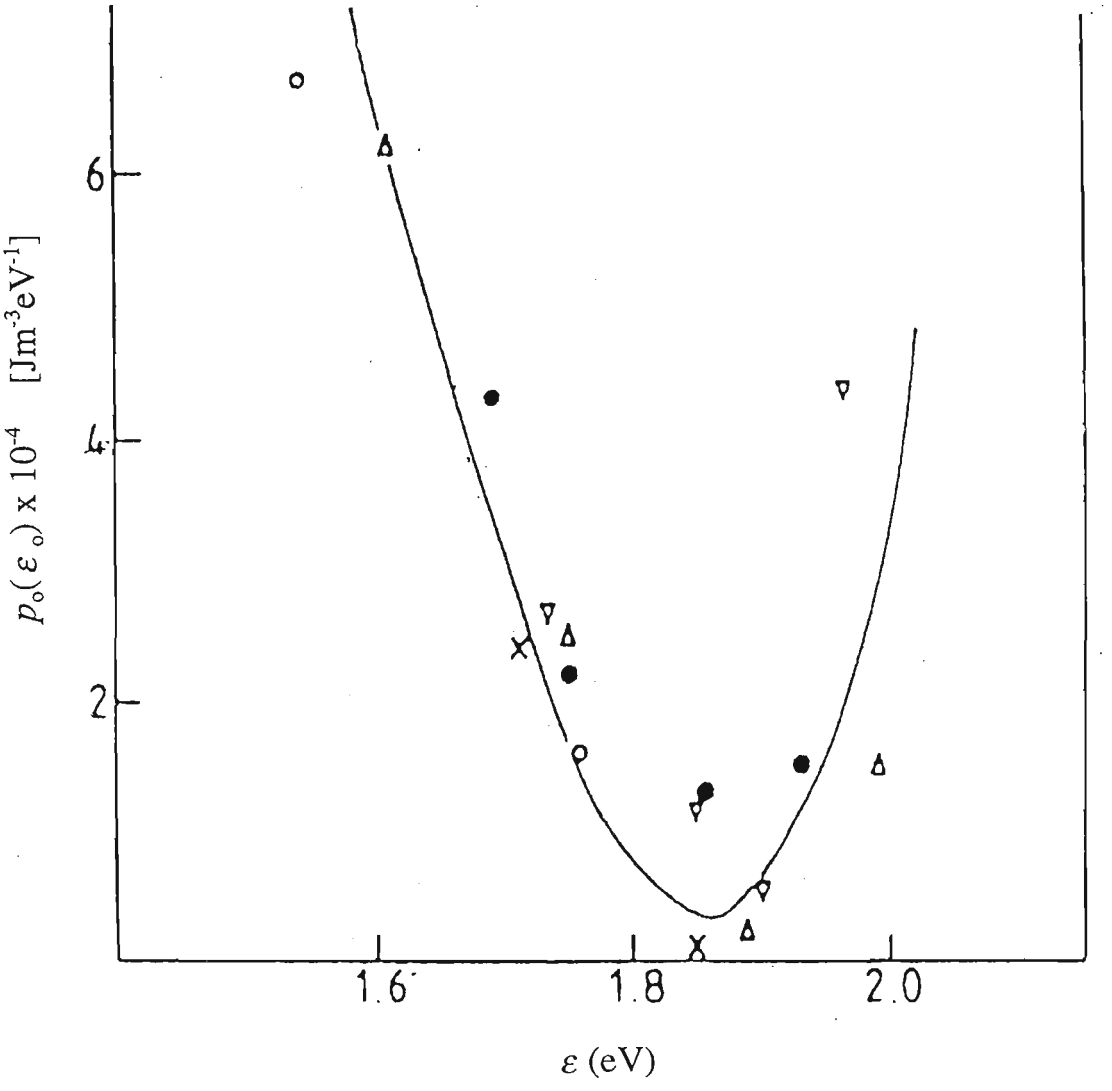

Figure 4.11: A profile of $p_o(\epsilon_o)$ vs ϵ (Ascasibar and Hernando, 1985).

We relate processes with activation energies between approximately 1.5 and 1.8 eV, to the directional reordering of nearest neighbour atom pair axes. Evidence for reordering of the atom pairs is provided by the magnetic after effects (MAE) observed in ferromagnetic amorphous alloys (Kronmuller and Moser, 1983). The presence of MAE has been demonstrated in a number of alloys (see, for example, Fujimori *et al* (1978), Alia *et al* (1980), and Moser and Kronmuller (1980)). An interesting aspect of MAE measurements is their relation to the diffusion properties of amorphous alloys as related to the microstructural reordering of atom pairs (Kronmuller and Moser, 1983). In a crystalline binary (AB) alloy it is well established that magnetic annealing induces an anisotropy energy due to alignment of magnetic atom pairs parallel to the spontaneous magnetization. In amorphous alloys, containing two transition metals (A and B), atom pairs of type AA, BB and AB exist. Egami and Flanders (1976), reporting on stress relaxation measurements, predict similar pairing in $Fe_{40}Ni_{40}B_{20}$. They relate the relaxation mechanism with reorientation of the axes of nearest neighbour pairs of metal atoms (Fe-Fe, Ni-Ni, Fe-Ni), which takes place in the vicinity of a free volume.

In general the atom pairs are considered to be mobile. As indicated in Figure 4.12 (Kronmuller and Moser, 1983), a small rearrangement of the free volume results in a reorientation of the axes of neighbouring pairs of metal atoms. It is assumed that each atom pair may occupy two energetically different orientations, i.e. $\mathbf{P_1}$ or $\mathbf{P_2}$. In each orientation the energy of interaction of an atom pair with the spontaneous magnetization is different and thus influences the MAE. Shown in Figure 4.13 is a relaxation spectra of the MAE, presented in terms of the fractional change in reluctance r (which is defined as the inverse susceptibility, $1/\chi$), for FeNiB alloys of the form $Fe_{80-x}Ni_xB_{20}$. It is apparent from the figure that the maximum amplitude of the MAE in $Fe_{40}Ni_{40}B_{20}$ occurs near 360 K and goes to zero at about 500 K (Kronmuller and Moser, 1983). The temperature range between 360 and 500 K is roughly in agreement with the range, suggested in the

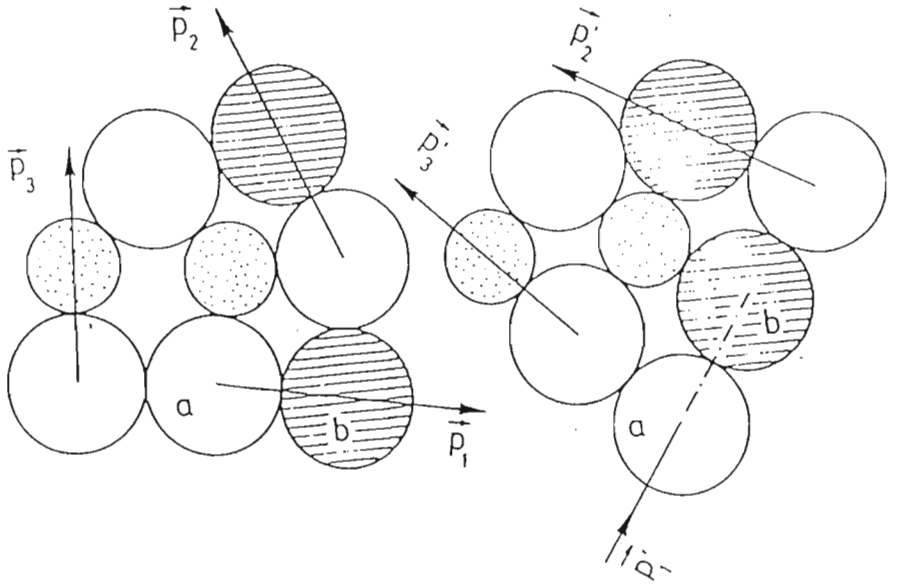

Figure 4.12: Reorientation of pairs of metal atoms in the neighbourhood of a free volume. Big empty circle = iron atoms, big shaded circle = nickel atoms, small circles = metalloid atoms (Kronmuller and Moser, 1983).

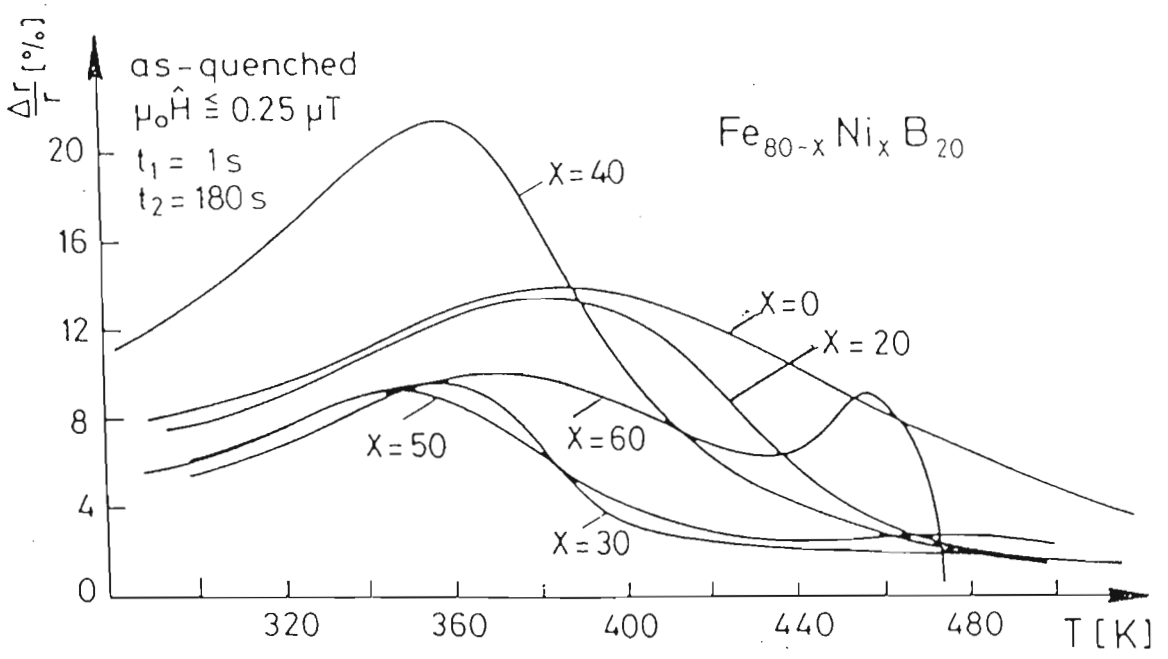

Figure 4.13: MAE relaxation spectra of several $FeNiB$ alloys (Kronmuller and Moser, 1981).

present work, over which pairing of metal atoms is thought to occur.

For processes with activation energies above 1.8 eV, the excess free volume is sufficiently reduced to allow the diffusion of the smaller metalloid atoms only. This interpretation is supported by Koster *et al* (1980), who obtained an activation energy of 1.87 eV for crystallization governed by B diffusion in amorphous $Fe_{40}Ni_{40}B_{20}$. Metalloid atoms, in general, are assumed to occupy centres of a Bernal polyhedra (Bernal, 1960). These positions for the metalloid atoms are considered to be rather stable and to be activated only at higher temperatures. With reference to Figure 4.14, the relaxation process in this region is ascribed to jumps of metalloid atoms (small spheres) to sites 2 and 2' located between neighbouring metal atoms (big spheres), from their usual sites 1 and 1'. The sites 2 and 2' are called 'anomalous' sites (Bernal, 1960). Thus, at elevated temperatures free volume reduction proceeds by diffusion of the metalloid atoms only, via an 'interstitial' type mechanism.

Whence the observed behaviour in the initial activation energy spectrum $p_o(\epsilon_o)$, inferred from the relaxation behaviour of length and resistivity, could be attributed to different relaxation processes that could be classified by

1. diffusion of the larger metallic atoms for low activation energies,

2. pairing of metallic atoms for intermediate activation energies, and

3. diffusion of the smaller metalloid atoms for higher activation energies.

Note that the partitioning of the activation energy range has been roughly inferred from the behaviour of $p_o(\epsilon_o)$, whereas the diffusion mechanisms thought to occur are inferred from the literature. Therefore, the above classification is a generalization and could, in fact, involve cooperative movement of a large number of atoms (Ulfert, 1988).

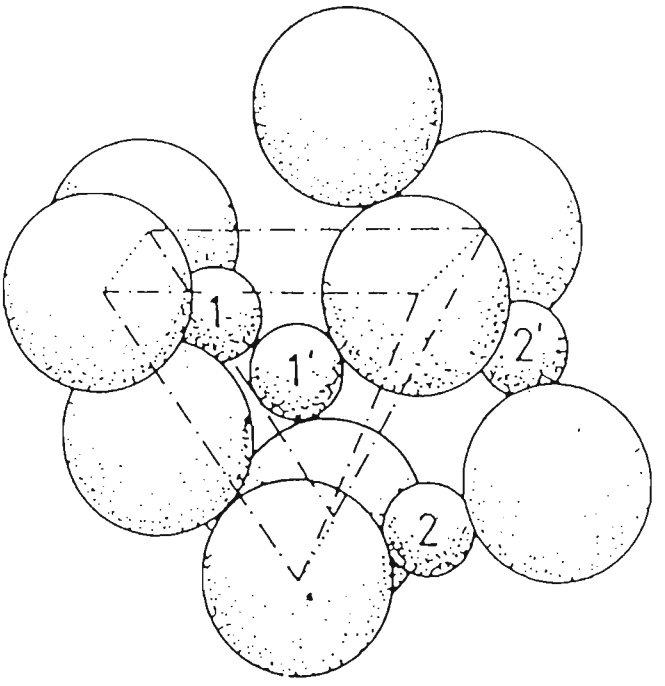

Figure 4.14: Movement of metalloid atoms in a Bernal Polyhedra (Bernal, 1960).

4.4 Use of the 'Relaxation Equation'

In order to apply the 'relaxation equation' (Equation 2.41) to the experimental results of length and resistivity relaxation, estimates for the initial activation energy spectrum $p_o(\epsilon_o)$, and the scaling factors β and c are required. In the present treatment $p_o(\epsilon_o)$ is found to take on two different values over the temperature range investigated. For simplicity, the values of $p_o(\epsilon_o)$, obtained from the slope $-\tau p_o(\epsilon_o)$ of the curves in Figures 4.3 (length) and 4.4 (resistivity), are averaged over the temperature range investigated. Use of the averaged value has little effect on the scaling plots since $p_o(\epsilon_o)$ assumes two approximately constant values over the whole temperature range investigated and is expected (Equation 2.16) to be reasonably constant for isothermal annealing at a particular temperature. The averaged values for $p_o(\epsilon_o)$, obtained independently from length and resistivity measurements, are given in Table 4.1.

Now, both β and c appear in the expression for $\Delta P/P_o$ (Equation 2.41) which is, therefore, not algebraically solvable if both β and c are unknown. An empirical solution is, however, obtained from a plot of $-(\Delta P/P_o(\ln(t) = 0))/\tau$ against temperature T, as shown in Figures 4.15 and 4.16 for length and resistivity respectively. The gradient is then given by $\beta p_o(\epsilon_o)/T_m$ and the ordinate by $p_o(\epsilon_o)[ln(\nu_o) - c]$, where the value of $p_o(\epsilon_o)$ is already known and ν_o is taken to be the Debye frequency, $\sim 10^{13}$ Hz (Chen, 1981a). T_m the melting temperature of $Fe_{40}Ni_{40}B_{20}$ is known to be approximately 1373 K (Vacuumschmelze 0040 specification sheet). Values for β and c, obtained from length and resistivity measurements, are also given in Table 4.1.

It should be noted that both β and c obtained from length and resistivity measurements respectively are, within experimental error, apparently equal. This is expected since the configurational entropy change ΔS, as given in Equation 2.40, is the same for both length and resistivity relaxation. It should be noted, however, that the averaged value of $p_o(\epsilon_o)$, as obtained from length and resistivity, respectively, are distinctly dif-

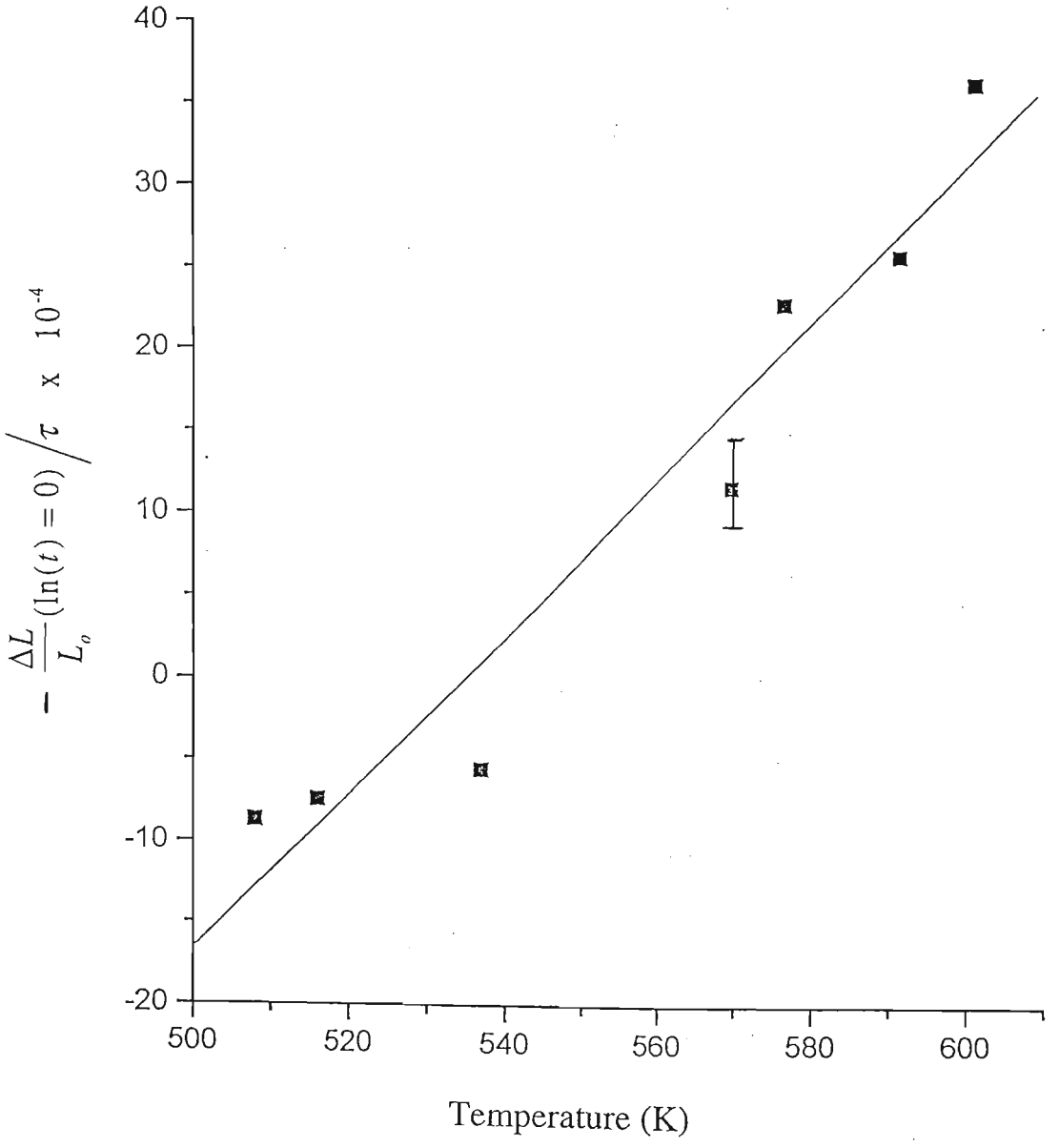

Figure 4.15: $-(\Delta P/P_o(\ln(t) = 0))/\tau$ vs T, inferred from length measurements.

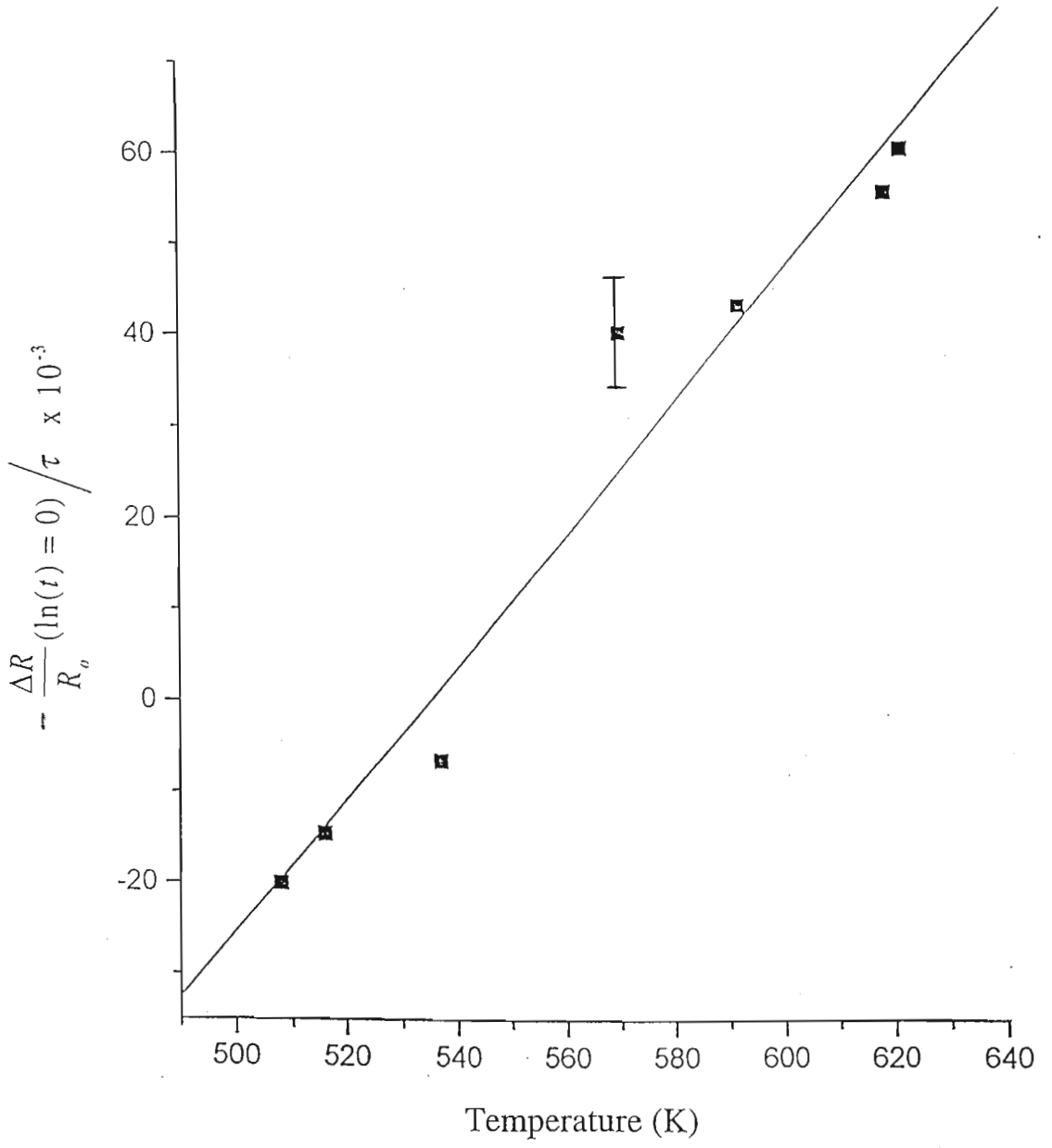

Figure 4.16: $-(\Delta P/P_o(\ln(t) = 0))/\tau$ vs T, inferred from resistivity measurements.

ferent by two orders of magnitude. Since the same initial activation energy spectrum is scanned during the annealing process, one would intuitively expect the same values of $p_o(\epsilon_o)$ in each case. In Section 2.2.4, however, we noted that a property p is proportional to the number of kinetic processes q which can yet occur, i.e. $p = Iq$. The proportionality constant I (termed the importance factor) is expected to be different in each case. Length (density) relaxation is dependent on the annihilation of 'free volume' or more precisely on p_s-n_s defect recombination (which is a second order effect), whereas resistivity relaxation is dependent on the reduction of internal stresses (which is a first order effect). The magnitude of $p_o(\epsilon_o)$, therefore, depends on the relationship between the activated processes and the property change being measured and, moreover, on the state of the material at the start of the experiment.

	Length	Resistivity
$p_o(\epsilon_o)$ $[(\text{eV})^{-1}]$	$6.95\text{x}10^{-4}$	$1.33\text{x}10^{-2}$
β	70 ± 15	81 ± 15
c	57 ± 6	62 ± 3

Table 4.1: Values for $p_o(\epsilon_o)$, β and c inferred from experiment.

Inserting the values of $p_o(\epsilon_o)$, β and c into the 'relaxation equation' (Equation 2.41) yields excellent agreement between theory and experiment, as shown in Figures 4.17 (length) and 4.18 (resistivity) for a few selected times. The gradient of the best fits are 1.15 and 1.06, for length and resistivity respectively, in good agreement with a unit gradient as expected from Equation 2.41. The extended model can, therefore, be used to predict relative quantitative changes in structure sensitive properties during structural relaxation at sub-T_g isothermal annealing temperatures.

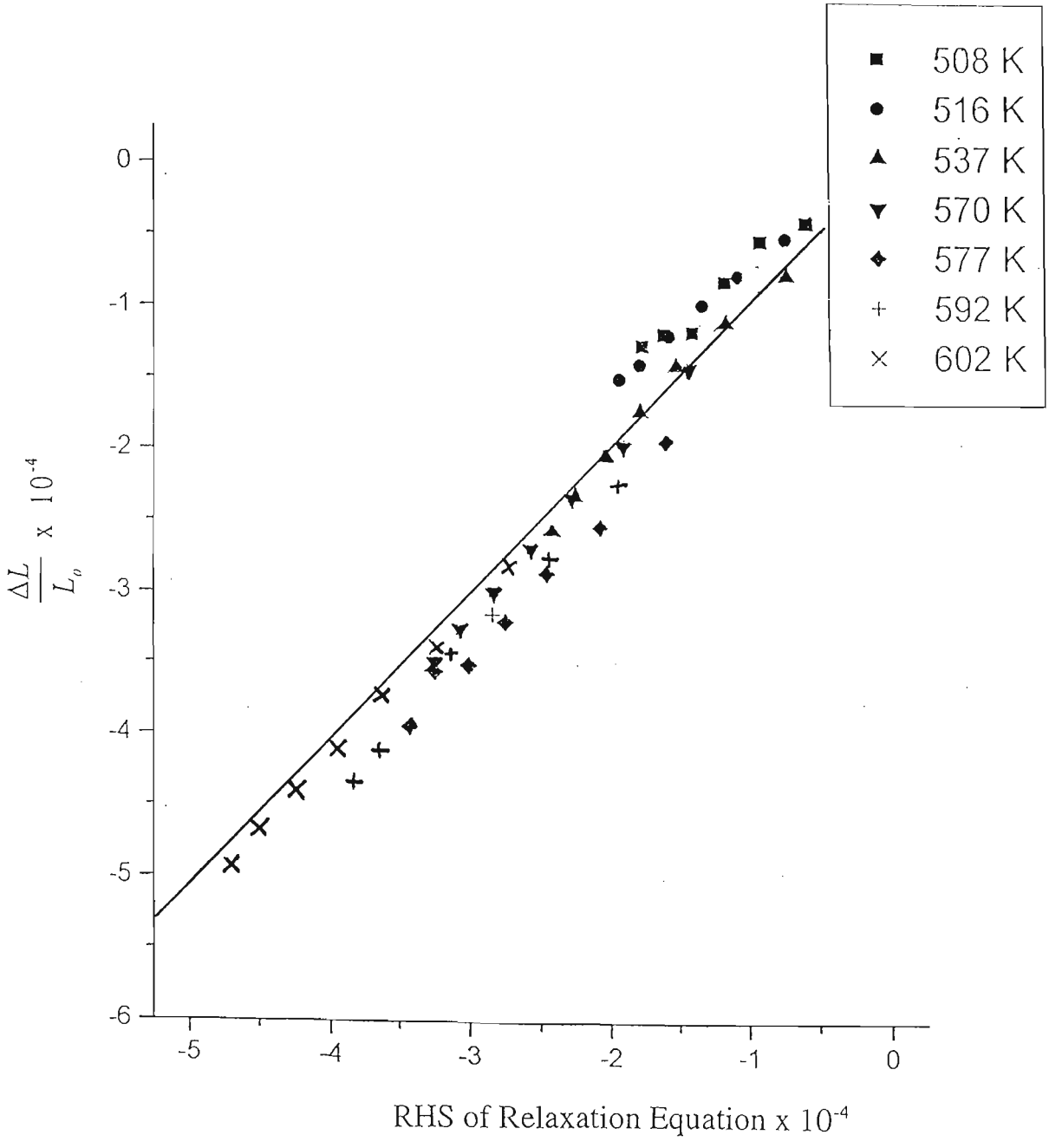

Figure 4.17: Fit for length measurements.

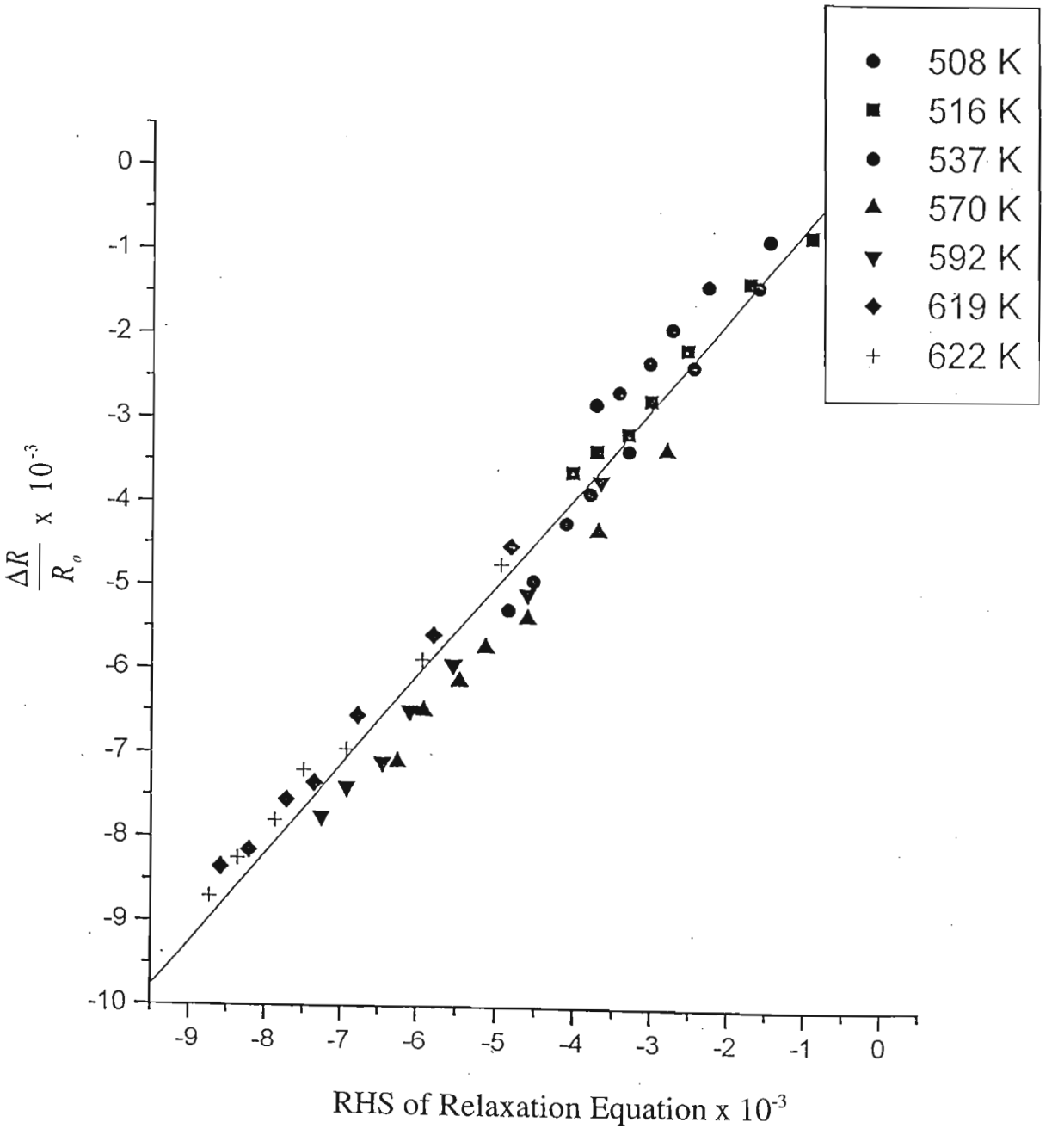

Figure 4.18: Fit for resistivity measurements.

4.5 Some Implications of the 'Relaxation Equation'

4.5.1 Scaling Behaviour

A few interesting implications of the relaxation equation (Equation 2.41) are apparent if we replace the scaling constants β and c by

$$\beta = \beta' ln(\nu_o) \tag{4.2}$$

and

$$c = c' ln(\nu_o). \tag{4.3}$$

Using $\nu_o = 10^{13}$ Hz and the results from Table 4.1 gives $\beta' = 2.35$ and $c' = 1.91$ from length measurements and $\beta' = 2.71$ and $c' = 2.06$ from resistivity measurements. Inserting Equations 4.2 and 4.3 into the relaxation equation (Equation 2.41) gives

$$\frac{\Delta P}{P_o} = -\tau p_o(\epsilon_o) \left[\ln(t) + \ln(\nu_o) \left(1 - c' + \beta' \frac{T}{T_m} \right) \right]. \tag{4.4}$$

Note that the relaxation equation represented in this form reduces to $-p_o(\epsilon_0)\tau \ln(t)$ at some critical temperature T_o, where $T_o = T_m(c'-1)/\beta'$. Inserting values for β' and c' into the expression for T_o yields 537 K and 531 K, for the parameters extracted from length and resistivity measurements, respectively. Note that these values for T_o correspond approximately to 540 K, the temperature at which $p_o(\epsilon_o)$ changes values (see Figures 4.5, 4.6 and 4.7).

Since $\ln(\nu_o)[1 - c' + \beta' T/T_m]$ gives the displacement necessary to fit parts of the activation energy spectrum, revealed at different temperatures, together then for $T_o <$ 540 K and $T_o >$ 540 K the activation energy spectrum will be displaced to lower and higher activation energies, respectively. This displacement is attributed to the different diffusion mechanisms dominating the temperature range above and below $T_o = 540$ K.

We can further rearrange Equation 4.4, by dividing throughout with $\ln(t)$, to obtain

$$\frac{\Delta P}{P_o \ln(t)} = -\tau p_o(\epsilon_o)\left[1 + \frac{\ln(\nu_o)}{\ln(t)}\left(1 - c' + \beta' \frac{T}{T_m}\right)\right]. \tag{4.5}$$

Now, if a plot of $\Delta P/(P_o \ln(t))$ vs T is made, then the curves for different annealing times should all pass through the same point at $T = T_o$. This is indeed approximately observed, as shown in Figures 4.19 and 4.20, for length and resistivity, respectively.

4.5.2 Entropy

The main contribution to the free energy for structural relaxation comes from local changes around the excess free volume, and since this cannot be properly isolated no general conclusion about the sign of the configurational entropy change ΔS is thus possible (Huntington *et al*, 1955). Structural relaxation, however, involves densification as the excess free volume is removed. This process involves correlated short-range ordering effects as the mean atomic distance between neighbouring atoms decrease. At higher annealing temperatures the degree of densification is greater as observed from the larger saturation values of the fractional change in length, as shown in Figure 4.1. The entropy change, as noted in Equation 2.40, is therefore expected to be temperature dependent.

The linear curves obtained in Figures 4.15 and 4.16 can be taken as a formal confirmation of the linear temperature dependence of ΔS if (see Equation 2.41)

$$-\frac{\Delta P/P_o(\ln(t) = 0)}{\tau} = p_o(\epsilon_o)[\ln(\nu_o) + \beta T/T_m - c]$$

holds over the range of temperatures investigated. Now insertion of the averaged values of $\beta = 76$ and $c = 60$ (from Table 4.1) into the formal expression for the entropy change (Equation 2.40) result in negative values for ΔS over the whole temperature range investigated. Zener (1951a) associates a negative entropy change to short-circuiting paths for diffusion and also discusses various possible types of such paths. Thus, in inhomogeneous systems there are percolation paths along which diffusion occurs more readily

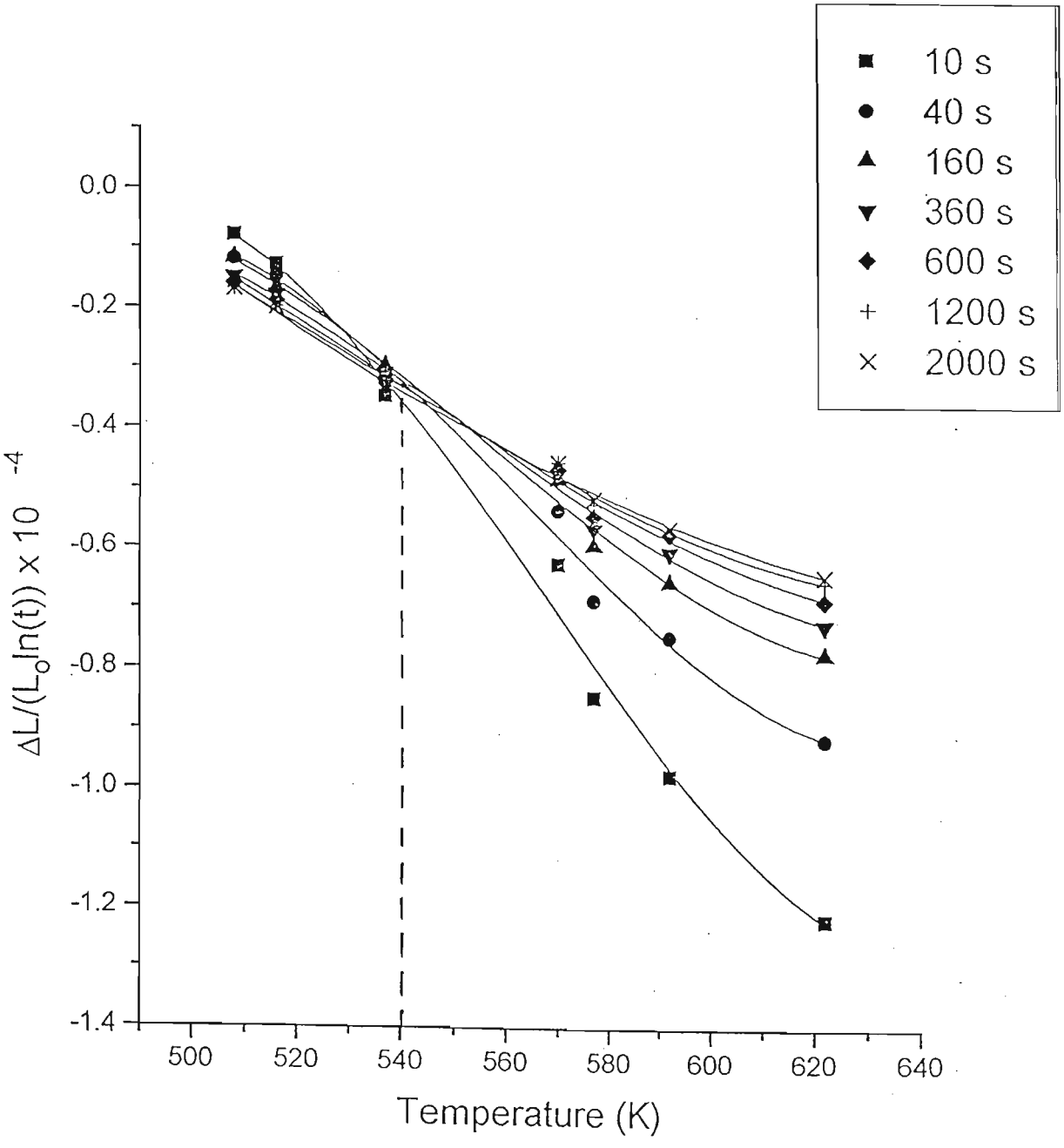

Figure 4.19: $\Delta L/(L_o \ln(t))$ vs T.

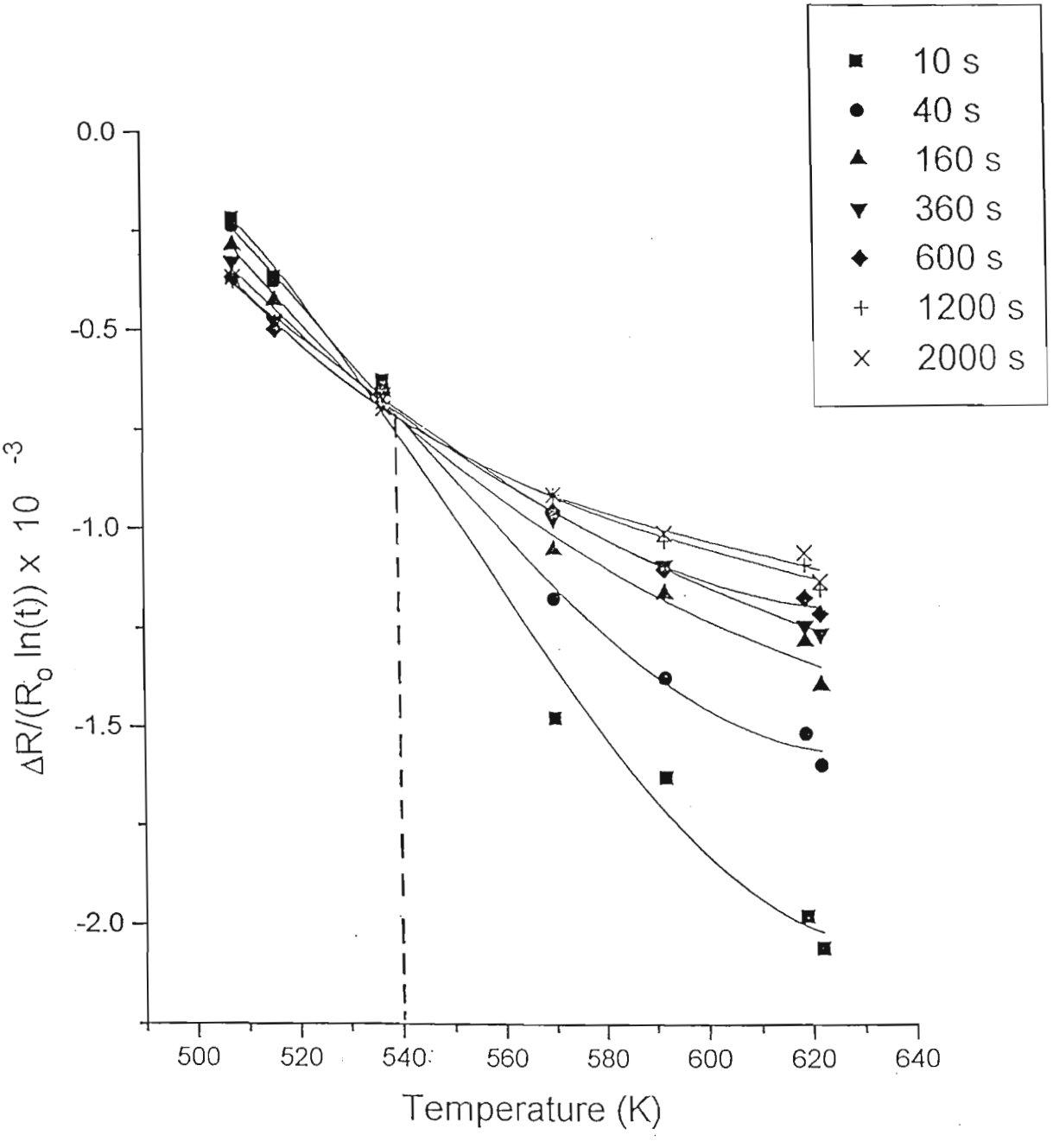

Figure 4.20: $\Delta R/(R_o \ln(t))$ vs T.

than in homogeneous systems. This is due to a lower activation energy for diffusion and, therefore, a lower corresponding bulk measured value for the diffusion constant. These percolation paths can be provided by, for example, grain boundaries which have been found to promote rapid diffusion of thorium in tungsten (Fonda *et al* (1933) and Langmuir *et al* (1934)), and dislocations which have also been found to accelerate diffusion (Matanno, 1934). Pound *et al* (1961) find large negative values for the entropy of activation in chromium and uranium, and attribute this to a ring diffusion mechanism. A large negative contribution to the entropy change is expected, for ring diffusion, from the requirement that the vibration of atoms in the ring be properly coordinated. It is also possible in amorphous alloys that large negative entropies be associated with vacancy migration if the local relaxation around a free volume is sufficiently large. If diffusion occurs predominantly along these short-circuiting paths then ΔS can be negative.

Kronmuller and Frank (1989), reporting on Fe tracer diffusion mechanisms in amorphous $Fe_{91}Zr_9$, relate a reduced diffusion coefficient to a negative tracer migration entropy. They propose that diffusional jumps of the Fe tracer atoms, in a loosely packed $Fe_{91}Zr_9$ structure, become possible when, as a result of thermal fluctuations, the spread-out free volume contracts next to the tracer atoms. This enables the tracer atoms to jump into the vacant space of the size of about one atomic volume. The contraction of free volume corresponds to a negative migration entropy (Kronmuller *et al*, 1991). This phenomenon is easily extended to self-diffusion mechanisms of the constituent components in amorphous alloy systems. It should be noted that in an amorphous structure, free volume 'vacancies' can dissappear not only at conventional sites, such as the specimen surface, but also internally in regions in which the local density exceeds its average value (Frank *et al*, 1996).

In the present treatment negative ΔS result from the condition $c > \beta T/T_m$ (see Equation 2.40). The idea of short-circuit diffusion is ruled out by the fact that during

relaxation, at a fixed temperature, the excess free volume anneals out simultaneously with a decrease of the diffusivities in all metallic glasses investigated. The increase in activation energy from 1.5 eV through more than 1.8 eV is due to the fact that the vacancies gradually agglomerate. A negative entropy is interpreted in terms of a low availability of vacant neighbouring sites, where the vacant sites have to be produced by contraction of the spread-out free volume as a result of thermal fluctuation.

4.5.3 Free Volume Annihilation

There has been considerable difficulty, in the literature, in understanding the mechanisms involved in free volume annihilation. There are two possible mechanisms, namely the excess volume n_s may migrate through the amorphous matrix until it disappears by redistribution or by annihilation with compressive defects p_s. It is expected that the p_s and n_s defects are distributed in size, and hence in activation energy, as discussed in Section 2.2.3. At lower activation energies the larger defects are predominantly annihilated before the smaller defects. The concentration of defects can be inferred by observing a physical property change ΔP which depends, in a known way, on a particular defect concentration. The simplest interpretation is to assume that defects, treated as points, migrate through the amorphous lattice until they reach a 'sink' where they can disappear completely. The observed change in ΔP is then due solely to the removal of these defects, and the number of defects which are removed in unit time dt is then $d\Delta P/dt$. The mean time $< t >$ which an individual defect requires to find a sink is then $d\Delta P/(d\Delta P/dt)$ and from Equation 2.41 this is given by

$$< t >= t_A \left[\ln(t_A) + \ln(\nu_o) + \frac{\beta T}{T_m} - c \right], \tag{4.6}$$

where t_A is the annealing time at temperature T. Consider now the process of annihilation of excess free volume at a number of randomly distributed sinks (sites) in the

amorphous system. Since the motion of each n_s defect is a 'random walk' process, and the defects and sinks are initially randomly distributed, the average number of jumps made by a defect before disappearing will scale as the reciprocal of the concentration of sinks. If, for arguement, the free volume annihilation process were to proceed via expulsion through the surface of the ribbon, i.e. through an infinite number of sinks, then free volume annihilation would be independent of the concentration of sinks. The mean number of jumps will, therefore, be constant throughout relaxation so that $< t >$ should be approximately constant. But this is not physically correct since $< t >$ evolves with both annealing temperature and time as expressed in Equation 4.6. The situation is formally similar to the disappearance of the excess free volume at a number of sinks, but the concentration of sinks now decrease as relaxation proceeds. This interpretation is physically appealing since the mean number of jumps made by a defect before it disappears is expected to increase, as the excess free volume is annihilated, due to a reduction in the number of available sinks. Thus, $< t >$ should be dependent on annealing time as noted in Equation 4.6. The temperature dependence in Equation 4.6 is expected since at higher temperatures, defects effectively sample more sites due to the increased thermal motion. Therefore, the degree of free volume annihilation will be enhanced at higher temperatures leading to larger saturation levels, as noted in Figures 4.1 and 4.2.

Chapter 5

Other Related Effects

5.1 The Glass Transition Temperature

The phenomenon of the glass transition is complex, and no single theory has been capable of accounting for all aspects of it (Elliot, 1984). The glass transition, as observed experimentally, also shows a relaxation behaviour. In particular, very different results are obtained if the glass transition is probed calorimetrically (differential scanning calorimetry or differential thermal analysis), where the experimental time scale is of the order of seconds, than, for example, when ultrasonic relaxation spectroscopy experiments (such as dielectric loss measurements) is employed, where the time scale is much smaller.

A theory which relates relaxation kinetics with entropy considerations has been proposed by Adams and Gibbs (1965). These authors account for mass transport by considering cooperative atomic rearrangements. By finding the smallest size of a molecular group capable of rearrangement at a given temperature, they show that the group size and, therefore, the probability of rearrangement and hence the viscosity η can be

expressed as a function of the configurational entropy ΔS by

$$\eta = \eta_o \exp\left(\frac{B}{T\Delta S}\right),$$

where B is a constant. Substituting from Equation 2.40, for the configurational entropy ΔS, into the above equation, yields

$$\begin{aligned} \eta &= \eta_o \exp\left(\frac{B}{T(\beta k T/T_m - c_s)}\right) \\ &= \eta_o \exp\left(\frac{B'}{T(T - cT_m/\beta)}\right) \end{aligned} \tag{5.1}$$

where $B' = BT_m/\beta k$ and $c = c_s/k$. The form of this equation resembles that of the Vogel-Taumann-Fulcher equation (Equation 1.11) with the exception of an additional temperature term appearing in the denominator. Also, the Vogel-Taumann-Fulcher equation has a singularity at some temperature T_o, which is defined as the ideal glass transition temperature. Hence, the singularity in equation 5.1 is defined as

$$T_g = cT_m/\beta. \tag{5.2}$$

Inserting the values for the scaling parameters β and c given in Table 4.1 into Equation 5.2, one obtains values for the glass transition temperatures of $T_g = 900 \pm 400$ °C (from length relaxation) and $T_g = 800 \pm 200$ °C (from resistivity relaxation). These calculated values for T_g are, within experimental error, in rough agreement with the accepted value of $T_g \sim 700$ °C for $Fe_{40}Ni_{40}B_{20}$ (Vacuumschmelze 0040 specification sheet).

It should be noted, however, that the Vogel-Taumann-Fulcher equation is an empirical law and, in particular, the temperature dependence is rather unusual in that it cannot be obtained by an appropriate averaging of the energy in an Arrhenius expression or by a suitable temperature dependence of the energy.

The total configurational entropy ΔS is related to the heat capacity by

$$\Delta S = \int_{\ln(T_o)}^{\ln(T)} \Delta C_p d\ln(T).$$

For the case where ΔC_p is small, as it is for SiO_2 and GeO_2, ΔS is almost independent of temperature and the viscosity η should obey an Arrhenius equation of the Vogel-Taumann-Fulcher form (Elliot, 1984). On the other hand when ΔC_p is large, ΔS contributes a temperature dependent term to the equation for viscosity, leading to a strongly non-Arrhenius behaviour, as observed in many organic and ionic glasses. These trends, i.e. both Arrhenius and non-Arrhenius behaviour, are shown in Figure 1.4 (from Wong and Angell, 1976). Since the configurational entropy change ΔS (Equation 2.40) is temperature dependent, a non-Arrhenius behaviour in the viscosity should be expected. The derived equation for viscosity (Equation 5.2) should, therefore, be more appropriate for metallic glass systems.

5.2 Diffusion

Taub and Spaepen (1980) attempted to evaluate diffusion coefficients from viscosity data. They find that in Pd-Si alloys the measured diffusivity of Au atoms in the as-quenched glass is larger, by several orders of magnitude, than the diffusivity calculated from viscosity data for the relaxed state. The diffusivity decreases to the relaxed state value if the glass is allowed to relax by annealing at some sub-T_g temperature. This suggests that frozen-in defects in metallic glasses, which are present in the as-quenched state, play an important role in diffusion.

Processes such as structural relaxation, phase separation, and crystallization involve significant rearrangements in the atomic structure and, therefore, cause significant changes in structure sensitive properties. These processes are controlled by diffusion of atoms through the structure of the amorphous alloy. In general, investigation of diffusion in amorphous alloys is difficult for two primary reasons (Ulfert *et al*, 1989):

1. The diffusivities decrease considerably during the course of annealing, and

2. Since at high temperatures amorphous alloys tend to crystallize, diffusion can be measured over small distances in reasonable experimental times only.

Ulfert *et al* (1989) overcame these problems with the use of tracer atoms. In conjunction with the large volume of data available on diffusion in metallic glasses, three diffusion mechanisms, namely, vacancy, interstitial and cooperative diffusion, are suggested. Vacancy migration is the most common mechanism for self diffusion and impurity diffusion in crystalline alloys (Christian, 1965). However, the usual definition of a vacancy is meaningless in an amorphous structure where it can only be defined as a region of lower than average density of atomic dimensions in the alloy structure. A vacancy in an amorphous structure is not characterized by the absence of an atom but rather as large 'interstitial' sites.

Several investigations of the structure and size of 'interstitial' sites in soft dense random packed models have been considered (see, for example, Finney and Wallace, 1981). It is understood that the size of 'interstitial' sites cannot be very different from the size of a vacancy in a crystal lattice and that migration of larger interstitial sites are a possible diffusion mechanism analogous to vacancy migration in a crystalline lattice.

Several investigators, for example, Valenta *et al* (1981) and Chen *et al* (1978), have suggested that diffusion in amorphous alloys can take place by cooperative motion of a group of adjacent atoms. Cooperative motion can only initiate atomic diffusion if some redistribution of 'interstitial' sites occur and, conversely, the migration of 'interstitial' sites require cooperative motion of the surrounding atoms. Interstitial migration may take place either by direct interchange of position between large and small 'interstitial' sites, or by decomposition of a large 'interstitial' site into several smaller ones. This interpretation is consistent with free volume reduction by p_s-n_s defect recombination, where p_s and n_s are associated with the small and large 'interstitial' sites respectively.

In crystalline alloys, small atoms are dissolved into interstitial sites within the lat-

tice. Diffusion then proceeds by an interstitial mechanism, with the small atoms moving between adjacent interstitial sites (Shewman, 1963). A similar interstitial diffusion mechanism is also possible in an amorphous alloy, with small solute atoms migrating through the interstitial sites of an amorphous matrix.

Shown in Figure 5.1 is the normalized Arrhenius graph of measured diffusion coefficients in metal-metalloid amorphous alloys, with a different line for each of the diffusing species (Cantor and Cahn, 1983). Note that at a given fraction of T_g the diffusion coefficients depend only upon the nature of the diffusing species, and increase progressively from the larger atoms such as Pd and Au through to the smaller atoms such as Li. This suggest a progressive change in the diffusing species, within the ternary amorphous $Fe_{40}Ni_{40}B_{20}$ system, from the large Fe, Ni atoms to the light B atoms. This view is further supported by Kijek *et al* (1980) who suggest a progressive change in the diffusing species, from cooperative atomic motion and interstitial site migration for large atoms, to an interstitial diffusion mechanism for small atoms. This progressive change in diffusing species from the larger to the smaller atoms is consistent with our interpretation of the different relaxation mechanisms, considered in Section 4.3 of the present study.

5.3 Crystallization

To gain an understanding of crystallization in an amorphous alloy, a hypothetical diagram of the free energy for various possible phases versus atomic concentration is found to be useful. Such a diagram for an amorphous Fe-B alloy system, with stable α-Fe and Fe_2B phases, metastable Fe_3B phase and the amorphous phase, is shown in Figure 5.2 (after Koster and Weiss, 1975). The stable equilibrium phases are indicated by solid tangents and the metastable phases by dashed tangents. The reaction paths from the amorphous phase to the various stable and metastable phases are numerically marked in brackets.

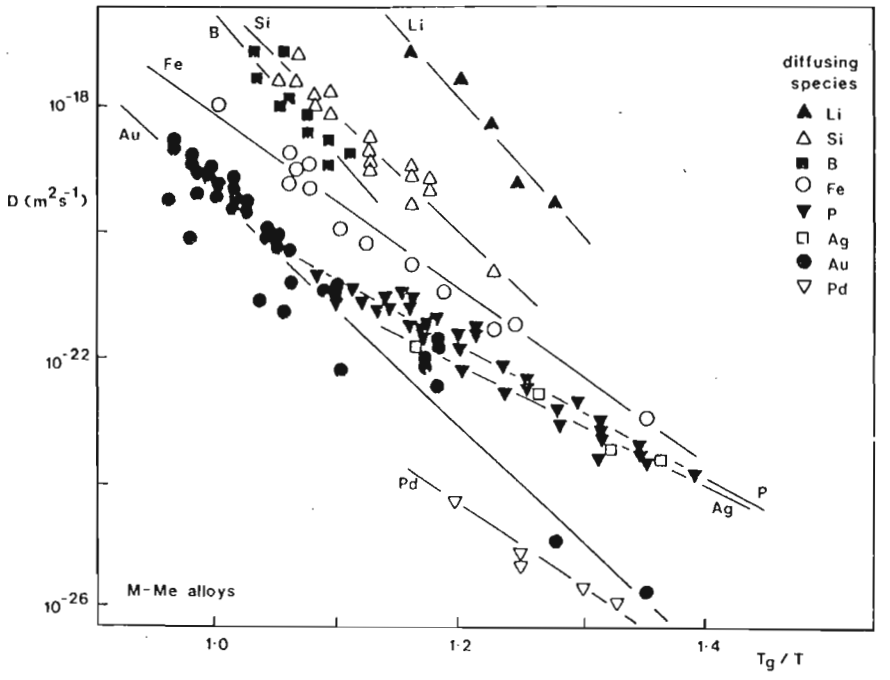

Figure 5.1: Normalised Arrhenius graph of measured diffusion coefficients in metal-metalloid amorphous alloys (Cantor and Cahn, 1983).

Depending on concentration, the transition from the metastable amorphous phase into the crystalline phase can proceed by one of the following reactions (Herold and Koster, 1978):

1. Polymorphous Crystallization of an amorphous alloy into a supersaturated crystalline alloy. This reaction can only occur in regions near the pure elements or compounds. These reactions should be possible in the Iron rich range (reaction (1)) or near the composition Fe_3B (reaction (4)).

2. Primary Crystallization into one of the stable phases, for example, α-Fe (reaction (2)). During this reaction the amorphous phase will be enriched in B until further crystallization is stopped by reaching the stable α-Fe and amorphous Fe-B phases. The dispersed primary crystallized phase may act as preferred nucleation sites for crystallization of the remaining amorphous matrix.

3. Eutectic Crystallization into two crystalline phases by a discontinuous reaction (reaction (3) or reaction (5)). These reactions have the largest driving force and can occur anywhere between the two stable α-Fe and Fe_2B phases.

All Fe-B metallic glasses crystallize by one of the above mechanisms. The dominant reaction is determined by the thermodynamic driving force and the activation barrier for each reaction. In most cases, equilibrium phases do not form directly from the glass, but proceed by way of one or several metastable phase/s, for example, in the Fe-B system the stable phases are α-Fe and Fe_2B yet the glass always crystallize to the metastable Fe_3B phase with the stable phases forming only at higher temperatures. Stability against crystallization is determined by the nucleation and growth process. In all Fe-B-X ternary alloys, activation energies for eutectic and polymorphous crystallization are much higher than in binary alloys. This indicates a simultaneous transfer of a group of atoms indicative of cooperative processes. In general, eutectic and polymorphous

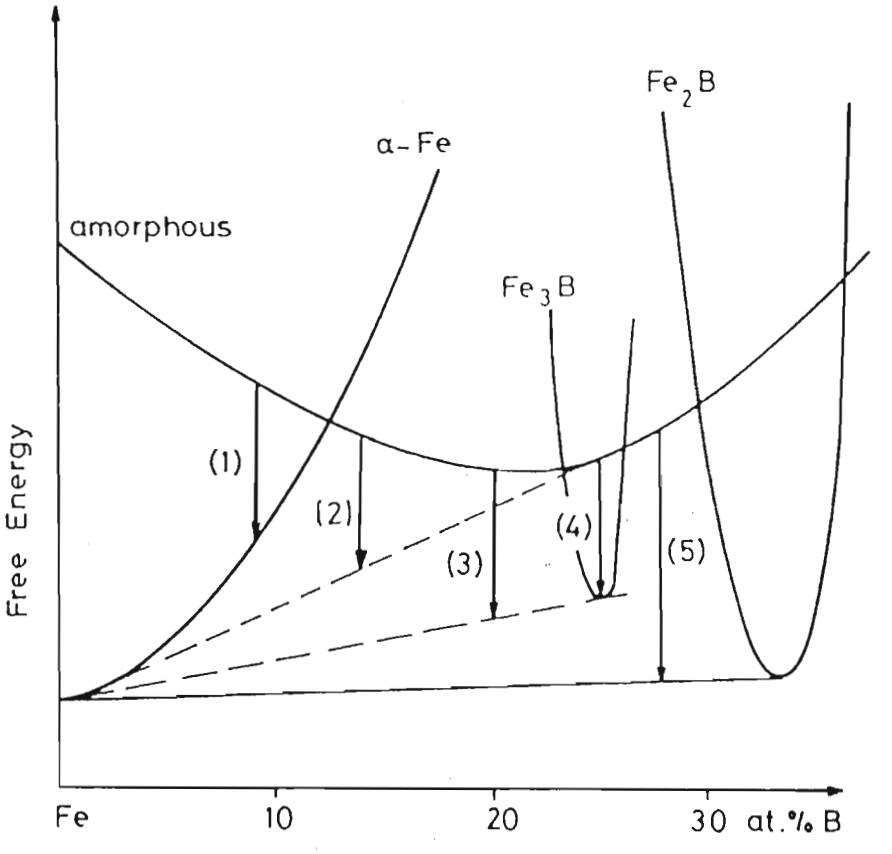

Figure 5.2: A hypothetical diagram of the free energy for various phases versus B concentration (Koster and Weiss, 1975).

crystallization is found to be retarded in ternary alloys (Koster and Weiss, 1975), for example, in $Fe_{40}Ni_{40}B_{20}$. Primary crystallization, however, is stabilized by the metalloid atoms in ternary metal-metalloid alloys due to a larger diffusion coefficient of the metalloid species. The observation of small scale phase separation in as-cast $Fe_{40}Ni_{40}B_{20}$ which leads to the formation of regions, about 4 μm in size, with the stoichiometric composition of $(FeNi)_3B$ (Piller and Haasen, 1982) suggests a primary crystallization process. This process is supported by the present work, where B diffusion is predicted to be the dominant process during the latter stages of structural relaxation.

Chapter 6

Conclusion

Numerous models have been formulated to explain various relaxation phenomena in amorphous metallic alloys. No single model, however, has been successful in accounting for all aspects of structural relaxation, i.e. the glass transition, crystallization, $\ln(t)$ behaviour, crossover and reversibility effects. The most general models that include the kinetics of processes which are distributed in activation energy, successfully predict the experimentally observed $\ln(t)$ behaviour. All previously published treatments based on these models do not, however, adequately allow for a distribution of effective attempt frequencies ν and for a varying initial activation energy spectrum $p_o(\epsilon_o)$. Earlier models generally assume ν and $p_o(\epsilon_o)$ to be constant over the range of temperatures for which $\ln(t)$ kinetics is observed.

In the present work, the above problems are addressed by considering the entropy change ΔS. The functional form of ΔS (Equation 2.40) is obtained by considering the elastic distortion of neighbouring atoms, necessary for a 'configurational jump', during the relaxation process. Inclusion of the entropy change ΔS, by replacement of the activation energy ϵ with the Gibbs free energy of activation ΔG, via the effective attempt frequency ν, results in an expression for structural relaxation (Equation 2.41). This

equation is found to yield good agreement for the relaxation behaviour of both length and resistivity in ribbon specimens of amorphous $Fe_{40}Ni_{40}B_{20}$.

The entropy change ΔS predicted by the present treatment, over the whole temperature range investigated, is found to be negative. A negative entropy is interpreted in terms of a low availability of vacant neighbouring sites. The vacant sites have to be produced by contraction of the spread-out free volume as a result of thermal fluctuation. The quenched-in excess free volume results in stress defects p_s (compressive stress), n_s (dilative stress) and τ_s (shear stress). It is shown that the τ_s defect concentration is significantly reduced by relaxation during the glass formation process and, therefore, do not contribute significantly to structural relaxation during sub-T_g super-ambient annealing procedures. It is concluded that free volume annihilation proceeds by mutual recombination of the compressive p_s and dilative n_s stresses.

Also investigated is the structure of the initial activation energy spectrum $p_o(\epsilon_o)$, which reveals three sub-intervals, namely; below 1.5 eV, between 1.5 and 1.8 eV, and above 1.8 eV respectively. These sub-intervals are shown to be governed by the atomic processes accompanying structural relaxation in the glassy state. These atomic processes are intrinsically associated with consecutive diffusion of the metallic and metalloid atoms respectively. We predict that the initial relaxation (i.e. for processes with activation energies below 1.5 eV), involving regions with a relatively large excess free volume, proceeds via diffusion of the larger metallic Fe and Ni atoms. When the excess free volume is further reduced (i.e. for processes with activation energies between 1.5 and 1.8 eV), a directional reordering of the nearest neighbour metallic atom pair axes takes place. Thereafter, the reduced excess free volume allows only for diffusion of the smaller metalloid atoms via an interstitial type mechanism.

Moreover, various implications of the relaxation equation are considered and good agreement with the experimental data is noted. Firstly, we show (in Section 4.5) that

the relaxation equation reduces to $-p_o(\epsilon_o)\tau\ln(t)$ at a critical temperature T_o, where $T_o = T_m(c\ln(\nu_o) - 1)/\beta\ln(\nu_o)$. Insertion of the relevant parameters into the expression for T_o yield the approximate temperature at which $p_o(\epsilon_o)$ changes value. Secondly, by dividing the relaxation equation (Equation 2.41) with $\ln(t)$, it is noted that curves for different annealing times should all pass through the same point at $T = T_o$. This is indeed approximately observed.

The predictions inferred from the relaxation equation, or aspects of it, is also applied and/or compared to the phenomena of the glass transition, diffusion and crystallization. Following a discussion by Gibbs and Di Marsio (1958), in which the glass transition is defined as that temperature at which the entropy difference ΔS between the liquid and crystalline phases vanish, we obtain, by equating the entropy change ΔS (Equation 2.40) to zero, an expression for the glass transition temperature T_g (Equation 5.2). Insertion of the relevant parameters into Equation 5.2 yield values (calculated independently for the parameters derived from length and resistivity relaxation respectively) for T_g in reasonable agreement with the expected value of $T_g \sim 700$ °C for the $Fe_{40}Ni_{40}B_{20}$ amorphous alloy. We also derive, by considering the viscosity as a function of the configurational entropy change ΔS, a non-Arrhenius expression for the viscosity (Equation 5.1). This expression for the viscosity should be more appropriate for amorphous metallic alloys.

$Fe_{40}Ni_{40}B_{20}$ is shown to crystallize via a primary reaction, in which the amorphous phase is enriched with B. Evidence for this process is the observation of small scale phase separation in $Fe_{40}Ni_{40}B_{20}$, with the stoichiometric composition of $(FeNi)_3B$ (Piller and Haasen, 1980). Primary crystallization in $Fe_{40}Ni_{40}B_{20}$ is governed by diffusion of the metalloid B atoms, due to the larger diffusion coefficient. This process is further supported by the model proposed in this work, which predicts that the smaller B atoms are the last species to diffuse.

Diffusion coefficients in metal-metalloid amorphous alloys are shown to depend on the nature of the diffusing species, and increases progressively from the larger metallic atoms through to the smaller metalloid atoms, which is consistent with the predictions in the present work. Hence, the relaxation equation, although developed to describe the $\ln(t)$ kinetics, can be used to account for other related phenomena. This shows a consistency in our approach in the development of the 'present' theory.

Finally, the relaxation equation has introduced two new parameters, namely; β and c. These parameters depend intrinsically on the sample parameters and, therefore, can be used for the characterization of an alloy. In fact, values for β and c can be obtained, for a particular alloy system, from the glass transition temperature T_g, the melting temperature T_m and a plot of the heat flow spectrum, if these are obtainable. By fitting the heat flow spectrum with two linear curves, the temperature T_o at which a change in slope occurs could be estimated. By noting both T_o and the glass transition temperature T_g, values for β and c can be obtained by simultaneously solving for the analytical expressions of T_o (see Section 4,5) and T_g (Equation 5.2).

As an extension to this work the Magnetic After Effects (MAE) can also be investigated under the theoretical approach developed here. Since these effects predominantly involve nearest neighbour atomic pairing, direct comparison with relaxation processes inferred from this work will be possible. The analysis given here should also be tested against other alloy systems.

7 References

1. Adam G and Gibbs J H, J. Chem. Phys., 43, 139, (1965).

2. Allia P, Mazzetti P and Vinai F, J. Magnetism Magn. Mater., 19, 281, (1980).

3. Argon A S and Kuo H Y, J. Non-cryst. Solids, 37, 241, (1980).

4. Asami K and Hashimoto K, Corrosion Sci., 19, 1007, (1979).

5. Ascasibar E and Hernando A, J. Phys. (British Inst. Phys.), d, 141, (1985).

6. Balanzat M, Scripta Met., 14, 173, (1980).

7. Balanzat E and Hillairet J, J. Phys. F., 12, 2907, (1982).

8. Barker J A, Hoare M R and Finney J L, Nature, 257, 120, (1975).

9. Barker J A, J. de Physique, 38(C2), 37, (1977).

10. Batschinski A J, Z. Phys. Chem., 84, 644, (1913).

11. Bennett C H, Chaudhari P, Moruzzi V and Steinhardt P, Philos. Mag., 40, 485, (1979).

12. Bernal J D, Nature, 185, 68, (1960).

13. Berry B S and Pritchet W C, J. Appl. Phys., 44, 3122, (1973).

14. Berry B S and Pritchet W C, AIP Conf. Proc., 34, 292,(1976).

15. Beuche F, J. Chem Phys., 30, 748, (1959).

16. Bhatia A B and Thornton D E, Phys. Rev., B2, 3004, (1970).

17. Boesch L, Napolitano A and Macedo P B, J. Amer. Ceram. Soc., 53, 148, (1970).

18. Brenner A, 'Electrodeposition of Alloys', Academic Press, New York, (1963).

19. Brenner A, Couch D E and Williams E K, J. Res. Natn. Bur. Stand., 44, 109, (1950).

20. Cahn R W, Contemp. Phys., 21, 43, (1980).

21. Cantor B and Cahn R W, 'Amorphous Metallic Alloys', ed. Luborsky F E, Butterworths, 494, (1983)

22. Cargill G S, J. Appl. Phys., 41, 12, (1970).

23. Cargill G S, Solid State Phys., 30, 227, (1975).

24. Chambron W and Chamberod A, Solid St. Commun., 33, 157, (1980).

25. Chaudhari P, Giessen B C and Turnbull D, Scient. Am., 98, (April 1980).

26. Chaudhari P, Spaepen F and Steinhardt P J, 'Glassy Metals II', ed. Beck H and Guntherodt H J, Springer-Verlag, Ch 5, (1983).

27. Chen H S, Scripta. Met., 11, 367, (1977).

28. Chen H S, J. Appl. Phys., 49, 462, (1978).

29. Chen H S, Re. Prog. Phys., 43, 353, (1980).

30. Chen H S, J. Appl. Phys, 52(3), 1860, (1981a).

31. Chen H S, J. Non-Cryst. Solids, 46, 289, (1981b).

32. Chen H S, 'Amorphous Metallic Alloys', ed. Luborsky F E, Butterworths, 180, (1983).

33. Chen H S and Coleman E, Appl. Phys. Lett., 28, 245, (1976).

34. Chen H S and Inoue A, J. Non-cryst. Solids, 61, 805, (1984).

35. Chen H S, Sherwood R C, Leamy H J and Gyorgy E M, IEEE Trans. Magn., MAG-12, 933, (1976).

36. Chi G C and Cargill G S, Mater. Sci. Engng., 23, 155, (1976).

37. Chi G C, Chen H S and Miller C E, J. Appl. Phys., 49, 1715, (1978).

38. Christian J W, 'The theory of transformations in metals and alloys', Pergamon Press, (1965).

39. Cohen M H and Grest G S, Phys. Rev., B20, 1077, (1979).

40. Cohen M H and Turnbull D, J. Chem. Phys., 31, 1164, (1959).

41. Cohen M H and Turnbull D, Nature, 203, 964, (1964).

42. Cohen M H and Turnbull D, ibid., 52, 3038, (1970).

43. Goldstein M, J. Chem. Phys. 51, 3728, (1969).

44. Cost J R and Stanley J T, Scripta. Metall., 15, 407, (1981).

45. Cost J R and Stanley J T, J. of Non-Cryst. Sol., 61, 799, (1984).

46. Cowley J M, J. Appl. Phys., 21, 24, (1950).

47. Curie M, Trans. Faraday Soc., 35, 114, (1930).

48. Davies H A, J. Non-Cryst. Solids, 17, 266, (1975).

49. Davies H A, 'Amorphous Metallic Alloys', ed. Luborsky F E, Butterworths, 17, (1983).

50. Davies H A, Aucote J and Hull J B. Scripta Met., 8, 1179, (1974).

51. Davies H A and Lewis B G, Scripta Met., 9, 1107, (1975).

52. Davis L A, 'Metallic Glasses', Metal Parks, Ohio: Amer. Soc. Metals, 190, (1978).

53. Dienes G J, J. Appl. Phys., 21, 1189, (1950).

54. Dixmier J, Doi K and Guinier A, 'Physics of Non-Crystalline Solids', North Holland, 67, (1965).

55. Doolittle A K, J. Appl. Phys., 22, 1471, (1951).

56. Doyle T B, unpublished.

57. Drijver J W, Mulder A L and Radelaar S, Proc. 4th Int. Conf. on Rapidly Quenched metals, Sendai, (1981).

58. Duwez P, 'Progress in Solid State Chemistry', Pergamon Press, vol 3, 377, (1966).

59. Duwez P, Trans. Am. Soc. Metals, 60, 607, (1967).

60. Duwez P and Lin S C H, J. Appl. Phys., 38, 4096, (1967).

61. Egami T, J. Mater. Sci., 13, 258, (1978).

62. Egami T, 'Amorphous Metallic Alloys', ed. Luborsky F E, Butterworths, 109, (1983).

63. Egami T and Flanders P J, IEEE Trans. Magn., MAG-II, 220, (1976).

64. Egami T, Flanders P J and Graham C D Jr., AIP Conf. Proc., 24, 697, (1975).

65. Egami T and Ichikawa T, Mater. Sci. Engng., 32, 293, (1978).

66. Egami T, Maeda K and Vitek V, Phil. Mag., A41, 883, (1980).

67. Egami T, Ann. N.Y. Acad. Sci., 371, 238, (1981).

68. Egami T and Srolovitz D, J. Phys. F., 12, 2141, (1982).

69. Elliot S R, 'Physics of Amorphous Materials', Longman, Ch 2, (1984).

70. Finney J L, Proc. Roy. Soc., A319, 479, (1970).

71. Finney J L and Wallace J, J. Non-Cryst. Sol.,43, 165, (1981).

72. Finney J L, 'Amorphous Metallic Alloys', ed. Luborsky F E, Butterworths, 42, (1983).

73. Fonda, Young and Walker, Physics, 4, 1, (1933).

74. Fox T G and Flory P J, J. Polym. Sci., 14, 315, (1954).

75. Frank F C, Proc. Roy. Soc., A215, 143, (1952).

76. Frank W, Hamlescher U, Kronmuller H, Scarwaechter P and Schuler T, Physica Scripta, T66, 201, (1996).

77. Fujimori S, Ohta S, Masumoto T and Nakamoto K, Proc. 3rd Int. Conf. on Rapidly Quenched Metals, Vol 2, 232, (1978).

78. Gibbs J H, 'Modern Aspects of the Vitreous State', ed. Mckenzie J D, ch7, (1960).

79. Gibbs J H and Di Marzio E A, J. Chem. Phys., 28, 273, (1958).

80. Gibbs M R J and Evetts J E, Proc. 4th int. conf. on Rapidly Solidified Metals, Sendai, 479, (1981).

81. Gibbs M R J, Evetts J E, Leake J A, J. Mater. Sci., 18, 278, (1983).

82. Giessen B C and Wagner C N J, 'Liquid Metals', Marcel Dekker, 633, (1972).

83. Girt E, Tomic P, Kursomovic A and Mikhaekusanovic T, J. Phys., 41, 875, (1980).

84. Girt E, Tomic P, Kursumovic A and Lord A E Jr, Acta. Metall., 29, 1309, (1981).

85. Goldstein M, J. Chem. Phys., 51, 3728, (1969).

86. Graham C D and Egami T, Ann. Rev. Mat. Sci., 8, 423, (1978).

87. Grange R A and Keifer J M, Trans. Am. Soc. Metals, 29, 85, (1941).

88. Greer A L and Leake J A, J. Non-Cryst. Sol., 33, 291, (1979).

89. Greer A L and Spaepen F, Ann. New York Acad. Sci., 371, 218, (1981).

90. Gubanov A I, Fizika, 2, 502, (1960).

91. Gyorgy E M, Leamy H J, Sherwood R C and Chen H S, AIP Conf. Proc., 29, 198, (1976).

92. Halperin B I and Nielson D R, Phys. Rev. Lett., 41, 121, (1978).

93. Herold U and Koster U, Proc. 3rd Int. Conf. on Rapidly Quenched Metals, ed. Cantor B, Vol 2, 1, (1978).

94. Hoare M R and Pal P, J. Cryst. Growth, 17, 77, (1972).

95. Hoare M R and Pal P, Adv. Phys., 24, 646, (1975).

96. Honig J M, J. Chem. Phys., 22, 1689, (1954).

97. Huang S C and Fiedler H C, Mater. Sci. Engng., 51, 39, (1981).

98. Huntington H B, Shirin G A and Wajda E S, Phys. Rev., 99, 1085, (1955).

99. Jones H, 'Glass', Meuthuen, (1956).

100. Jones H, Rep. Prog. Phys., 36, 1425, (1973).

101. Kauzmann W, Chem. Rev., 43, 219, (1948).

102. Kijek M, Ahmadzadeh M and Cantor B, Proc. Int. Conf. on Amorphous Metals, Budapest, (1980).

103. Kimura H and Ast D G, Proc. 4th Int. Conf. on Rapidly Quenched Metals, Sendai, 457, (1980).]item Kimura H and Masumoto T, 'Amorphous Metallic Alloys', ed. Luborsky F E, Butterworths, Ch 12, (1983).

104. Klemen M and Sadoc J F, J. Phys. Lett., 40, L569, (1979).

105. Koster U, Herold U, Hillenbrand H G and Denis J, J. Mater. Sci., 15, 2155, (1980).

106. Koster U and Weiss P, J. Non-Crsyt. Sol., 17, 359, (1975).

107. Kramer J, Annin Phys., 19, 37, (1934)

108. Kronmuller H and Frank W, Rad. Def. and Def. in Sol., 108, 81, (1989).

109. Kronmuller H and Moser N, 'Amorphous Metallic Alloys', ed. Luborsky F E, Butterworths, 341, (1983).

110. Kronmuller, Frank W and Horner A, Materials Science and Engineering, A133, 410, (1991)

111. Kuhlmann D, Z. Physik, 124, 468, (1948).

112. Kursomovic A, Cahn R W and Scott M G, Scripta. Met., 14, 1245, (1980).

113. Kursomovic A and Scott M G, Appl. Phys. Lett., 37, 620, (1980).

114. Langmuir I, J. Franklin Inst., 217, 543, (1934).

115. Leake J A, Gibbs M R J, Vryenhoef S and Evetts J E, J. of Non-Cryst. Sol., 61, 787, (1984).

116. Lieberman H H, J. Mater. Sci., 15, 2771, (1980).

117. Luborsky F E, 'Amorphous Metallic Alloys', ed. Luborsky F E, Butterworths, 4, (1983).

118. Luborsky F E, American Institute of Physics Conf. Proc., 29, 209, (1976)

119. Luborsky F E, 'Ferromagnetic Materials', North-Holland Publishing Company, New York, vol 1, 451, (1980).

120. Luborsky F E, Becker J J and McCary R O, IEEE Trans. Magn., MAG-11, 1644, (1975).

121. Luborsky F E and Lieberman H H, Mater. Sci. Engng., 49, 257, (1981).

122. Luborsky F E and Walter J L, J Appl. Phys., 47, 3648, (1976).

123. Mader S and Nowick A S, J. Vac. Sci and Technol., 2, 35, (1965).

124. Majewska I, Thijsse B J and Radelaar S, Proc. 4th Int. Conf. on Rapidly Quenched Metals, Sendai, 1173, (1981).

125. Marcus M A, Acta. Met., 27, 879, (1979).

126. Masumoto T, Hashimoto K and Naka M, Proc. 3rd Int. Conf. on Rapidly Quenched Metals, Vol 2, 435, (1978).

127. Masumoto T and Suzuki K, Japan Institute of Metals, Sendai, Vol I, 371, (1982).

128. Matanno C, Jap. J. Phys., 9, 41, (1934).

129. Mizoguchi T, Kudo T, IrisawaT, Watanabe N, Nimura N, Misawa M and Suzuki K, Proc. 3rd Int. Conf. on Rapidly Quenched Metals, Ed. B Cantor, Vol 2, 384, (1978).

130. Mizoguchi T, Kato H, Akutsu N and Hatta S, Proc. 4th Int. Conf. on Rapidly Quenched Metals, Sendai, vol 2, 1173, (1981).

131. Moser N and Kronmuller H, J. Magnetism Mag. Mater., 19, 21, (1980).

132. Mott N F, J. Phys., C13, 5433, (1980).

133. Nachtrieb N H and Handler C N, Acta Met., 2, 797, (1954).

134. Piller J and Haasen P, Acta. Metall., 30, 1, (1982).

135. Pond R and Maddin R, TMS-AIME, 245, 2475, (1969).

136. Pound G M, Bitler W R and Paxton H W, Phil. Mag., 6, 473, (1961).

137. Prigogine I and Defay R, 'Chemical Thermodynamics', Longman Greens, (1954).

138. Primak W, Phys. Rev., 100(6), 1677, (1955).

139. Randall J T and Wilkins M H F, Proc. Roy. Soc. (London), 184, 390, (1945).

140. Rao K V, 'Amorphous Metallic Alloys', ed. Luborsky F E, Butterworths, Ch 21, (1983).

141. Ritland H N, J. Soc. Glass Technol., 39, 99, (1955)

142. Robertson J, Phys. Chem. Glasses, 23, 1, (1982).

143. Ruhl R C, Mater. Sci. Engng., 1, 313, (1967).

144. Sadoc J F, Dixmier J and Guinier A, J. Non.Cryst. Sol., 12, 46, (1973).

145. Scott G D, Nature, 188, 908, (1960).

146. Scott G D, Nature, 194, 956, (1962).

147. Scott M G, Scripta. Met., 15, 1073, (1981).

148. Scott M G, 'Amorphous Metallic Alloys', ed. Luborsky F E, Butterworths, 144, (1983).

149. Scott M G, Cahn R W, Kursomovic A, Girt E and Njuhovic N B, Proc. 4th Int. Conf. on Rapidly Quenched Metals, Sendai, vol 2, 469, (1981).

150. Scott M G and Kursomovic, Acta. Metall., 30, 853, (1982).

151. Shewman P G, 'Diffusion in Solids', Mcgraw-Hill, New York, (1963).

152. Simpson A W and Brambley D R, Phys. Status solidi, 43(b), 291, (1971).

153. Spaepen F, Acta Metall., 25, 407, (1977).

154. Spaepen F, J. Non-Crsyt. Solids, 31, 207, (1978).

155. Spaepen F, 'Physics of Defects', North Holland, 133, (1981).

156. Srolovitz D, Maeda K, Vitek V and Egami T, Phil. Mag., A44, 847, (1981).

157. Stearn A and Eyring H, J. Phys. Chem., 44, 955, (1940).

158. Takayama S, J. Mater. Sci., 11, 164, (1976).

159. Takayama S and Di T, J. Appl. Phys., 50, 6673, (1969).

160. Tarnoczi T, Phys. Stat. Sol., 87, 283, (1985).

161. Taub A I and Spaepen F, J. Mater. Sci., 28, 1781, (1980).

162. Tsuei C L and Duwez P, J. Appl. Phys., 37, 435, (1966).

163. Uhlmann D, 'Metallic Glasses', Metals Park, 128, (1978).

164. Uhlmann D R, J. Non-Cryst. Solids, 7, 337, (1972).

165. Ulfert W, Horvarth J, Frank W and Kronmuller H, Crsyt. Lat. Def. and Amorph. Mater., 18, 519, (1989).

166. Valenta P, Moser K, Kronmuller H and Freitag K, Phys. Stat. Solidi, 106, 129, (1981).

167. Van den Beukel A and Radelaar S, Acta Metall., 31, 419, (1983).

168. Vand V, Proc. Phys. Soc., London, 55, 222, (1943).

169. Volterra V, 'A Treatise on the Mathematical Theory of Elasticity', Dover, 221, (1944).

170. Warren B E, Averbach B L and Roberts B W, J. Appl. Phys., 22, 1493, (1951).

171. Waseda Y, 'The Structure of Non-Crystalline Materials', McGraw Hill, New York, (1980).

172. Wehner G K and Anderson G S, 'Handbook of thin film technology', chap 3, Mcgraw-Hill, New York, (1970).

173. Werner F E, 'Energy Efficient Steels', Eds Marder A R and Stephenson E T, pg 1, TSM-AIME, Pittsburgh, PA, (1981).

174. Williams R S and Egami T, IEEE Trans. Magn., MAG-12, 927, (1976)

175. Woldt E and Neuhaser H, J. Phys., c8 41, 846, (1980).

176. Wong J and Angell C A, 'Glass: Structure by Spectroscopy', Dekker, (1976).

177. Wong J, 'Glassy Metals', Ed. Guntherodt H J, Springer-Verlag, Berlin, 45, (1981).

178. Wood J V and Honeycombe R W K, J. Mater. Sci., 9, 1189, (1974).

179. Yokoyama A, Kamiyama H, Inoue H, Masumoto T and Kimura H M, Scripta Met., 15, 365, (1981).

180. Zener C, J. Appl. Phys, 22(4), 372, (1951a).

181. Zener C. Acta Cryst.,3, 346, (1951b).

182. Ziman J M, 'Models of Disorder', CUP, (1979).

8 Appendix

Software code for automation of the annealing procedure, written in Turbo Basic

```
1 Clear ,,2000
2 Def Seg = 0
4 Cseg = (256 * Peek(&H3c7))+Peek(&H3c6)
6 Def Seg
8 Def Seg =Cseg:Poke &H392,0:Poke &H397,0:Def Seg
10 init% = &H51f :wrstr% = init% + 18 :rdstrrdfile% = rdstr% + 18
12 wrfile% = rdfile%+18:adc% = wrfile%+18:gret% = adc%+18:sdl% = gret14 llo% =
sdl%+18 :abort% = llo%+18 :ppoll% = abort%+18 :ppd% = ppoll%+18
16 ppu% = ppd% + 18 :rbst% = ppu% + 18 :sdr% = rbst%+18 :spoll% = sdr%+18
18 ppen% = spoll% + 18 :adtl% = ppen% + 18 :adtr% = adtl% + 18
20 transfer% = adtr + 18 :pcnt% = transfer% + 18 :rcnt% = pcnt% + 18
22 sdc% = rcnt% + 18 : rdstrs% = sdc% + 18 : setto% = rdstrs% + 18
24 dma% = 0
26 tcimode% = 1
28 V$(2) = "cls09:f1r0n5t1"
30 Def Seg = Cseg
32 bd.addr% = &H310
34 er% = 0
36 Def Seg = Cseg
38 Call init%(dma%, ms%, tcimode%, my.addr%, bd.addr%, er%)
40 Def Seg
```

```
42 er%=0
100 Key Off
110 x = 1
120 Cls
122 For I = 1 to 10
123 Print ""
124 Next I
125 I = 0
130 If X = 1 then 135 else 155
135 Print " ";
140 Color 0,7 : Print "1 List of Annealing Time Sequence " : Color 7,0
150 Goto 170
155 Print " ";
160 Print "1 List Annealing Time Sequence "
170 If X = 2 then 175 else 195
180 Color 0,7 : Print "2 Change Annealing Time Sequence " : Color 7,0
190 Goto 210
195 Print " ";
200 Print "2 Change Annealing Time Sequence "
210 If X = 3 then 215 else 235
215 Print " ";
220 Color 0,7 : Print "3 Single Shot Anneal " : Color 7,0
230 Goto 250
235 Print " ";
240 Print "3 Single Shot Anneal "
250 If x = 4 then 255 else 275
```

```
255 Print " ";
260 Color 0,7 : Print "4 Continuos Anneal " : Color 7,0
270 Goto 290
275 Print " ";
280 Print "4 Continuous Anneal "
290 If x = 5 then 295 else 315
295 print " ";
300 Color 0,7 : Print "5 End Program " : Color 7,0
310 Goto 330
315 Print " ";
320 Print "5 End Program "
330 a$ = inkey$ : If a$ = "" then 330
340 V = asc(a$)
350 If V = 56 then X = (X-1) mod 5
360 If X = 0 then X = 5
370 If V = 50 then X = (X+1) mod 5
380 If X = 0 then X = 5
390 If V = 13 then 400 else 120
400 If X = 1 then 500
410 If X = 2 then 600
420 If X = 3 then 800
430 If X = 4 then 1100
440 If X = 5 then stop
500 Cls
505 File$ = "info"
506 Print ""
```

```
507 Print ""
508 Print ""
509 Print ""
510 Color 0,7 : Print " List of Sequential Annealing Times " : Color 7,0
512 Print ""
513 Print ""
515 Open File$ for Input as 1
520 Input #1, n
525 For I = 1 to n
530 Input #1, y
535 Print y;
540 Next I
545 Close 1
546 For I = 1 to 10
547 Print ""
548 Next I
549 Print ""
550 Color 0,7 : Print "Press any key to proceed.... " : Color 7,0
555 B$ = inkeky$ : If B$ = "" then 555
560 I = 0
565 Goto 120
600 Cls
605 File$ = "info"
610 Open File$ for Output as #1
615 Gosub 675
620 Print " How many annealing sequences do you wish to perform ? " ;
```

```
625 Input m
630 Write #1, m
635 For I = 1 to m
640 Gosub 675
645 Print " Enter Time " ; I ; " : " ;
650 Input p
655 Write #1, p
660 Next I
665 Close 1
670 Goto 120
675 Cls
676 Print ""
677 Print ""
678 Print ""
679 Print " ";
680 If I < m then return
690 Goto 120
800 Cls : out &H79b, &H80
810 Print "Enter annealing time for single shot anneal : " ;
815 Input ta%
820 On Timer(10) Gosub 870
830 Timer On
840 Out &H709, &H40
850 While not instat : wend
860 Timer Off
870 Cls
```

```
880 Gosub 2000
890 Print " ";
900 Color 0,7 : Print " Time        Length        Resistivity " : color 7,0
910 Print " 0 " ; l ; "          "; r
920 Goto 1500
930 Gosub 2000
940 Print " "; ta%; " "; l ; " " ; r
950 Print ""
960 Print ""
970 Print " ";
975 Color 0,7 : Print "Press any key to proceed " : Color 7,0
980 a$ = inkey$ : If a$ = "" then 980
985 Out &H709, &H0
990 Goto 120
1100 Cls
1110 File$ = "info"
1120 Open File$ for Input as 1
1130 da$4 = "exp.dat"
1140 Open da$ for Output as #2
1150 Input #1, n
1160 Out &H70b, &H80
1170 On Timer (10) Gosub 1200
1180 Timer On
1190 Out &H709, &H40
1200 Timer Off
1210 Gosub 2000
```

```
1215 le = (l*.00001)
1216 re = r
1220 Color 0,7 : Print " Time        length        resistivity " : color 7,0
1237 y% = 0
1238 t% = 0
1240 y% = y% + 1
1250 Input #1, tim%
1255 ta% = tim% - t%
1260 Goto 1500
1270 Gosub 2000
1280 Print tim% ; " "; -l ; " " ;-r
1290 Print #2, tim%, ",", -l, ",", -r
1295 t% = tim%
1300 If (y% < n) then 1240
1305 Out &H709, &H0
1310 Close 1
1320 Close 2
1330 Goto 120
1500 On Timer (2) Gosub 1540
1510 Timer On
1520 Out &H709, &H2
1530 While not instat : wend
1540 Timer Off
1550 On Timer (ta%) Gosub 1600
1560 Timer On
1570 Out &H709, &H22
```

```
1580 While not instat : wend
1590 Timer Off
1600 Out &H709, &H2
1610 On Timer (2) Gosub 1650
1620 Timer On
1630 While not instat : wend
1640 Timer Off
1650 Out &H709, &H40
1660 On Timer (25) Gosub 1690
1670 Timer On
1680 While not instat : wend
1690 Timer Off
1700 If X = 3 then 930
1800 If X = 4 then 1270
2000 For x% = 1 to 2
2010 term% = 2:eos% = 10:strnum% = 1:er% = 0
2020 lad%(0) = 9:lad%(1) = 199
2030 V$(1) = "cls04:f1r1n5t1"
2040 V$(2) = "cls05:f1rn5t1"
2050 Def Seg = Cseg
2060 Call wrstr%(eos%, term%, lad%(0), v$(x%), strnum%, er%)
2070 Def Seg
2080 data.str$(x%) = space$(13)
2090 eos% = 10:term% = 2:tad%(0) = 9:tad%(1) = 199:strnum% = 1:er% = 0
2100 Def Seg = Cseg
2110 Call rdstr%(eos%, term%, tad%(0), data.str$(x%), strnum%, er%)
```

```
2120 Def Seg
2130 If er% <> 0 then print "error = "; er%:stop
2140 Next x%
2150 r = val(data.str$(1)) : l = val(data.str$(2))
2160 Return
```